Chasing Rainbows on Enceladus

Discovery of an Inclined Periodic Structure in the Saturnian System

Niels Rubbrecht

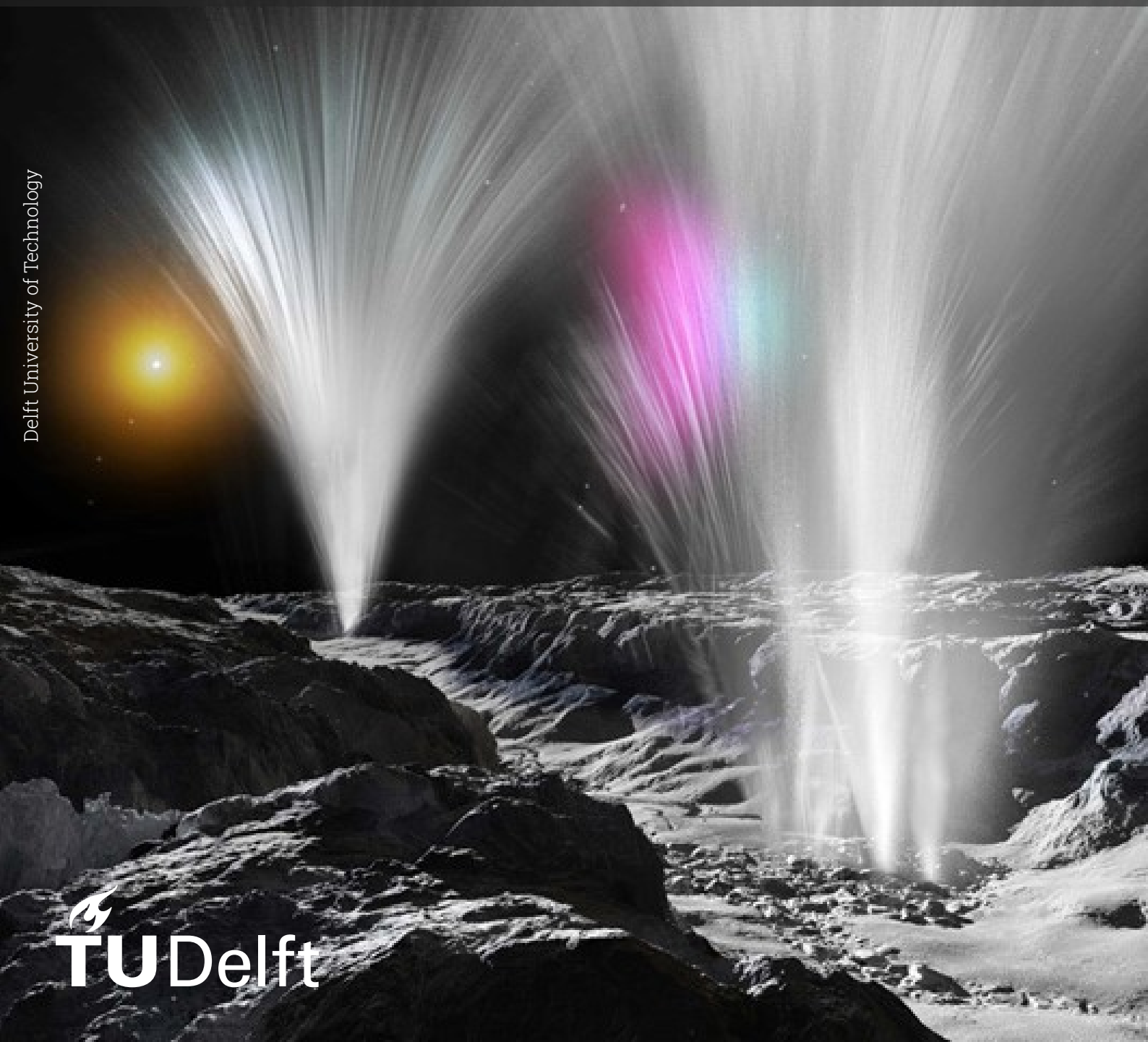

Delft University of Technology

TU Delft

This page is intentionally left blank.

Chasing Rainbows on Enceladus

Discovery of an Inclined Periodic Structure in the Saturnian System

by

Niels Rubbrecht

to obtain the degree of Master of Science
at the Delft University of Technology,
to be defended publicly on Tuesday November 19, 2024.

Student number: 4876539
Project duration: January 16, 2023 – November 19, 2024
Thesis committee:
Dr. S. M. Cazaux, TU Delft, Supervisor
Dr. J. J. D. Loicq, TU Delft, Chair
Dr. M. A. Kenworthy, Leiden University, Examiner

Cover: Fountains of Enceladus by Ron Miller (CICLOPS Art Room)

TU Delft

Preface

The saying *chasing rainbows* often implies pursuing an illusory goal. Yet it can also symbolise a journey fuelled by curiosity and a quest for something beautiful or elusive, even without any guarantee of finding it. This perfectly captures my experience with this project. A simple question—*Could there be rainbows on Enceladus?*—sparked my curiosity and led me to explore optical phenomena in Enceladus' plumes for my MSc thesis at the Faculty of Aerospace Engineering at the TU Delft. At times, it felt like searching for ghosts in the vast archive of Cassini data, but each breakthrough made the pursuit all the more thrilling.

I shared this journey with my daily supervisors, Stéphanie Cazaux and Jérôme Loicq, whose contagious enthusiasm made our weekly meetings a highlight of my week. I often wondered how we stayed so excited over stripes in Cassini images. Yet, their insights, encouragement, and dedication made every discussion meaningful and motivating. My deepest thanks go to them for their invaluable feedback and involvement. I am also grateful to Matthew Kenworthy, who, since the start of the project, has been a source of insightful feedback and inspiring discussions that guided me throughout this work. I would also like to extend my gratitude to Benoît Seignovert, Nicholas Kutsop, and Stéphane Le Mouélic whose expertise and fresh perspectives were instrumental in characterising the observations in this report.

I would like to extend a special thanks to Olivier, who has supported me and stood by me throughout this experience. I would also like to thank my friends who have been with me since the start of my journey in Delft—Arnaud, Kasper, and Oscar—as well as the friends I made along the way: Thomas, Bram, Aurelie, Kirsten, and Léon. These friends have given me some of the best years of my life.

Niels Rubbrecht
Delft, November 2024

Summary

Enceladus, one of Saturn's icy moons, releases massive plumes of water vapour and ice from its south pole, fed by a subsurface ocean. These geyser-like plumes provide a unique glimpse into the moon's internal processes. Observations from Cassini's remote sensing and in-situ instruments have been essential in characterising these plumes and evaluating Enceladus' potential to support life.

This report introduces a novel method for characterising Enceladus' plumes using Cassini's Visible and Infrared Mapping Spectrometer (VIMS) and Imaging Science Subsystem (ISS) to search for optical phenomena, such as rainbows and ice particle halos, created by light interacting with the plume particles. These phenomena, along with specific occurrence conditions, reveal particle properties like size distributions, ice phase structure, and optical constants.

Simultaneous VIMS-IR and ISS high-phase observations during Cassini flyby E17 captured unique stripe-like features in Enceladus' plumes, with similar patterns noted in VIMS-IR data from flybys E13 and E19. These parallel stripes, inclined at 16° to the ecliptic and 43° to Saturn's ring plane, appear continuous when projected in the J2000 reference frame. A central stripe, brightest at wavelengths around 5 microns, acts as the zeroth-order diffraction peak of a reflection grating with groove spacing of 0.12–2.60 mm. The adjacent stripes act as higher-order diffraction peaks.

Unlike any known atmospheric phenomenon on Earth, these observations point to a periodic, inclined, millimetre-scale structure within the Saturnian system. We propose two possible explanations: the patterns may arise from a periodic structure within the orbits of Saturn's Norse group moons or from an ordered structure in the E-ring. Further investigation of these unexpected findings may yield new insights into particle behaviour and ring dynamics within Saturn's complex environment.

Contents

Nomenclature

Abbreviations

Abbreviation	Definition
CAPS	Cassini Plasma Spectrometer
CCD	Charge-Coupled Device
CDA	Cosmic Dust Analyser
CIRS	Composite Infrared Spectrometer
DEC	Declination
DN	Data Number
ESA	European Space Agency
ET	Ephemeris Time
FOV	Field Of View
FWHM	Full Width at Half Maximum
IAU	International Astronomical Union
ICRF	Internation Celestial Reference System
IFOV	Instantaneous Field Of View
INMS	Ion Neutral Mass Spectrometer
ISIS	Integrated Software for Imagers and Spectrometers
ISS	Imaging Science Subsystem
IR	Infrared
ISA	Italian Space Agency
LWIR	Long-Wave Infrared
MNWC	Main Non-Water Constituent
NAC	Narrow Angle Camera
NAIF	Navigation and Ancillary Information Facility
NASA	National Aeronautics and Space Administration
NIR	Near-Infrared
PDS	Planetary Data System
PSF	Point Spread Function
SPICE	Spacecraft, Planet, Instrument, C-matrix, Events
UTC	Coordinated Universal Time
UV	Ultraviolet
UVIS	Ultraviolet Imaging Spectrograph
RA	Right Ascension
RSP	Remote Sensing Palette
VIMS	Visible Infrared Mapping Spectrometer
VIS	Visible
VMC	Venus Monitoring Camera
WAC	Wide Angle Camera

Symbols

Symbol	Definition	Unit
A	Refracting angle	[°]
a	Particle radius	[m]
a_s	Absorption coefficient	[-]
D	Total deviation angle	[°]
D	Diameter	[m]
$E_{\parallel i}$	Parallel component of the incident electric field	[V/m]
$E_{\perp i}$	Perpendicular component of the incident electric field	[V/m]
$E_{\parallel s}$	Parallel component of the scattered electric field	[V/m]
$E_{\perp s}$	Perpendicular component of the scattered electric field	[V/m]
F/N	F-number (focal length/aperture diameter)	[-]
I	Intensity	[arbitrary]
I/F	Reflectance (radiance/irradiance)	[-]
i	Angle of incidence	[°]
J_1	First-order Bessel function	[-]
k	Number of internal reflections	[-]
k	Wavenumber	[m^{-1}]
L	Length of hexagonal ice crystal	[m]
m	Relative refractive index of the sphere	[-]
n	Real relative refractive index (n_r/n_i)	[-]
n_i	Real incident refractive index of the medium	[-]
n_m	Refractive index of the surrounding medium	[-]
n_r	Real refractive index of the refracting material	[-]
r	Angle of refraction	[°]
r	Distance from particle (far field)	[m]
S_j	Amplitude scattering matrix element ($j = 1, 2, 3, 4$)	[-]
x	Size parameter	[-]
η	Path difference	[m]
λ	Wavelength of incident light in vacuum	[m]
λ_m	Wavelength of light in medium	[m]
ω	Angular frequency	[rad/s]
ρ	Particle radius	[m]
σ	Standard deviation	[-]
τ	Optical thickness	[-]
θ	Scattering angle	[°]
$\widetilde{\beta}$	Scattering phase function for unpolarized light	[-]

1

Introduction

The Cassini spacecraft, launched by a joint effort between NASA, ESA and ASI, revolutionised our understanding of Saturn and its moons during its 13-year mission [73]. One of its most remarkable discoveries was the detection of geyser-like plumes erupting from Saturn's icy moon Enceladus in 2005 [60]. These plumes, originating from the moon's south polar region, stem from a global subsurface ocean beneath its icy crust [56, 64], offering a unique window into Enceladus' internal processes and evolutionary history [16]. Subsequent research detected complex organic molecules in the icy grains of the plumes from in-situ sampling with Cassini's Cosmic Dust Analyser (CDA) [12, 65]. These findings provide direct evidence of a potentially habitable environment beyond Earth and make Enceladus a prime target for future missions to search for life [10, 62]. This emphasis is further supported by ESA's Voyage 2050 program, which prioritizes the exploration of icy moons, including Enceladus, as part of its long-term strategy for Solar System exploration [19].

Consequently, extensive research has been conducted to characterise the plumes using both remote sensing techniques and in-situ measurements collected by Cassini [26, 65]. One approach was developed by Ingersoll and Ewald [34], who used forward-scattering absolute brightness measurements from the Imaging Science Subsystem (ISS) to estimate the particle column densities and total particulate mass within the plumes. Subsequent research has built upon this method, providing deeper insights into the plumes' dynamics [35, 60, 62]. Another approach, led by Hedman et al. [30], utilised spectral data from the Visible and Infrared Mapping Spectrometer (VIMS) to develop particle density profiles versus height. However, significant discrepancies in particle number density estimates between these methods persist, with differences of up to factors of two to three [62].

This report aims to introduce a new remote-sensing approach which has not been previously used to characterise the particles ejected from Enceladus' plumes. Optical phenomena commonly observed in Earth's atmosphere, such as rainbows and halos, are not only visually captivating but also provide key information about the particles involved in their formation [41]. These phenomena arise from the interaction of light with particles, such as water droplets or ice crystals [23, 52, 54]. The unique appearances of the phenomena, coupled with the specific conditions needed for their occurrence, can be exploited to derive particle properties. For instance, glories observed atop clouds on Earth provide crucial clues about cloud formation and evolution [49]. While rare beyond Earth, such phenomena have been recorded elsewhere in the Solar System. For instance, the Venus Express orbiter captured a glory on the upper cloud layer of Venus, shedding new light on the material and size distribution of the cloud particles [46, 58]. Similarly, the Mars Perseverance rover recorded an ice particle halo generated by hexagonal prisms within crystalline water-ice clouds, offering valuable data on Martian cloud formation conditions [44].

Enceladus' plumes offer another promising opportunity for observing optical phenomena within the Solar System. Remote sensing of these plumes relies on forward-scattered light from the solid particles within the optically thin material [35]. This is reminiscent of the conditions that create optical phenomena like rainbows and halos in the Earth's atmosphere. Enceladus' plumes can be likened to a

garden hose, where sunlight hitting a spray of water droplets creates a rainbow. This imaginative idea has inspired several astronomical artists, who have depicted optical phenomena within the plumes, as illustrated on the front page of this report. Building on this artistic vision, the scientific search for colour variations in Enceladus' plumes caused by optical phenomena offers a novel and unique opportunity to characterise the particles within the plume. This gave rise to the main research question for this scientific report:

"Can optical phenomena be observed in Enceladus' plumes from Cassini measurements, and what can these reveal about the physical and chemical structure of the particles within?"

The primary research question is further explored through several sub-questions:

1. What are the expected projections of the rainbow, corona, halo, and glory optical phenomena onto Enceladus' plumes when observed from the ISS and VIMS for a complete 3-dimensional observer geometry?
2. How will the plume data be analysed to find signatures of the optical phenomena?
3. What can the (lack of) optical phenomenon signatures reveal about the physical and chemical structure of the plume particles?
4. Can optical phenomena be observed using artificial plume experiments and what can these reveal about the plumes' composition?
5. What recommendations can be made for future missions to observe and exploit optical phenomena for particle characterisation?

The research questions will be addressed in the report according to the following structure. First, in chapter 2, an overview will be given of the current state of research regarding optical phenomena in atmospheric optics and the characteristics of Enceladus' plumes. Second, the findings will be detailed in a scientific article referenced in chapter 4. Lastly, in chapter 5, conclusions and recommendations will be presented for further research in this field.

2

Background

This chapter aims to present an overview of the background information pertinent to the scientific article discussed in chapter 4. First, section 2.1 will provide a summary of the fundamentals of meteorological optics. This will cover the theoretical basis for commonly observed phenomena on Earth, as well as an overview of various light scattering theories. In section 2.2, research will be presented that used observations of optical phenomena (on Earth and in space) to determine particle properties. In section 2.3, the state-of-the-art science on Enceladus' plumes will be reviewed to provide insights into the plume's composition and dynamics. The Cassini instruments used to observe the plumes will be described in section 2.4. Finally, the knowledge of optical phenomena, Enceladus' plumes and Cassini's instruments will be combined to assess for potential observations of optical phenomena in Enceladus plumes in section 2.5.

2.1. Meteorological Optics

In the search for optical phenomena in Enceladus' plumes, one must first look at what drives these spectacular light displays on Earth. The aim of this chapter is to give an overview on the fundamentals of meteorological optics, starting with a theoretical approach on the origin of common optical atmospheric phenomena. First, the rainbow will be explained through geometrical ray tracing optics in subsection 2.1.1. Secondly, in subsection 2.1.2, the most common features of ice particle halos will be elaborated upon. Next, diffraction theory will be introduced to explain the atmospheric corona in subsection 2.1.3. In subsection 2.1.4, supernumerary rainbows and fog bows will be explained through Airy theory. The glory or anti-corona will briefly be discussed in subsection 2.1.5. This is followed by an introduction to Mie theory subsection 2.1.6 which can approximate most light scattering phenomena. Lastly, the appearance of these optical phenomena in the infrared spectrum will be discussed in subsection 2.1.7.

2.1.1. The Rainbow

The theory of the rainbow can be adequately explained through geometrical optics, which is based on reflection and refraction. The relation between the angle of incidence (i) and angle of refraction (r) is given by Snell's law in Equation 2.1 where n_i is the incident refractive index of the medium and n_r is the refracted index of the refracting material. Descartes first came up with the geometrical optical theory of the rainbow based on Figure 2.1. Here he assumed a transparent spherical water droplet suspended in air. In Figure 2.1 (a) the droplet is hit by a light ray at point A at an angle of incidence i. The ray first undergoes refraction upon entering the water drop resulting in a deviation of $i - r$. Next, internal reflection takes place in point B deviating the ray over an angle of $\pi - 2r$. Lastly, the ray again undergoes a deviation of $i - r$ after leaving the water drop in point C due to refraction. A similar approach can be taken for two internal reflections as seen in Figure 2.1 (b). The total deviation D for k internal reflections is given by Equation 2.2 [77].

$$n_i \sin i = n_r \sin r \tag{2.1}$$

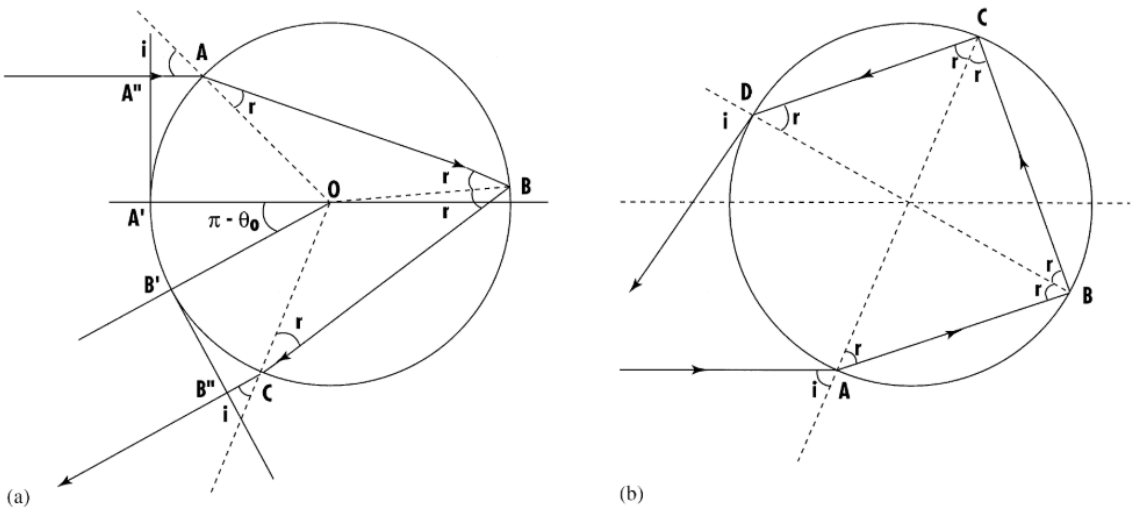

Figure 2.1: Ray hitting a spherical drop at incidence angle i experiencing refraction with refraction angle r for one internal reflection (a) and two internal reflections (b) [2].

$$D = 180k^\circ + 2i - 2(1+k)r \tag{2.2}$$

Figure 2.2 shows the trajectories of 12 rays hitting the water drop at different incidence angles. The deflections of these rays compared to i are plotted Figure 2.3. Among these rays, the seventh one corresponds to the point of minimal deviation. This ray is referred to as the Caustic or Rainbow ray as light rays bundle up around this ray, creating an intense surge of light at that specific angle [2]. The required i can be found by derivation of $\frac{dD}{di} = 0$.

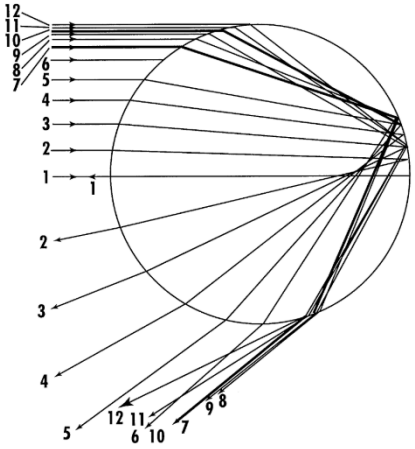

Figure 2.2: The trajectories of multiple rays passing through a spherical raindrop [2].

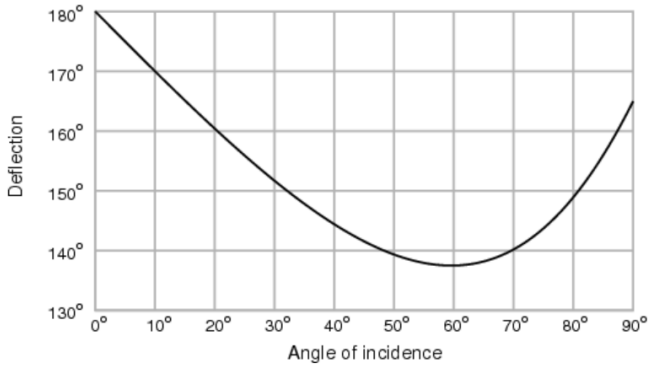

Figure 2.3: Variations in the total deviation angle corresponding to different angles of incidence [77].

Differentiating Equation 2.2 results in Equation 2.3.

$$\frac{dD}{di} = 2 - 2(1+k)\frac{dr}{di} \tag{2.3}$$

Next, differentiating Snell's law gives Equation 2.4, which is put in Equation 2.3, resulting in Equation 2.5. The refractive index of the refracting material relative to the medium is written as $n = n_r/n_i$.

$$\cos i = n \cos r \frac{dr}{di} \tag{2.4}$$

$$\frac{dD}{di} = 2 - 2(1+k)\frac{\cos i}{n \cos r} \tag{2.5}$$

Searching for the minimum with condition $\frac{dD}{di} = 0$,

$$\begin{aligned}
\frac{1}{1+k} &= \frac{\cos i}{n \cos r} \\
\frac{1}{(1+k)^2} &= \frac{\cos^2 i}{n^2(1 - \sin^2 r)} \\
&= \frac{\cos^2 i}{n^2 - \sin^2 i} \\
&= \frac{\cos^2 i}{n^2 - 1 + \cos^2 i}
\end{aligned}$$

$$\cos i = \sqrt{\frac{n^2 - 1}{k(2+k)}} \tag{2.6}$$

Equation 2.6 gives the angle of incidence required for the Caustic ray based solely on refractive index n and number of internal reflections k, which in turn gives the value of minimum deviation. Looking back at Figure 2.1, $\pi - \theta_0$ gives the angular radius of the rainbow. In the case of a single reflection which corresponds to the primary rainbow, for the colour red at wavelength $\lambda = 656$ nm and $n_{\text{water}} = 1.3318$, the minimum deviation is $180° - 42°18'$. Therefore, the angular radius of the red bow is $42°18'$. For violet light of $\lambda = 405$ nm, $D_{\text{min}} = 180° - 40°36'$ resulting in a violet bow of angular radius $40°36'$. A double reflection as seen in Figure 2.1 (b) results in a secondary rainbow. For red wavelengths, the angular radius is $50°40'$, and for violet light, this is $53°36'$. The secondary rainbow thus lies outside of the primary with its colours being inverted (red on the inside, violet outside). The resulting visible phenomena are shown in Figure 2.4. Additionally, the area between the primary and secondary rainbow appears to be much darker than the area inside the primary bow (especially on the right side of the picture). This phenomenon is called Alexander's dark band and is created due to the lack of light being scattered at these angles [77]. Furthermore, Fresnel proved that the light from the rainbows is highly polarised parallel to the plane of incidence due to the dependence of the reflection and refraction coefficients on the polarisation of light for different incidence angles [77].

In conclusion, rainbows are formed by refraction and reflection of light through a spherical water drop. According to Lynch and Schwartz [45], the minimal radius of the droplets should be 35 µm. The primary rainbow can be observed at an angular size of approximately 42° from the anti-solar point, while for the secondary rainbow, this is 53°. The secondary rainbow is fainter than the primary because of losses due to an extra internal reflection. Rainbow light is also strongly polarised.

Figure 2.4: Double rainbow in Alaska [11]

2.1.2. The Ice Particle Halo

Ice crystal halos are a collection of circles, arcs, and light spots formed when sunlight strikes ice crystals in the atmosphere. The most observed features are shown in Figure 2.5. The 22° halo is the most common of at least eight circular halos that centre on the Sun or Moon. It has a pale, mostly white colour with red on the interior. Parhelia, often known as sundogs, are brilliant, spectrally smeared dots that appear at the same height as the sun. These appear on the 22° halo when the Sun is at the horizon but move more outside the halo as the Sun rises in the sky [20]. Another feature is seen above the 22° halo called the upper tangent arc with similar colour variations as the sundogs. A vertical shaft of light can also be observed and is called a sun pillar. Moving to larger angular distances from the sun, there are the rare but more colourful 46° halo and a circumzenithal arc [52] [20].

Similarly to the rainbow, the origin of the elements in the ice particle halos lies in refraction and reflection of light explained through geometrical optics. However, instead of spherical water droplets, there are ice prisms that interact with the sunlight. Ice crystals most commonly form in hexagonal structures as seen in Figure 2.6. The most common crystals are needles which are thin hexagonal columns with long principal axes (top image), and plates which have a shorter principal axis (bottom image) [20].

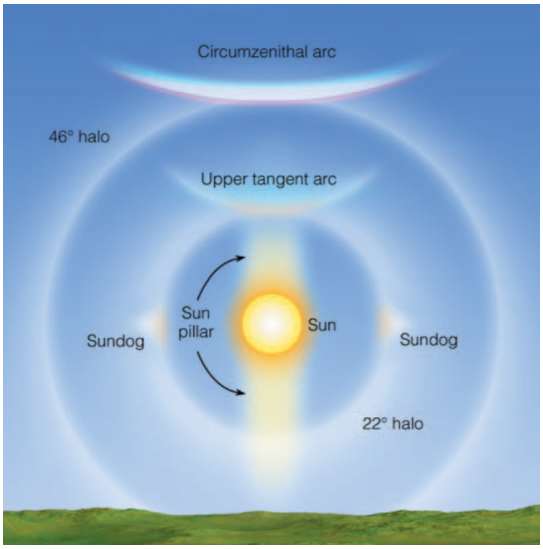

Figure 2.5: Ice crystal phenomena in ice particle halo [3]

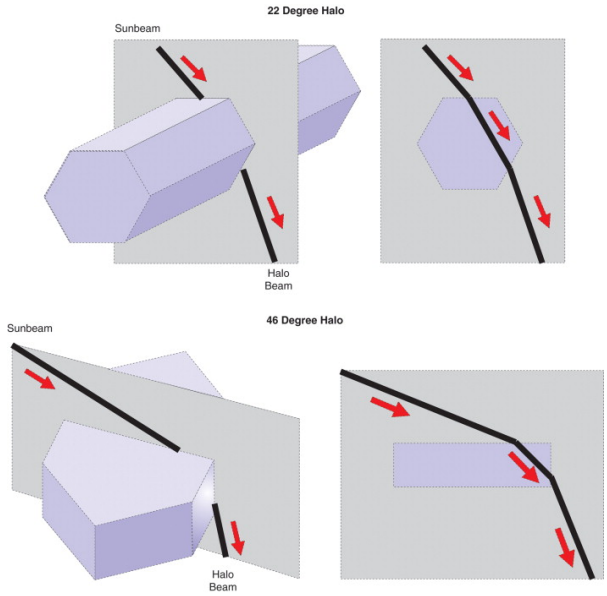

Figure 2.6: Light rays hitting the prism in a plane normal to the refracting edge with a refracting angle of $60°$ (top) and $90°$ (bottom) [20]

It was found that Equation 2.7, the equation for the refraction of a light ray hitting a prism in a plane perpendicular to the refracting edge (grey plane), can explain the presence of the most common 22° and the more rare 46° halo.

$$n_i \sin\frac{A + D_{min}}{2} = n_r \sin\frac{A}{2} \tag{2.7}$$

Here, A is the refracting angle of the prism, D_{min} is the minimum deviation, n_i is the refractive index of the incident medium, and n_r is the refractive index of the ice prism. If the light ray propagates through a medium with n_i=1 and hits an ice prism with $n_r = 1.31$ with refracting angle $A = 60°$ (see Figure 2.6 top) or $A = 90°$ (Figure 2.6 bottom) the angle of minimum deviation becomes $22°$ and $46°$ respectively. Tricker [77] proved that sun rays hitting the prism in a plane inclined to the refracting edge (every plane except the grey one in Figure 2.6) do not contribute to these halos as the limiting angles of incidence to avoid complete internal reflection are larger than those for minimum deviation. The pale colours of the halo can be explained by the double requirement for D_{min}; the angle of incidence needs to be just right, and the rays must hit normal to the refracting edge. The other rare phenomena in the halo can be explained by more complex crystal shapes and common orientations of the ice crystals

with respect to the sunlight. The sundogs, for example, are formed by light rays passing through falling ice crystal plates, which are oriented horizontally with respect to the surface due to friction with the air. Similarly, as hexagonal column ice crystals descend with their long axes parallel to the ground, the upper tangent arc is formed. The brilliant arc of light is created when sunlight is refracted through these ice crystals. The sun pillar is formed solely from the reflection of sunlight from horizontally oriented plates and columns. These oscillate and rotate as they fall, creating a bright pillar of light. Many more intricate displays of halos have been observed, and an overview of all observed elements was catalogued by Moilanen and Gritsevich [52].

According to Bi and Yang [5], peaks in the phase function of compact hexagonal ice crystals, like the $22°$ and $46°$ halo, start to show up as the size parameter $(2\pi L/\lambda)$ gets closer to 80. Here compact prisms with length (L) of twice the size of a hexagon facet (so, $L \sim D$, diameter) were assumed. This assumption is validated by Yang et al. [82], who stated that the aspect ratios are close to one for compact ice crystals smaller than 40 µm in size. When the equivalent size parameter gets closer to 150, this sensitivity to particle size tends to decrease. Additionally, Bi and Yang [5] developed a T-matrix method to construct phase functions for single ice crystals of different forms and aggregates. The diminishing effects of surface roughness and internal inclusions on the halo intensity peaks were also investigated. Surface roughness may cause the halos to diminish or disappear for particles that are arbitrarily big [82]. As a result, the halo cannot be regarded as a diagnostic for sizes larger than the lowest permitted value. Additional constraints and characteristics regarding the formation of the ice particle halo are summarised in Table 2.1. The expected appearance can also be modelled through freely available Software like HaloSim3 by Les Cowley and Michael Schroeder.

2.1.3. The Corona

The corona is an optical phenomenon seen around a luminous object when it is observed through a mist or thin cloud. Contrary to the halo and the rainbow, the corona is seen at much smaller angular distances, and its origin lies outside that of geometrical optics. The corona is the result of diffraction of light around liquid water droplets or ice particles [77] as can be seen in Figure 2.7.

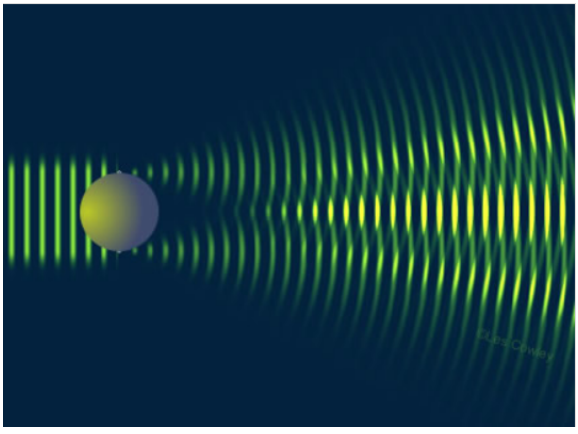

Figure 2.7: Light diffracted by a droplet [13]

Figure 2.8: picture of the lunar corona with three rings. The third red ring's placement is indicated by the arrow [40].

The diagram shows how two spots on a droplet surface scatter light and generate spherical waves. The scattered waves overlap and interfere. Where wave crests of the same sign overlap, the light intensity increases. Waves of opposite amplitudes interact destructively, resulting in low intensity. Scattered light from the entire droplet surface, plus lesser contributions from reflected and transmitted waves, combine to form a diffraction pattern which forms a corona. Corona are mainly formed in nature through cloud drops. It is irrelevant how far apart the cloud particles are spaced. Mutual interference, similar to a diffraction grating, only occurs when droplets are closer than two diameters apart, while cloud particles are separated by 50 or more diameters. In addition, droplets do not have to be spherical or even clear. Coronae can be made up of huge absorbing dust particles, pollen grains, and tiny ice crystals. However, the size distribution of the particles needs to be narrow as different droplet sizes produce different size rings, which can blur out the corona [13]. Diffraction of a spherical particle can be modelled

through Fraunhofer diffraction seen in Equation 2.8.

$$I(\theta) \propto \left[x \frac{[1+\cos\theta]}{2} \frac{(J_1[x\sin\theta])}{[x\sin\theta]} \right]^2 \tag{2.8}$$

$I(\theta)$ is the intensity of the scattered field at scattering angle θ, $x = 2\pi r/\lambda$ with r the spherical particle radius, λ the wavelength of the light and J_1 is the first-order Bessel function [40]. From Figure 2.8, it can be seen that the corona consists of multiple concentric rings of pale colours. The angular size of these rings depends strongly on the size of the diffracting particles, as will be shown in subsection 2.2.2. Typically, coronas can be visible for particles with radii from 1 to 20 microns [69]. These particle sizes can result in coronas with angular sizes of 30° to 3° [40]. The angular size of the rings thus increases for decreasing particle sizes. Additional constraints and characteristics of the corona are listed in Table 2.1.

2.1.4. Supernumerary Rainbows and Fog bows: Airy Theory

These optical phenomena, which are frequently seen as bows, are essentially caused by rays from a raindrop interfering with one another close to the rainbow angle or the angle of minimal deviation (see Figure 2.9). These rays often penetrate the raindrop at various incidence angles and follow diverse routes through the denser material (in this case, water), as was shown in Figure 2.2. The unique diffraction pattern resulting from constructive and destructive interference is caused by the cumulative effect of various route lengths. The diameter of the raindrop and the light's wavelength determine how far apart the peaks and minima are in this diffraction pattern. Greater distances between these extremes are seen in smaller raindrops. The first maximum is prominently located below the major bow when raindrop sizes are less than about 0.2 mm. Given favourable conditions, many such maxima may be seen [2].

Figure 2.9: Primary rainbow with three supernumerary arcs[42]

Tricker [77] showed that this wave-like phenomenon can be explained by examining wavefronts and rays through geometrical optics. As the angle of incidence increases, focus is directed toward the point where a ray emerges from the raindrop rather than the angle of least deviation. A thorough examination of Figure 2.2 shows that when the angle of incidence changes from zero, the point of entry circles the drop clockwise, and at the same time, the point of emergence moves counterclockwise at first, reaches an extreme, and then turns clockwise. Rays exiting the drop near this extreme point will have a major impact on the wavefront's form. Referring to this figure, the objective is to determine when the angle BOA $4r-i$ is maximal. Following the derivation of Adam [2] this maximum occurs for $\mathrm{d}(4r-i)/\mathrm{d}i = 0$ which results in:

$$\frac{\mathrm{d}r}{\mathrm{d}i} = \frac{1}{4}$$

and

$$\frac{\mathrm{d}^2 r}{\mathrm{d}i^2} < 0.$$

from the first derivative:

$$\frac{\cos^2 i}{n^2 - \sin^2 i} = 16$$

or

$$i = \arccos\left(\frac{n^2 - 1}{15}\right)^{1/2},$$

For $n = 1.33$, $i \approx 76.8°$, which is much larger than the angle associated with the rainbow ($\approx 59.4°$), as depicted in Figure 2.10 (a), the ray labelled YEY' emerges at minimum deviation. Rays situated on either side of YEY' experience greater deviations. Looking at the corresponding wavefront WEW (altered from the original wavefront XOX' as seen in Figure 2.10 (b), the wavefront can be approximated as a cubic function. With point E as the origin and YY', XX' as the coordinate axes, the equation of the wavefront WEW' can be written as

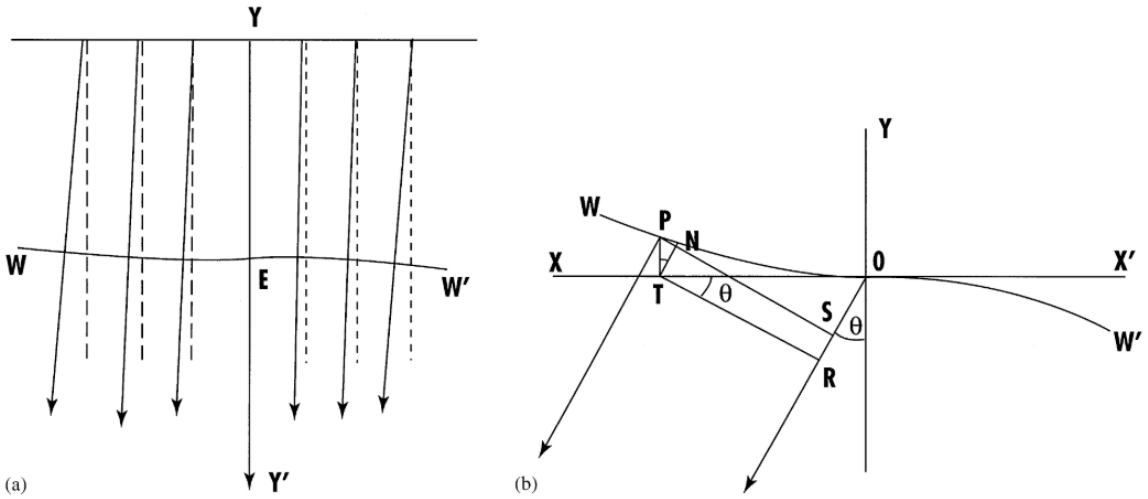

Figure 2.10: (a) The ray of minimum deviation YY' and nearby rays emerging from the (locally) cubic wavefront WW', (b) the geometry of the wavefront WW' leading to the Airy integral form for the amplitude [2]

$$y = c' x^3,$$

since $y'(0) = 0$, where c' is a constant with dimensions of (length $)^{-2}$. The linear wavefront's dimensions should be proportional to the size of the raindrop that generated it. From this, the wavefront function can be written in terms of drop radius a

$$y = \frac{c}{a^2} x^3,$$

c is currently dimensionless. Now, the famous "rainbow integral" introduced by Sir George Airy in 1838 can be derived [2]. Using Figure 2.10(b), an expression for the amplitude of the wave in a direction making an angle θ with that of minimum deviation can be derived. From examining the path difference η between the points $P(x, y)$ and O

$$\eta = OS = OR - RS = OR - TN = x \sin\theta - y \cos\theta$$

or

$$\eta = x \sin\theta - \frac{cx^3}{a^2} \cos\theta.$$

A small part of the wavefront δx at O can be written as $\sin \varpi t$, then a similar element at P can be written in the form $\sin(\varpi t + \delta)$, where

$$\delta = \frac{2\pi\eta}{\lambda} = k\eta$$

λ is the wavelength, and k is the wavenumber of the disturbance. The total disturbance of the entire wavefront is presented as an integral

$$A = \int_{-\infty}^{\infty} \sin(\varpi t + k\eta) \mathrm{d}x$$

or, because $\sin k\eta$ is an odd function,

$$A = \sin \varpi t \int_{-\infty}^{\infty} \cos k\eta \mathrm{d}x.$$

This becomes Airy's rainbow integral when expressed as below.

$$A = \left(\frac{\pi a^2}{2kc \cos\theta}\right)^{1/3} \int_{-\infty}^{\infty} \cos \frac{\pi}{2} \left(m\xi - \xi^3\right) \mathrm{d}\xi.$$

with

$$\xi^3 = \frac{2kcx^3 \cos\theta}{\pi a^2}$$

and

$$m\xi = \frac{2kx \sin\theta}{\pi},$$

The graph of the rainbow integral is shown in Figure 2.11. This technique is based on the fundamental assumption that diffraction occurs at spots on the wavefront near the Descartes ray. This assumption is valid when the drop size is significantly bigger than the wavelength of light, which is usually the case with most rainbows. While this assumption may not be valid for smaller cloud or fog droplets, which are much smaller than raindrops, the drop diameter may still be five or ten times the wavelength, making the Airy theory a useful approximation [2]. From the Airy model, Tricker [77] further concluded that the intensity of the light will be proportional to $(a^7/\lambda)^{1/3}$. Figure 2.12 shows the origin of the supernumerary rainbows lying in interference between cusp-shaped wavefronts close to the Descartes Ray.

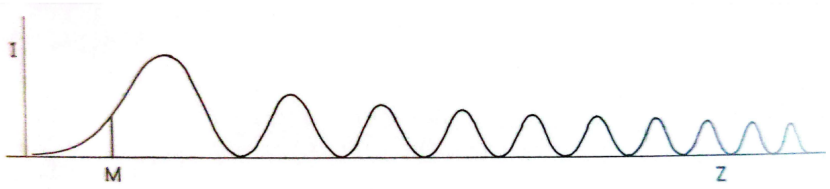

Figure 2.11: Graph of the Airy Rainbow Integral, M represents the Descartes ray, the parameter m is represented as z [77].

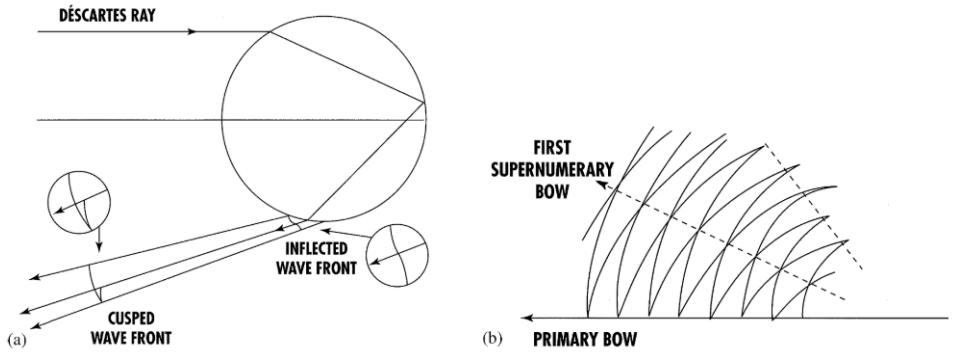

Figure 2.12: a) The cusp-shaped wavefront as it emerges from the raindrop. (b) The interference between the two branches of the cusp-shaped wavefronts (shown significantly exaggerated) is likely to give rise to the supernumerary bows [2][77].

Tricker [77] presented an approach made by J.M. Pertner to superimpose colour from the Airy rainbow curves for different wavelengths. A dependency of rainbow colour and width was found for varying particle sizes as seen in Figure 2.13. The width of the rainbow increases with decreasing particle size. In addition, as the particle size decreases, the colours become paler. Eventually, this leads to the creation of so-called white rainbows or fog bows. For large droplets, the light in the primary rainbow is more intense, and supernumerary arcs are close to the primary rainbow. Smaller droplets lead to supernumeraries spaced further apart from the primary, with dark bands separating them.

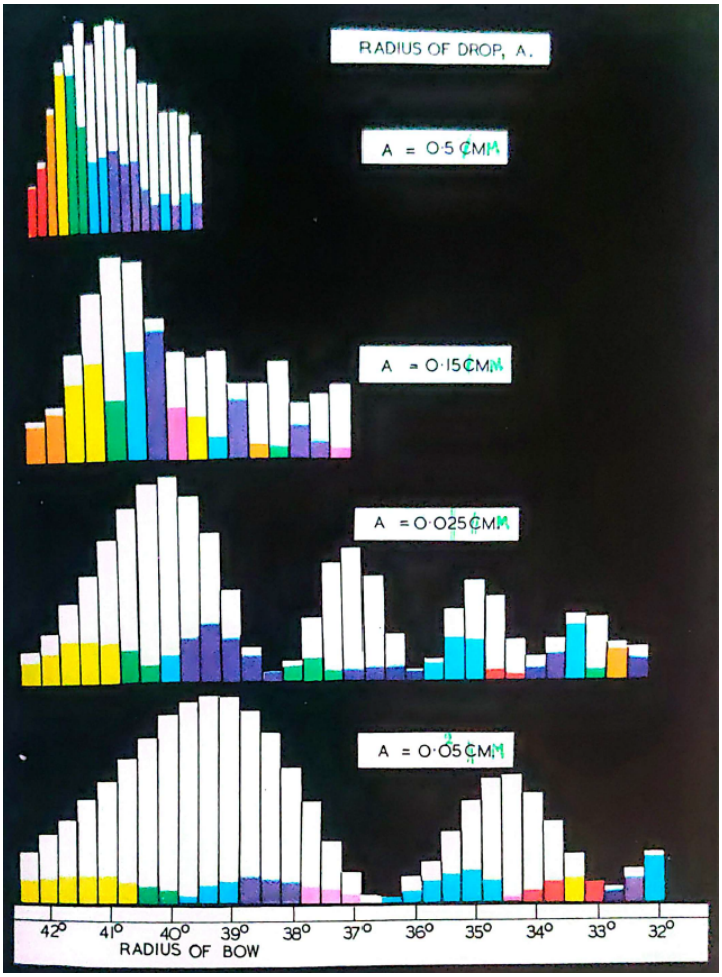

Figure 2.13: Colour approach on primary and supernumerary rainbows for varying droplet size from Airy theory by J. M. Pertner [77]

2.1.5. The Glory or Anti-Corona

This phenomenon is seen when the shadow of the observer is cast upon a cloud and consists of one or more coloured rings surrounding the observer's head as shown in Figure 2.14. The glory is also called the anti-corona as the scattering angle from the glory is $180°$ compared to $0°$ for the corona. Another discrepancy between the two phenomena is that the origin of the glory cannot be explained through simple diffraction or geometrical optics. The science of the glory was only recently discovered by Nussenzveig [54]. A minor contribution could be explained by electromagnetic surface waves, as shown in the top part of Figure 2.15. This involves light rays skimming the surface of a droplet and undergoing a temporary transformation into electromagnetic surface waves. The light then traces the curved surface for short distances before entering and exiting the droplet. This process allows the light to undergo a deviation of 180°, ensuring that it returns in the same direction. However, it was found that the main contributor to the glory's bright intensity came from Mie resonances created by the "tunnelling" of light, as shown in the bottom part of Figure 2.15. Here energy "tunnels" into water

droplets from light rays that would, under normal circumstances, bypass the droplets entirely. At the edge of the droplet, the electric and magnetic fields that make up the light waves do not totally vanish. Rather, the fields continue to extend a brief distance beyond the surface, creating evanescent waves. These evanescent waves make the electromagnetic field around the drop vibrate. This vibration is experienced by the medium just outside the drop and allows energy to tunnel through. Tunnelling is a prevalent phenomenon in waves of various types, manifesting in both quantum and classical physics. [54].

Figure 2.14: Glory on cloud observed from a passenger on an aircraft

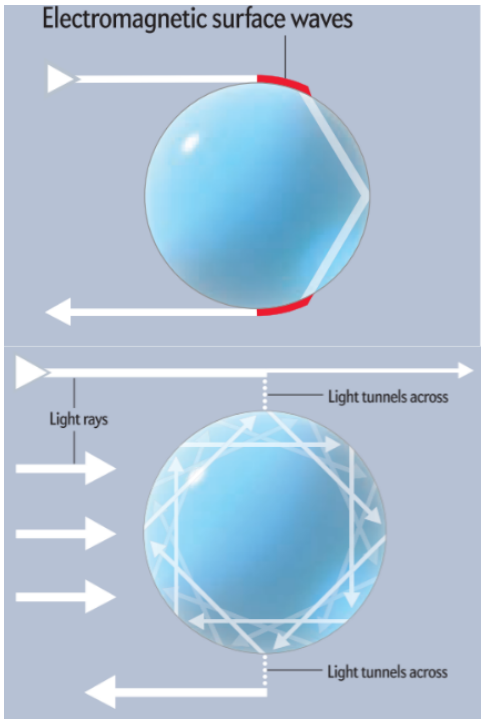

Figure 2.15: Light rays deviated 180° from surface waves (top) and light tunnelling (bottom) [54].

2.1.6. Mie Theory

In subsection 2.1.5, the glory phenomenon can be modelled through Mie theory. This theory, written by Gustav Mie [50], encompasses the solution of light scattering by small spherical particles beginning from Maxwell's equations. Moreover, it can model all of the aforementioned optical phenomena except ice particle haloes (as these originate from non-spherical particles). Mie Theory will prove to be an essential tool in this research due to its accuracy and flexibility. Understanding the full derivation of the theory itself is beyond the scope of this research as it encompasses exceptionally difficult and lengthy mathematics. Therefore, this section provides a basic overview of the inputs and outputs of the theory based on explanations provided by Mobley [51]. The main assumptions in the problem statement are:

- A single homogeneous sphere of radius ρ with a dielectric material that has a complex index of refraction $m_s = n_s + ik_s$ is considered. Here n_s is the real index of refraction, and k_s is the complex index of refraction of the sphere. The complex index directly influences the absorption coefficient a_s of the sphere material by $a_s(\lambda) = 4\pi k_s(\lambda)/\lambda$ with λ being the wavelength in vacuum of the electromagnetic wave with frequency v.
- An infinite, non-absorbing, homogeneous medium is considered in which the sphere is embedded. The index of refraction of the medium is $m_m = n_m$.
- An electromagnetic plane wave with frequency v is incident on the sphere. The wavelength of the light in the medium is $\lambda_m = \lambda/n_m$.

The goal is to identify the electric field within the sphere and its surrounding medium. That is, information on how the sphere absorbs and scatters incident light, as well as the angular distribution

and polarization state of the scattered light. The geometry for Mie theory is given in Figure 2.16. The origin of the coordinate system is selected so that the wave function is a cosine at time zero and so that the wave is propagating in the positive z-direction.

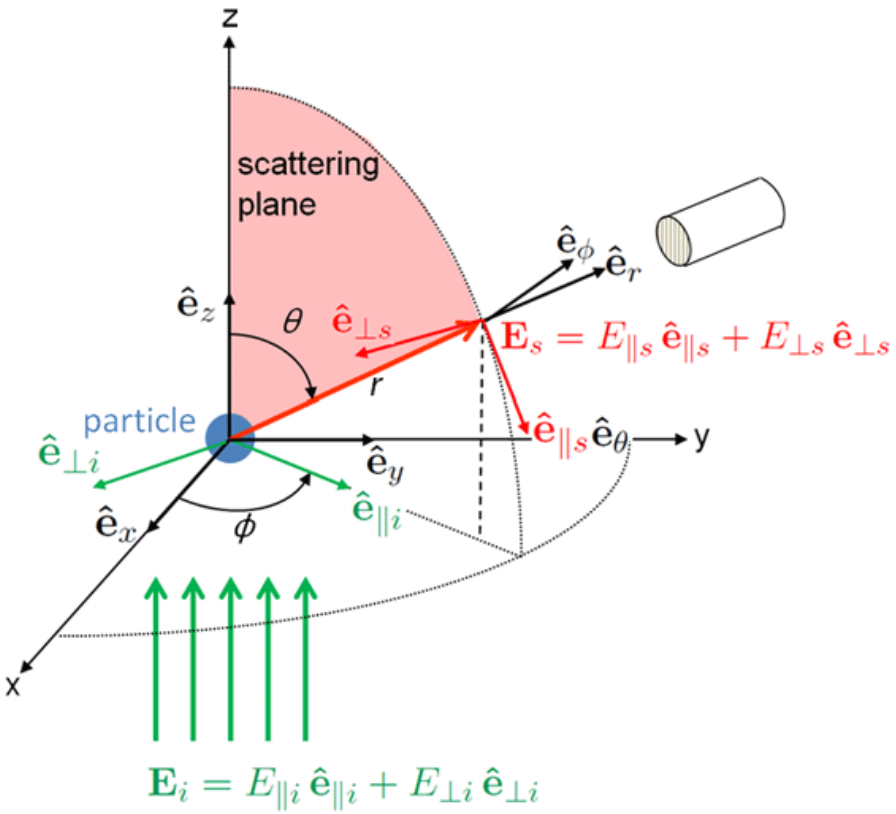

Figure 2.16: Mie theory geometry. The incident plane wave is represented by the thick green arrows, while the scattered wave is represented by the thick red arrows. The blue sphere at the origin is the scattering particle. Unit direction vectors are indicated with hatted letters [51].

In the medium with a real index of refraction, the incident electric field can be expressed according to Equation 2.9. Here $k = 2\pi/\lambda_m = 2\pi n_m/\lambda$, which is the wavenumber (cycles/meter) in the medium. $\omega = 2\pi v$ is the angular frequency (radians/second). $\mathbf{E}_{oi}$ is the amplitude of the incident electric field vector and t is time. Only the electric field is discussed, as the magnetic field naturally follows from it.

$$\mathbf{E}_i(z,t) = \mathbf{E}_{oi} e^{i(kz-\omega t)} \tag{2.9}$$

Since light travels in a transverse electromagnetic wave, its magnetic and electric fields are perpendicular to its direction of propagation. Additionally, the incident wave is polarised arbitrarily. Two components that are orthogonal to the direction of propagation can be combined to represent an arbitrary state of polarisation of $\mathbf{E}_i(z,t)$ as seen in Equation 2.10. These two orientations are chosen to be perpendicular to the scattering plane and parallel to it. The scattered field becomes transverse at vast distances from the particle (referred to as the ”far field”) and may also be expressed as a combination of components in directions perpendicular and parallel to the scattering plane as in Equation 2.11.

$$\mathbf{E}_i = E_{\parallel i}\hat{\mathbf{e}}_{\parallel i} + E_{\perp i}\hat{\mathbf{e}}_{\perp i} \tag{2.10}$$

$$\mathbf{E}_s = E_{\parallel s}\hat{\mathbf{e}}_{\parallel s} + E_{\perp s}\hat{\mathbf{e}}_{\perp s} \tag{2.11}$$

The solution for the scattered wave from a non-spherical and/or non-homogeneous particle at the origin becomes Equation 2.12. S_j with $j = 1, 2, 3, 4$ are the entries of the amplitude scattering matrix. The amplitudes of the incident electric field are converted into the amplitudes of the scattered field

through these functions. The amplitude scattering matrix has four non-zero members that are dependent on both the azimuthal and polar scattering angles. Naturally, the size, shape, and composition of the particles, as well as the incident light's wavelength, affect these entries [51].

$$\begin{bmatrix} E_{\parallel s} \\ E_{\perp s} \end{bmatrix} = \frac{e^{ik(r-z)}}{-ikr} \begin{bmatrix} S_2 & S_3 \\ S_4 & S_1 \end{bmatrix} \begin{bmatrix} E_{\parallel i} \\ E_{\perp i} \end{bmatrix} \tag{2.12}$$

In case of homogeneous and spherical particles $S_3 = S_4 = 0$ resulting in Equation 2.13. The incident and scattered electric fields must meet Maxwell's equations and boundary conditions for them to work correctly at the sphere's surface and interior. These boundary conditions indicate which specific electric field—among all those that could meet Maxwell's equations—is the one that best characterises scattering by a given sphere.

$$\begin{bmatrix} E_{\parallel s} \\ E_{\perp s} \end{bmatrix} = \frac{e^{ik(r-z)}}{-ikr} \begin{bmatrix} S_2 & 0 \\ 0 & S_1 \end{bmatrix} \begin{bmatrix} E_{\parallel i} \\ E_{\perp i} \end{bmatrix} \tag{2.13}$$

There are two inputs for the scattering matrix entries. First, the size parameter x given in Equation 2.14 shows the relative size of the spherical particle compared to the wavelength. The second input is the refractive index of the sphere relative to the surrounding medium, as shown in Equation 2.15.

$$x = \frac{2\pi\rho}{\lambda_m} = \frac{2\pi\rho n_m}{\lambda} \tag{2.14}$$

$$m = \frac{n_s}{n_m} + i\frac{k_s}{n_m} \tag{2.15}$$

Equation 2.16 shows the solution of Mie. Here, a_n and b_n are the "Mie Coefficients" which describe multipole expansions of the electric and magnetic field respectively. τ_n and π_n are functions which depend on the scattering angle, which is depicted as θ in Figure 2.16 and is independent of ϕ because of the spherical geometry of the particle. It is important to note that if the index of refraction of the sphere is equal to that of the medium, the Mie Coefficients reduce to zero and no scattering will occur. Therefore, it can be concluded that scattering is caused by differences in the index of refraction.

$$\begin{aligned} S_1 &= \sum_{n=1}^{\infty} \frac{2n+1}{n(n+1)} \left(a_n\pi_n + b_n\tau_n\right) \\ S_2 &= \sum_{n=1}^{\infty} \frac{2n+1}{n(n+1)} \left(a_n\tau_n + b_n\pi_n\right) \end{aligned} \tag{2.16}$$

Lastly, Mie theory is exact and valid for all sizes of spheres, indices of refraction and wavelengths [51]. However, it is not possible to analytically compute the sums of infinite series. Therefore, one resorts to numerical approximation for a finite number of terms. For x < 10, only a limited number of terms are needed to get accurate results. However, for particles much larger than the wavelength, a great number of terms is needed to reach convergence. The scattering phase function for unpolarised light is given by Equation 2.17 where S^* denotes complex conjugation. Here, the parallel scattered intensity is given by $I_{\parallel s} = |S_2|^2 = S_2 S_2^*$. The same can be said for perpendicular polarisation when considering S_1. The previous calculations assumed a single particle. In order to evaluate different particle types and distributions, the individual contributions must be added as shown by Mobley [51].

$$\widetilde{\beta} = \frac{1}{2}\left(|S_1|^2 + |S_2|^2\right) = \frac{1}{2}\left(S_1 S_1^* + S_2 S_2^*\right) \tag{2.17}$$

The scattering phase function from Mie theory can reveal the appearance, polarisation, and intensity of every optical phenomenon created from spherical particles. Laven [41] used Mie scattering to obtain the phase functions of the glory, corona and rainbow for varying particle sizes as shown in Figure 2.17. Mie scattering theory thus proves to be an exact and versatile tool for modelling optical phenomena. Therefore, it can be very valuable in the scope of this research.

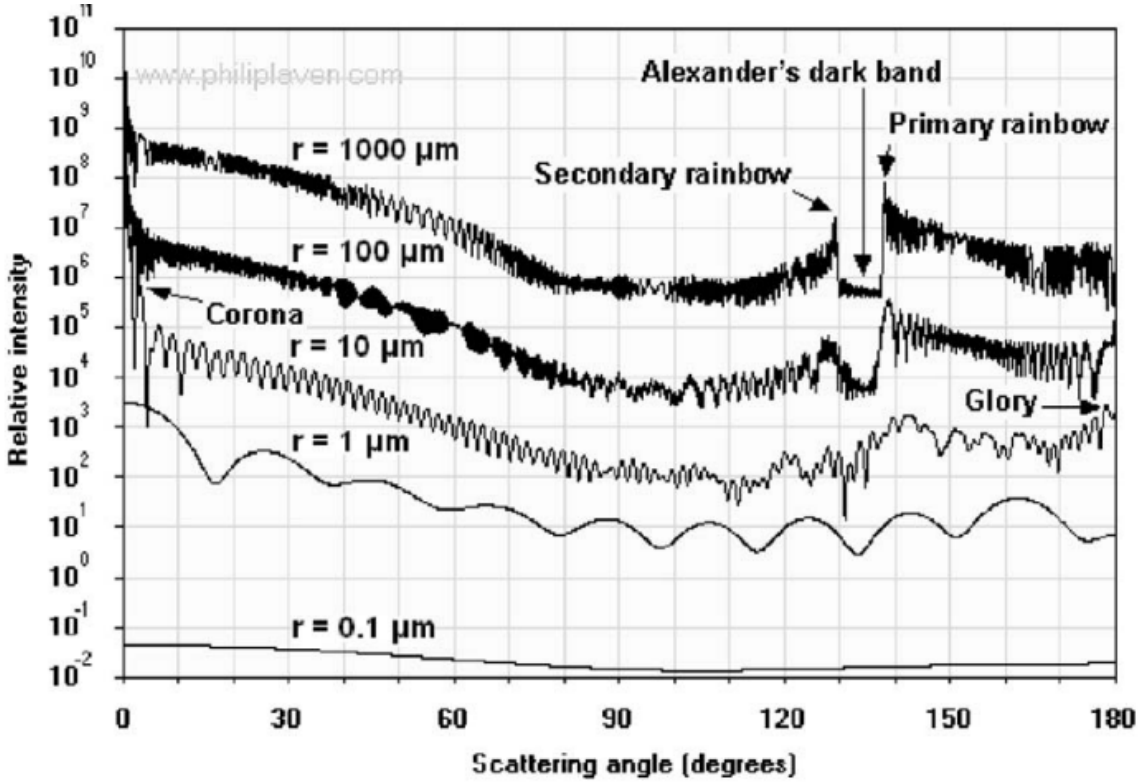

Figure 2.17: Mie theory calculations showing scattering of monochromatic light of wavelength 650 nm from spherical water drops with radius r = 0.1–1000 micron [41]

MiePlot Light Scattering Software

The aforementioned optical effects and scattering theories can be simulated by use of the MiePlot software made by Laven P. [41]. MiePlot is at its core a simple interface to the traditional BHMIE algorithm for Mie scattering from a sphere, as reported by Bohren and Huffman [7] in "Absorption and scattering of light by small particles". MiePlot not only calculates Mie scattering for single wavelengths, but it also calculates sunlight scattering and simulates atmospheric optical effects (such as rainbows, coronas, and glories). These simulations can be placed on digital photographs of real optical effects. Other theoretical approximations like geometrical ray tracing, Airy theory, Fraunhofer diffraction, and Rayleigh scattering can also be used. The Debye series is also available for computations with MiePlot. Mie theory does not shed any light on the physical mechanisms underlying the scattering of electromagnetic waves from a homogeneous sphere despite offering a precise mathematical solution to the problem. In essence, the Debye series is a reformulation of Mie theory that makes it possible to distinguish between contributions resulting from different ray trajectories. Many more features are available such as simulations for different particle size distributions, coated spheres, and varying refractive indices. A full overview of the program's capabilities is given on `http://www.philiplaven.com/mieplot.htm`. Example simulations of coronas, glories, and rainbows are given in Laven [41].

2.1.7. Optical Phenomena Beyond the Visible Spectrum

In previous sections, the appearance of atmospheric optical phenomena in the visible light spectrum (380 to 700 nm) was extensively discussed. However, as will be shown in section 2.4, the Cassini Imaging Science Subsystem (ISS) and Visual and Infrared Mapping Spectrometer (VIMS) can obtain measurements beyond these boundaries. The ISS has spectral sensitivities in the UV- and near-infrared regimes between 200-1050 nm (NAC). The VIMS is capable of observing spectra from 300 to 5100 nm which additionally covers the short and medium wave infrared range. These extended wavelength ranges allow for new unique observations of optical phenomena. An example is the significant reduction of Rayleigh scattering at longer wavelengths, leading to higher contrast observations [72]. On the other hand, it is known that water and water-ice have strong absorption features in the infrared [79]. The

attenuation of the transmission through water and ice is wavelength dependent as seen in Figure 2.18 (b) where a higher imaginary index of refraction (k) corresponds to stronger absorption. There are also strong variations in the real index of refraction (n) in the infrared range Figure 2.18 (a). For halos and rainbows (which rely on geometrical optics), this means that wavelength-dependent scattering angles can be vastly different and thus lead to different observing geometries. In this section, an answer to the question if the attenuation is sufficiently small to still observe the different optical phenomena in section 2.1 will be given. The expected appearance of these phenomena in the (near-)infrared range will also be discussed.

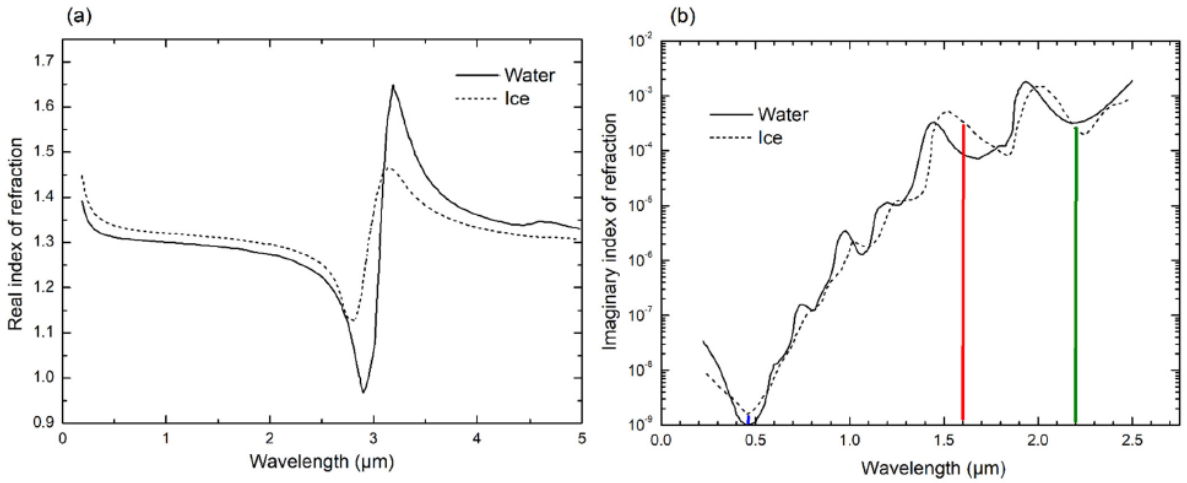

Figure 2.18: Real (a) and imaginary (b) index of refraction for water and ice with wavelengths; the vertical blue, red, and green lines correspond to absorption at 0.46, 1.6, and 2.2 μm, respectively [81]

Rainbow attenuation in the (Near-)Infrared

Strong absorption characteristics are seen in ice and liquid water within the thermal infrared spectrum. For instance, it is already possible to effectively block any light with a wavelength longer than 6 μm and significantly attenuate shorter wavelengths with a thin water sheet of 100 μm. The radiation that creates rainbows or the simplest refraction halos flows through liquid water or solid ice, hence the path length traversed by both substances determines the wave-length-dependent attenuation [79]. Raindrops range in size from 0.5 to a few millimetres [79]. Rainbow rays have internal path lengths of approximately 2.6 R for a droplet with radius R. For example, 0.5 mm, 1 mm, and 3 mm internal paths correspond to raindrops with diameters 0.38 mm, 0.77 mm, and 2.3 mm, respectively. Looking at Figure 2.20 (a), even with the greatest drop of 2.3 mm, the lowest transmission at the relevant wavelength is above 87%. Therefore, even large raindrops will not considerably attenuate the NIR radiation that may give birth to rainbows. Notably, the maximum absorption in the NIR at around 975 nm corresponds to the maximum imaginary index of refraction in Figure 2.18 (b). Figure 2.20 (b) shows internal transmission for wavelengths ranging from UV to 3 μm. Rainbows can be visible in nature or in the lab at wavelengths ranging from 190 nm up to 2.5 μm due to water absorption.

Glory attenuation in the (Near-)Infrared

Smaller droplets, such as 10 μm cloud droplets, cause glories. In a blended geometrical and wave optics depiction of glories, the rays would follow rainbow-like patterns as well as surface/interface waves along the drop perimeter. The path length for such rays is approximately 3R in droplets of radius R. Figure 2.20 (c) depicts internal transmission in water drops with ray path lengths ranging from 10 to 50 μm, similar to droplets with a diameter of 7-33 μm. Again, there is less attenuation in the NIR spectrum. However, small cloud drops, unlike bigger raindrops for rainbows, can exhibit thermal infrared glories up to 12 μm wavelength with sufficient radiation for scattering. Vollmer [78], set 0.01 as the upper limit of the imaginary index of refraction for pure water ice where glories could be visible (only a single ring). This sets a limit to the range of wavelengths for which water droplet glories may be observed. As seen in Figure 2.19, these windows are approximately 0.17 μm to 2.68 μm, 3.50 μm to 4.39 μm and 5.24 μm to 5.35 μm. Obviously, these limits are somewhat arbitrary, depending on the choice of the limiting value for the imaginary index of refraction.

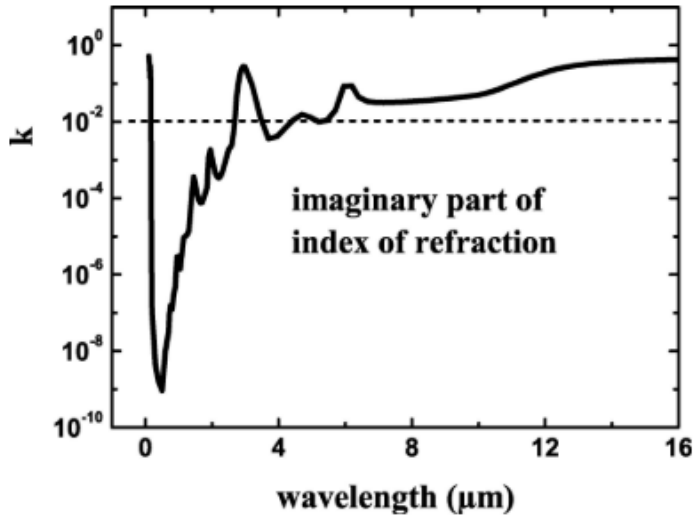

Figure 2.19: Imaginary part of index of refraction of pure water: $k \leq 10^{-2}$ defined as wavelength ranges where glories should be visible [78]

Halo attenuation in the (Near-)Infrared

Similarly, for halos, one can look at the internal transmission through the ice for realistic path lengths as shown in Figure 2.21 (a). Halo-forming ice crystals typically measure 10-100 µm [79]. Again, the maximum absorption in the NIR range at 1050 nm corresponds to the maximum imaginary index of refraction in Figure 2.18 (b). Rays in hexagonal ice crystals with facet length d will have ice ray path lengths ranging from d to $2d$. A perfect hexagonal crystal would have a size of $\sqrt{3}$ =1.73d, based on the distance between two parallel facets of common ice crystals. The values for 20 µm and 100 µm ray pathways correspond to crystal diameters of 23 µm and 115 µm, respectively. Since the internal transmission in ice is above 99.5% for a 100 µm path and remains above 97% for a 1 mm path in the NIR, it can be concluded that attenuation of radiation through ice will not significantly affect NIR refraction halos [79]. Figure 2.21 (b) shows the transmission through ice further in the infrared range from the UV (150 nm) up to 12 µm. With absorption being the limiting factor, refraction halos with path lengths of 20µm can be observable from 175 nm (UV) up to about 11 µm in the long-wave infrared (LWIR). Only the strong absorption band near 3 µm will completely attenuate the halo signal [79].

Corona attenuation in the (Near-)Infrared

To investigate the absorption at longer wavelengths, one can also look at the behaviour of strongly absorbing particles/droplets (as are water droplets in the thermal IR) of arbitrary materials. This is exactly what Vollmer [78] did. From Mie theory calculations, no major changes in the appearance of coronas are expected. This behaviour makes sense in the context of the flat mask projection of diffraction theory, which assumes that two-dimensional disks can approximate three-dimensional droplets. This is because the typical representation of water droplets is of transparent disks in an opaque screen, but strongly absorbing droplets correspond to opaque disks in a transparent screen. Babinet's principle states that in the Fraunhofer diffraction theory, the corresponding diffraction patterns have the same appearance [78].

As seen in Figure 2.22, the difference in the corona diffraction pattern of a water droplet m =1.3318, various aerosols, and highly absorbing droplets. m =1.3318+i1000 is not particularly pronounced for a normal size distribution with a =10 µm and σ =0.5 µm. The position of the first two to three maxima is not altered by modifying the real part. Increasing the imaginary component somewhat decreases the intensity of the rings. For aerosols (k=0.45) and entirely absorbing droplets (k=1000), the first two rings of the corona should remain visible. Stronger absorption obscures the diffraction ring pattern at higher orders. However, because most natural observations contain less than three ring sequences, the impacts of absorbing particles can be practically viewed as insignificant for coronas [78]. Nevertheless, looking at very minute particles (a =1 µm) in Figure 2.23, it was found that the ring outside of the aureole is only visible for water droplets. The primary characteristic of absorption for these minute particles is

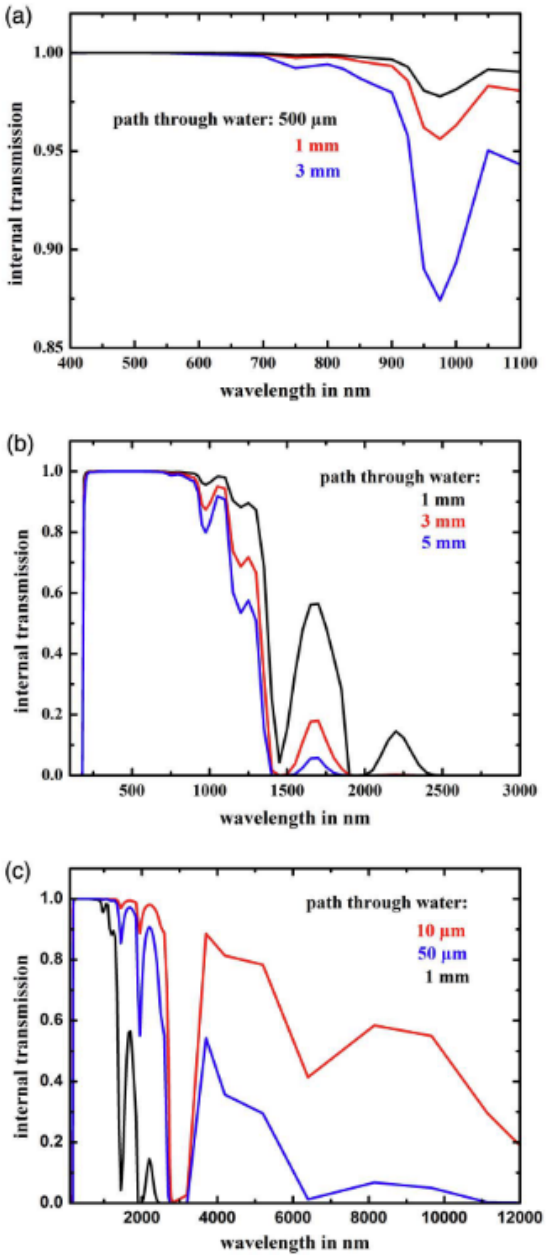

Figure 2.20: (a) VIS-NIR transmittance for rainbow path lengths; (b) VIS-SWIR transmittance for rainbow path lengths; (c) VIS-LWIR transmittance for glory path lengths (1mm included for comparison) [79].

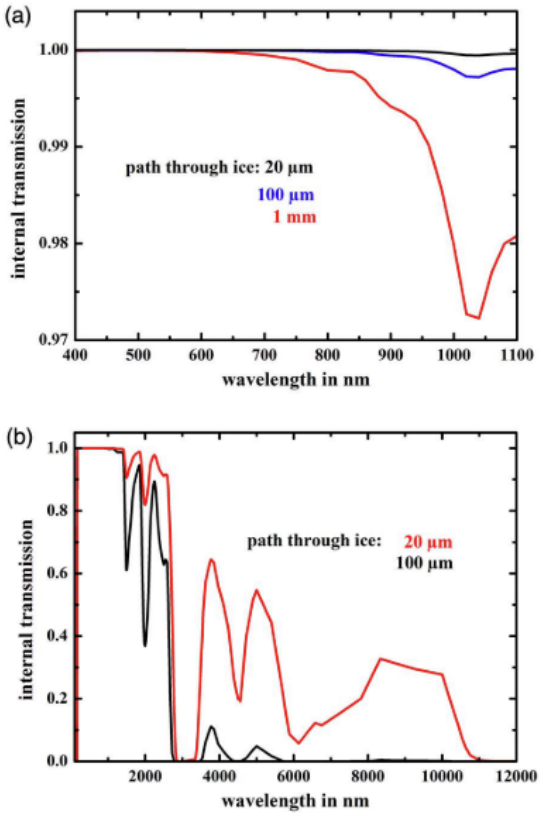

Figure 2.21: Transmission spectra through ice for VIS-NIR region (a) and from UV to 12 µm (b).

the effective suppression of the corona's higher-order diffraction rings. In this case, detection windows could be determined based on a maximum k, just like for the glory.

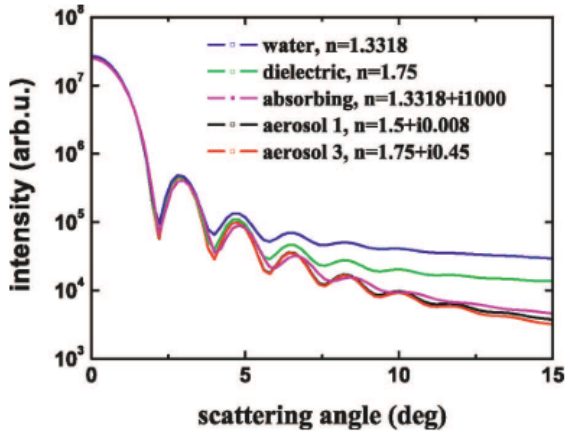

Figure 2.22: Forward scattering for spheres with a normal size distribution (a =10 µm and σ =0.5 µm) at $\lambda = 650$ nm as a function of the index of refraction [78].

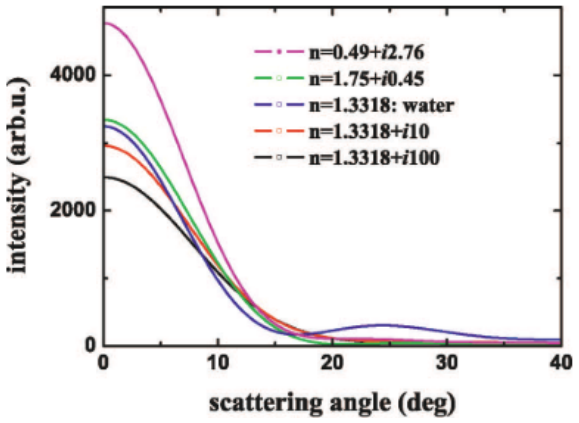

Figure 2.23: Forward scattering for spheres with a normal size distribution (a =1 µm and σ =0.1 µm) at $\lambda = 650$ nm as a function of the index of refraction [78].

(Near-)Infrared Observations of Optical Phenomena

As different wavelengths have different refractive indices through the same medium, expanding the observed spectrum for optical phenomena will likely alter their appearance. In this subsection, NIR images of different optical phenomena will be shown. Rainbows and refraction halos can be easily seen in the visible spectral region due to their distinct colour spread with scattering angles. Monochrome detection in the NIR lacks this information, requiring detection by brightness variation against the background. A uniformly dark background is desired. It is important to note that a dark background in the VIS can be bright in NIR or IR. In addition, the NIR spectrum shows a strong absorption characteristic for water molecules between 900 and 1000 nm. However, the spectral characteristics are narrow, affecting just a small portion of the NIR band. Detecting wide-band NIR radiation between 800 nm and 1100 nm may result in only a minor drop in image brightness [72].

Figure 2.24, shows the comparison between photographs of optical phenomena taken in the visible and wide-band near-infrared spectrum. For the rainbow, the NIR primary rainbow angle at 900 nm is approximately 42.7°, which is within 1° of the VIS rainbow angles (42.0° at 600 nm). The corresponding secondary rainbow shifts from 51.0 to 49.7° [72]. These minor shifts in position correspond to little change in the index of refraction for the NIR compared to the VIS as seen in Figure 2.18 (a). From this figure, it is also clear that the rainbow angle can drastically change when going beyond the NIR and VIS spectra. Using Equation 2.6 with refractive indices of water for wavelengths in the UV till 5 µm can result in rainbow angles ranging from 24° up to 80°.

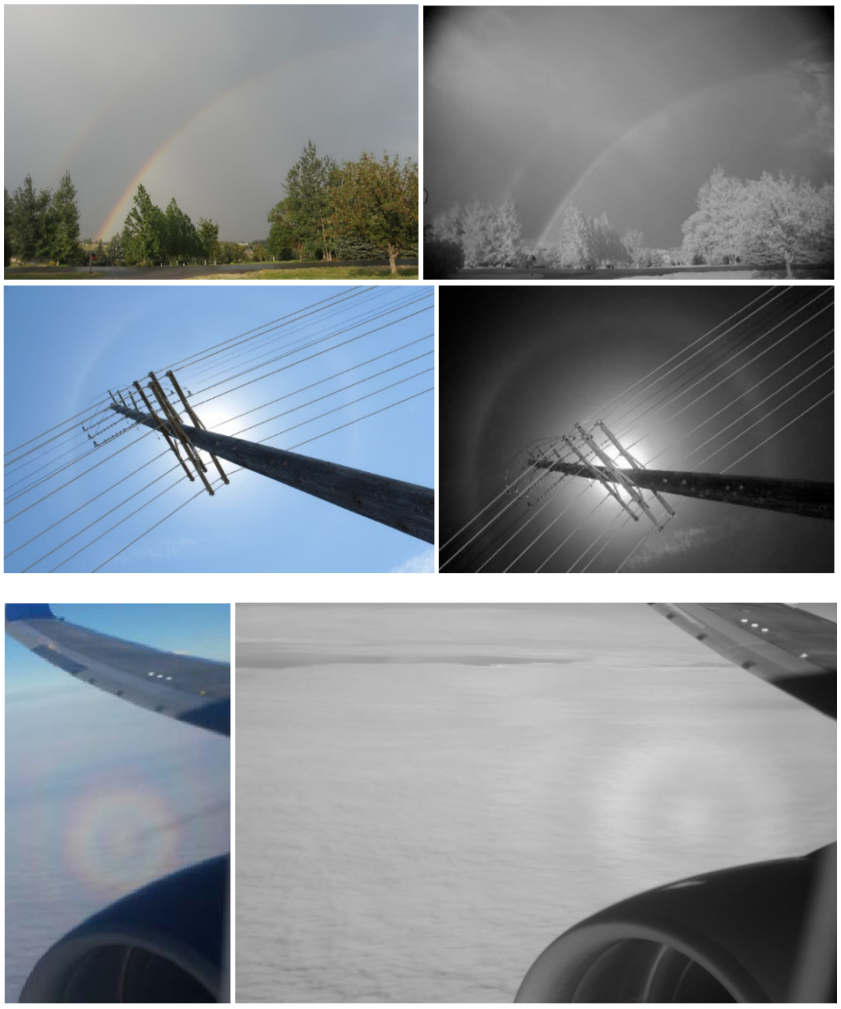

Figure 2.24: photographs in the VIS (left) and NIR (right), top: rainbow, middle: halo, bottom: glory [72]

Similarly to the rainbow, the halo also experiences a small angular position shift in the NIR due to variation in the index of refraction. However, the shift of the inner ring edges between red light at 650 nm and NIR radiation at 850 nm is only roughly 0.3° due to the extremely tiny dispersion of ice. Interestingly, reduced Rayleigh scattering in the clear sky at NIR wavelengths enhances the contrast between the sky and clouds, resulting in a more visible halo [72].

The glory is displayed as a sequence of at least three different coloured rings in the visible spectrum. The NIR glory with up to three bright rings is also visible in the corresponding original NIR photo Figure 2.24 (bottom). The difference in brightness between the highest and lowest brightness is only a few per cent, but the rings are still clearly visible. The angular size of the glory rings increases with wavelength, and this is the most noticeable difference between the glories in the NIR and VIS. When compared to the outer edge of the first red ring in the VIS image, the angular size of the first NIR glory ring's outer edge increased by roughly 30% [72]. According to Vollmer and Shaw [79], no images of coronas have been reported in the NIR or in the longer-wavelength thermal IR range. From Mie theory calculations, there would be no significant alterations in the appearance of coronas even for highly absorbing particles [78].

2.1.8. Summary of Optical Phenomena

Table 2.1, shows an overview of the main findings in this section. Diagrams depicting the expected observed angular geometry rainbow, halo, corona, and glory are presented in the first column. The geometries can change drastically with the properties of the medium. Therefore, it was decided to base

the interactions of light with particles consisting of pure water or water-ice (halo). Particle size effects on the angular size were taken into account by assuming geometries for the maximum range of particles for which the optical phenomenon is visible. The expected appearance of the optical phenomenon is depicted in the lower left corner. The second column shows the interaction of the light rays with the particle to create the optical displays. The third column shows a summary of the constraints like optical thickness, particle size, and phase angle for observing the phenomena, as well as additional characteristics like polarisation and appearance.

Table 2.1: Summary of the main characteristics of optical phenomena on Earth. Values are assumed for typical conditions in the Earth's atmosphere in the visible spectrum.

Observer Geometry	Ray-Particle Interaction	Characteristics
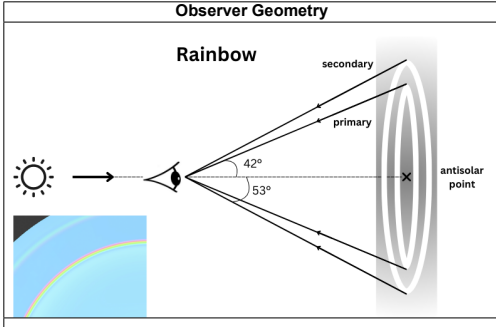	Geometrical optics, refraction and reflection [11]. 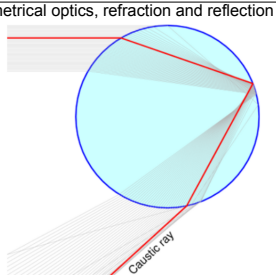	• Optical thickness [23]: min: $\tau \geq 0.0003$ (primary), $\tau \geq 0.003$ (secondary), peak: $0.1 \leq \tau \leq 3$ • Particles: spherical liquid water droplets, $a > 35\mu$m $\rightarrow$ rainbow, $a \leq: 35\mu$m$\rightarrow$ fogbow, secondary visible for $a > 10\mu$m, more details in Figure 2.25 [45] [41]. • Polarisation: 96% $\parallel$, 4%$\perp$ [77] • Phase angle range: 30°-42° (primary), 50°-60° (secondary)[45] • Appearance: both colourful with the primary bow being the brightest. Dark band between both bows. Fog bows are paler [41]. (picture [23])
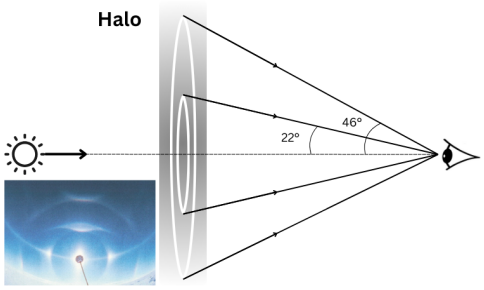	Geometrical optics, refraction and reflection [20]. 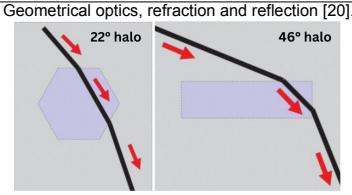	• Optical thickness: peak for $\tau \leq 1$ [24], for ~10% contrast, >1% of τ_{total} from halo-forming ice [44] • Particles: Hexagonal ice prisms, size parameter $2\pi L/\lambda \geq 80$ [5], $L \geq 11\mu$m [69] [24][44] • Polarisation: negligible for 22° features, 46° features have 15-20% radial polarisation [38] • Phase angle range: $\pm 134°$ & $\pm 158°$ • Appearance: 22° halo: red near the sun, followed by orange, yellow and paler colours. 46° halo: fainter but more colourful with the same colour sequence. Other more rare elements may be observed (see [77][38][52]) (picture [20])
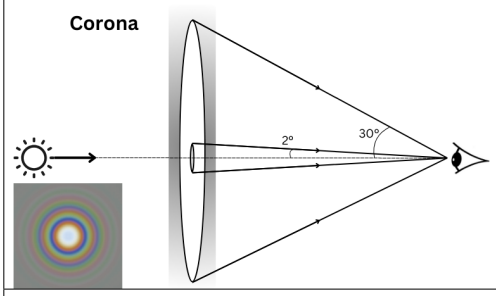	Wave theory, diffraction [13]. 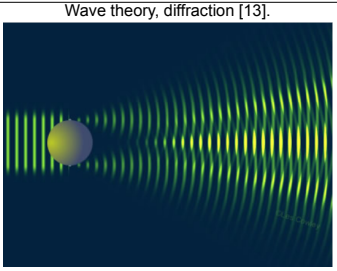	• Optical thickness: minimum for white aureole with blue sky background $\tau \geq 0.001$, peak colour purity $0.05 \leq \tau \leq 0.5$ [22] [69] • Particles: water- or ice-clouds, 1μm $\leq a \leq 20$ μm [69][22], narrow size distribution [22] • Polarisation: None [38] • Phase angle range: strong dependence on particle size, max range: 150°-178° [69] [22] [41] • Appearance: Bright central aureole encircled by concentric rings with decreasing light intensity and colour purity [22] (picture [22]).
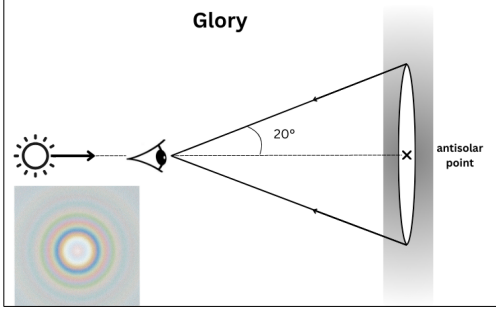	Wave tunnelling and surface waves [54]. 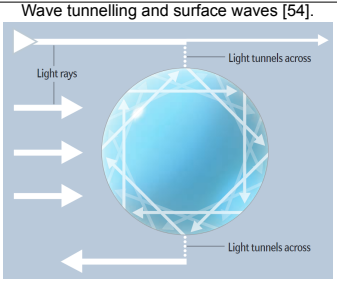	• Optical thickness: peak $\tau \sim 0.25$, range with skylight included $0.1 \leq \tau \leq 1$ (τ_{max} ≈3 without skylight)[21] • Particles: spherical liquid drops, narrow size distribution [38][54] [46], distinct for size parameters 10-300 ($2\pi a/\lambda$)[21] • Polarisation: rings are radially polarised, white area near centre is tangentially polarised [38] • Phase angle range: 0°-20°[21] • Appearance: a multicoloured-light halo surrounding the observer's shadow [54] (picture [22])

2.2. Exploitation of Optical Phenomena for Particle Characterisation

After discussing the many optical phenomena that could potentially exist on Enceladus, it is crucial to look at what they can reveal about the physical characteristics of the substance from which the optical

phenomenon originated. First, the variations observed in rainbows with droplet size will be discussed in subsection 2.2.1. Secondly, in subsection 2.2.2, a relation between the size of the corona rings and particle size will be shown. Next, an application of cloud droplet size estimation from airborne observations of a glory will be presented in subsection 2.2.3. In subsection 2.2.4 and subsection 2.2.5, optical phenomena observed in space are reported for Venus (glory) and for Mars (halo), respectively.

2.2.1. Rainbow & Fog Bow Variation with Droplet Size

Lynch and Schwartz [45] characterised rainbow properties for different particle sizes using Mie scattering theory. Their main findings are shown in Figure 2.25 and summarised below. The contrast of the bows is defined as $c = \frac{I_P - I_A}{I_A}$, where I_P is the peak brightness and I_A is the mean brightness of Alexander's dark band. From particles with radius a = 3 µm to a = 10 µm, the primary bow shows a nearly constant contrast, but the secondary bow shows a low and probably undetectable contrast for $a < 10$ µm. Because the primary bow widens rapidly with decreasing drop size, its apparently constant contrast does not mean that it is always visible. To be detected, it must be seen against a uniform featureless background: high contrast, structured backgrounds will hide its subtle nature. The colour purity parameter is defined as $\phi = \frac{S}{W}$, where S is the angular separation of the peaks of the red and blue bows, and W is their average angular width (full width at half-maximum, FWHM). If $\phi = 0$, the colours totally overlap, and the bow is white, while values of s exceeding 1 represent colourful bows [45]. In addition, this research set the definition of a fog bow as any rainbow formed in particles smaller than $a = 35\mu$m. Additional trends and observations from Figure 2.25 are listed below:

1. The rainbow width is minimal for $a = 100$ µm.
2. The supernumerary bows associated with the primary reach their highest visibility when a is equal to 50 µm.
3. The width of Alexander's dark band of 9.5° remains constant for varying drop sizes.
4. The peak linear polarisation of both bows fluctuates with the size of the droplets.
5. The secondary fog bow becomes observable only when a is greater than 10 µm.

2.2.2. The Corona, Particle Sizing from Angular Size of Rings

Laven [40] made a comparison between Fraunhofer diffraction and Mie scattering simulations applied on the atmospheric corona. When the droplet radius (a) is greater than 3 µm, Fraunhofer diffraction offers a suitable explanation for the corona, exhibiting only minor discrepancies compared to calculations using Mie theory. The angular radius of the corona's circular rings is inversely proportional to a, allowing images of the corona to be utilised for determining the value of a. However, common misconceptions arise regarding the connection between the diffraction patterns for monochromatic light and the coloured rings of the corona produced by sunlight scattering. One frequently used approximation suggests that the red rings in the sunlight corona correspond to maxima in the diffraction patterns for red light. While this holds well for the second and third red rings, the sunlight corona possesses an additional inner red ring not predicted by diffraction theory. Consequently, employing diffraction theory can lead to an overestimation of particle sizes by a factor of approximately 1.9 compared to Mie theory. While Fraunhofer diffraction is attractive due to its mathematical simplicity compared to Mie theory, particle sizing based on simple formulas derived from diffraction patterns for monochromatic light can yield significantly misleading results. Therefore, it is recommended to base particle sizing on Mie theory simulations of sunlight scattering. The discrepancies between diffraction theory and Mie theory become clear from Figure 2.26. Results are similar in both models for droplet radius greater than 3 µm. However, for smaller particles different colour sequences are seen in the rings which are ignored in diffraction theory. Figure 2.26 (b) reveals that the three inner red rings of the corona have angular radii of $\theta_1 \approx 16/a$, $\theta_2 \approx 31/a$, and $\theta_3 \approx 47/a$, where θ is measured in degrees and a is measured in µm. Additionally, it was found that the appearance of the corona is independent of the refractive index of the particles. Lastly, the rings can become unidentifiable for larger particle size distributions and are most recognisable for mono-disperse particles. For narrow distributions the rings appear to retain an angular radius respective to the mean particle size.

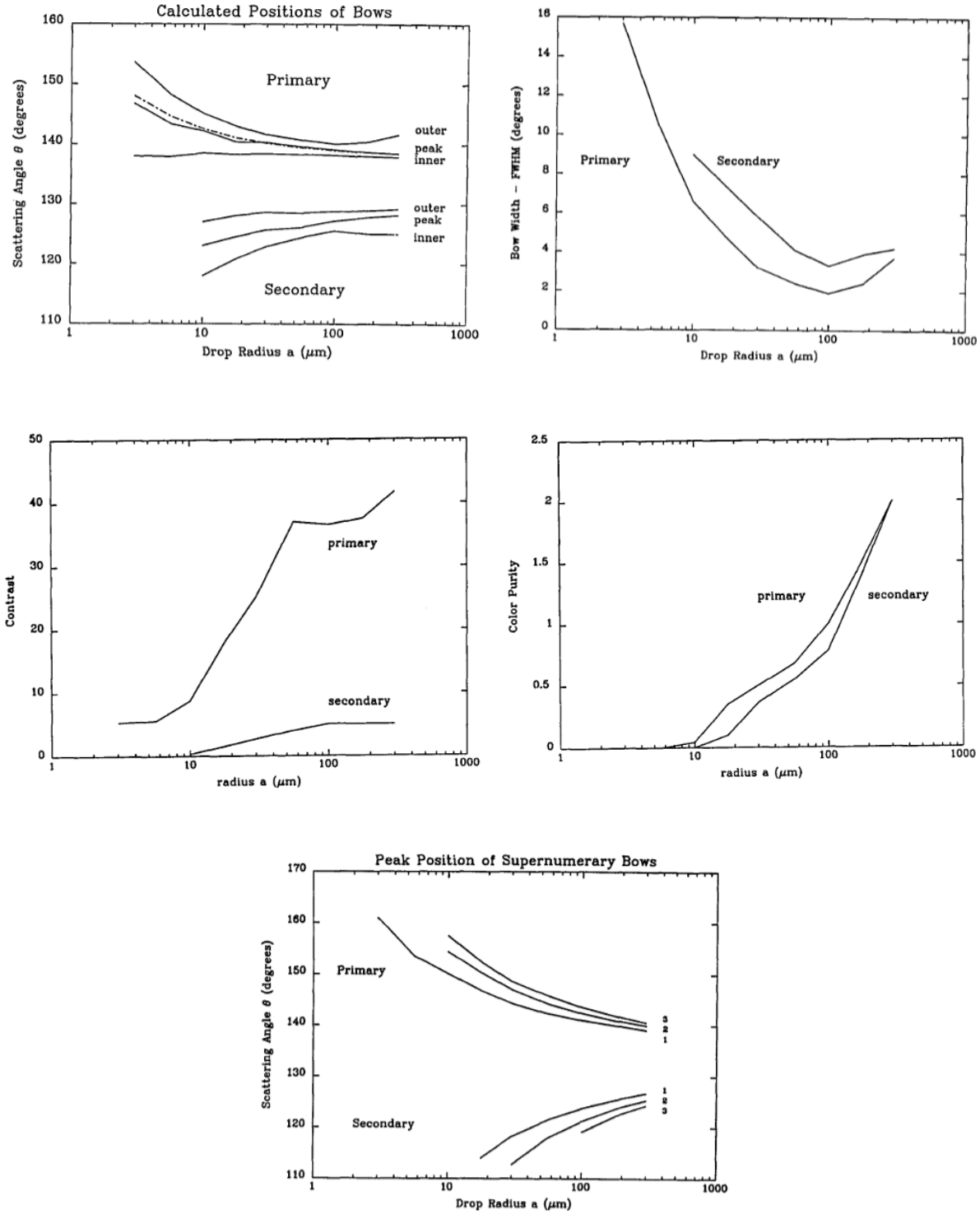

Figure 2.25: Primary and secondary rainbow properties for varying raindrop particle size [45].

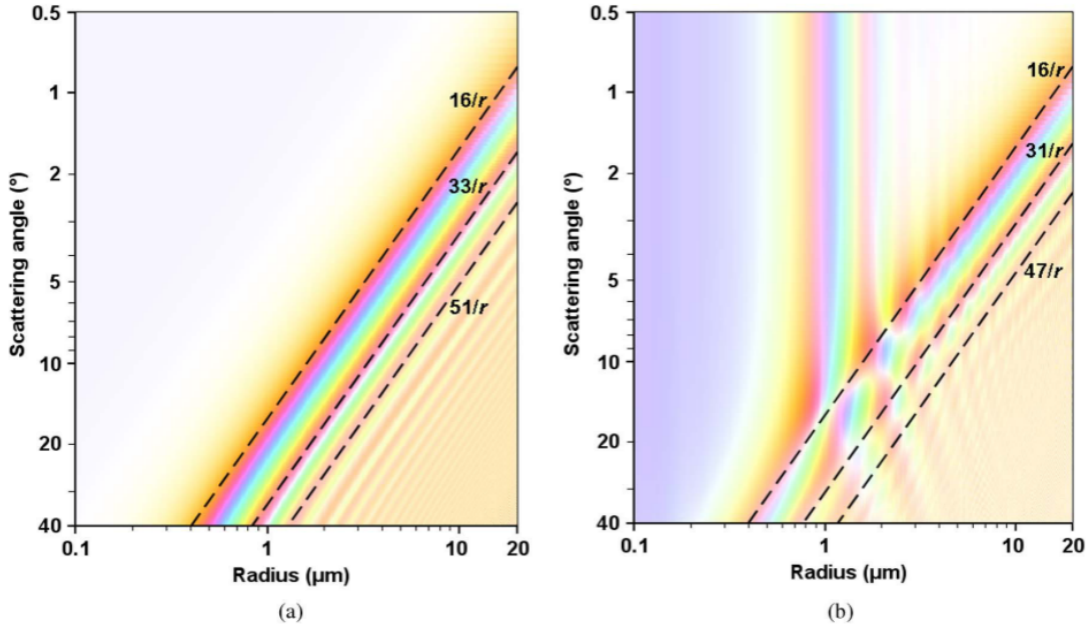

Figure 2.26: Lee diagrams showing the saturated colours of the corona vary with radius, r, of a spherical droplet of water. Diagram (a) shows the result of calculations using diffraction theory, while (b) shows the result of calculations using Mie theory [40].

2.2.3. Airborne Remote Sensing of Water Cloud Droplet Size Distributions using the Backscatter Glory

Utilizing high spatial resolution (2.5 m) airborne cloud top observations, Mayer et al. [49] introduced a retrieval scheme enabling the simultaneous determination of optical thickness, effective radius, and the width of the droplet size distribution from data acquired at a single wavelength. The retrieval method is centred on the observation of the glory in the 180° backscatter direction at 753 nm. Through a combination of Mie calculations and radiative transfer simulations, it was demonstrated that an increase in optical thickness raises the average reflectivity without altering the characteristic appearance of the glory. The features of the glory are dependent on the effective radius and the width of the droplet size distribution. While the spacing of the maxima primarily correlates with the effective radius, the amplitude of the smaller side maxima is influenced by the width of the droplet size distribution. This research demonstrates how parameters such as effective droplet radius, particle size distributions, and optical thickness can be derived from glory observations using only a single wavelength.

2.2.4. Glory on Venus Cloud Tops

Markiewicz et al. [46] [58] [47] exploited images from the Venus Monitoring Camera (VMC) on board the ESA's Venus Express to observe a glory on Venus' cloud tops. A campaign to investigate Venus cloud tops in back scattering viewing geometry produced images in four narrow band filters with centre wavelengths at 0.365 (UV), 0.513 (Vis), 0.965 (NIR1), and 1.010 (NIR2) micron. Over a dozen orbits were used to repeat these observations. For illustration, data from July 24, 2011, orbits 1809 and 1920 are displayed in Figure 2.27. The right side of this figure shows three images taken of the Venus cloud tops taken in the three narrow-band filters. The white areas represent the peaks of the phase functions seen on the left; these correspond to the rings of the glory. The entire glory pattern may be seen in a single image only in the UV filter because the VMC frame displaying the glory has an angular width of around 15° in phase angle, and the angular positions of the maximum and minimum in brightness are closer at shorter wavelengths [46]. In this research, the phase dependency of brightness of particular regions (phase angles ranging from 0 to 60°) was computed using 26 photos taken in orbit 1809. The photos were taken between 11:00 and 12:00 h local solar time, in latitudes 8°N–8°S and longitudes 270°E–280°E. The entire sequence took 17 minutes. Although the image resolutions vary, the ones close to backscattering have roughly 4 km per pixel. Every image has a width of 256 pixels. Apart from these observations, the Pioneer Venus polarimetry data also observed the glory. According to

Markiewicz et al. [46], polarimetric observations are more sensitive to a thinner section of the reflecting layer than unpolarised data, which is the primary difference between glory observations in polarised and unpolarised light. Consequently, these observations delve a little bit deeper into clouds.

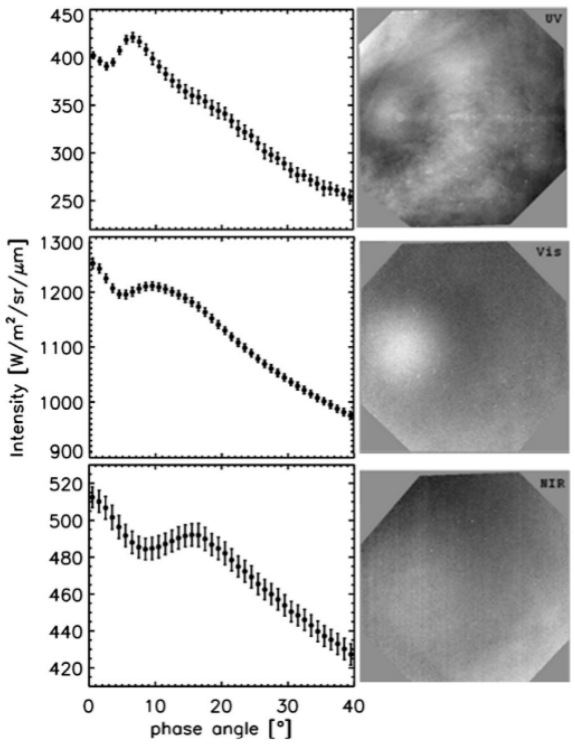

Figure 2.27: Venus glory as observed in three of the VMC channels (UV – 0.365 μm, Vis – 0.513 μm and NIR1 – 0.965 μm, top to bottom). Left: Averaged intensity as a function of phase angle (orbit 1809). Right: VMC images (orbit 1920). Error bars are one sample standard deviation [46]

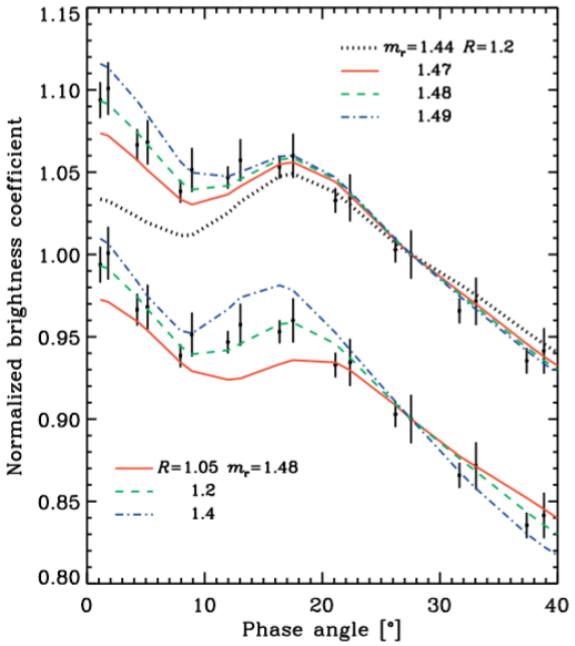

Figure 2.28: Normalized NIR1 brightness (vertical lines, two sets present the same measurements, but the lower one is shifted down by 0.1) compared with models of the cloud layer with the optical depth s = 30, composed of spherical particles with an effective radius of 1.2 μm with various refractive index values (upper set) and 1.48 refractive index with various radius values (lower set). The data are from photos taken in orbit 1809 and averaged across a 1° by 1° area centred at 274°E, 5°N [46].

It was stated that in order for a glory to exist, at least two conditions must be fulfilled. First, the cloud particles must be spherical, and their size distribution must be very narrow. The spatial scale of the glory displayed in Figure 2.27 is around 1200 km, showing that at least the upper layers of clouds are homogeneous in terms of cloud particle sizes on this scale. The dominating particle size of the cloud layer clearly and uniquely determines the spacing of the extrema [46].

The investigation focused on infrared pictures because of the sensitivity of brightness at shorter wavelengths to submicron haze and absorption, which can introduce additional characteristics. The research was successful in matching the minima and maxima with the single scattering phase functions of sulfuric acid droplets with an effective radius of 1.2 μm and an effective variance of 0.07, known to be present in the upper clouds of Venus. However, the relative difference between the primary and secondary maxima from the model did not match the observations. Variations in refractive indices and particle size were modelled from radiative transfer code as shown in Figure 2.28. The maxima are dictated by particle size and already matched well. Therefore, the only parameter that could be changed is the real index of refraction of the particles. Figure 2.28 demonstrates that increasing the refractive index to 1.48, which is significantly higher than the expected value for sulfuric acid droplets, provides an acceptable fit to data [46]. This increment was then related to cloud temperature and a mixture of a substance with a high refractive index in the form of haze or coating of particles using Mie theory [46].

2.2.5. Water-Ice Clouds on Mars Producing Halo Displays

The near-Sun geometry makes the halo often inaccessible to orbiting spacecraft. However, landers have more flexibility. Lemmon et al. [44] reported that several sensors on the Perseverance rover recorded a 22° scattering halo around the Sun for several hours around northern midsummer (solar longitude 142°) of Mars. This type of halo has never been observed outside of Earth. The halo required crystalline water-ice cloud particles in the shape of hexagonal columns that were large enough to allow for substantial refraction. The existence of halos establishes a lower bound on particle size since they are geometric-optics (refraction) features that do not exist for cloud particles that are small in relation to the wavelength as shown in subsection 2.1.2.

For the Martians clouds observations, the minimal cloud particle size in green light is L of 7–13 µm, at 866 nm, that is 11–21 µm. Therefore, a minimum estimate of 11 µm for the length and diameter is made. A 46° halo was not seen; this phenomenon is more prominent for plates ($L < D$) and less obvious for columns ($L > D$). This led to the assumption that the Martian clouds are likely being dominated by columns. It was also found that the halo-forming clouds need a high supersaturation of water which is why they are probably uncommon [44]. Farkas [18] also briefly discussed the outlook of possible halos in the solar system based on different ice types. The martian carbon-dioxide-ice particles have halos at 26° and 39° for example.

Roughness and diffraction (for small particles) can both smooth halos so that the peak brightness is not limited to 22°. Lemmon et al. [44] modelled an exponential fall off to larger angles and sharp inner edge characteristics of the geometric-optics halo. The data was fitted using a model that included parameters for the halo features' broadening, fall-off to large scattering angles, amplitude, and inner edge. This allowed to roughly estimate the roughness and particle size range. The differences in model fit can also be related to formation processes which result in more complex or irregular crystal shapes. Lastly, Yang et al. [82] estimated that more than 1% of the optical depth must contain halo-forming ice to get a halo with around 10% contrast. This is based on a factor of ten contrast. A bigger fraction with a lower-contrast halo (due to diffraction or roughness) is acceptable.

2.3. Enceladus' Plumes

As demonstrated in section 2.2, the properties of the particles that light interacts with have a significant impact on optical phenomena. Therefore, an overview of Enceladus' plume dynamics and consistency is necessary to locate and analyse these phenomena. In subsection 2.3.1, the abundance of gases in the plumes will be discussed, followed by the properties of solid particles in subsection 2.3.2. Next, in subsection 2.3.3, the locations and sources for the dynamics of the plumes will be presented. This section concludes with an overview of estimated particle size distributions shown in subsection 2.3.4.

2.3.1. Composition of the Gas Phase

The gaseous phase of the Enceladus plumes has been measured by two Cassini instruments: The Ion Neutral Mass Spectrometer (INMS) (in-situ) and the Ultraviolet Imaging Spectrograph (UVIS) (remote). UVIS used UV wavelengths of 110-190 nm for stellar occultations and 55-110 nm for solar occultations. The observations from stellar occultations indicate a column density of 1.5×10^{16} H_2O molecules cm^{-2} which corresponds to a gaseous water emission rate of 170-250 kg s^{-1} making it the most abundant component of the plume. The final results from the INMS measurements are presented in Table 2.2 [65]. In the gas phase, H_2, NH_3, and CO_2 are found with volume mixing ratios of at least fractions of a per cent. Methane constitutes the most abundant organic compound at approximately 0.2%. The D/H ratio in the plume is significantly higher than in the surrounding atmosphere [65].

Table 2.2: Final volume mixing ratios of all confirmed neutral gas compounds in Enceladus' plume from Cassini INMS [65].

H_2O	CO_2	CH_4	NH_3	H_2
96-99%	0.3-0.8%	0.1-0.3%	0.4-1.3%	0.4-1.4%

2.3.2. Composition of the Solid Phase

Three Cassini instruments have analyzed the chemical makeup of the frozen part of Enceladus' plumes: the Cosmic Dust Analyser (CDA), the Cassini Plasma Spectrometer (CAPS), and the Visible and Infrared Mapping Spectrometer (VIMS). The first two operate in situ, with CDA detecting ice grains ranging from approximately 0.2 to 2 µm in radius [63], CAPS observing even smaller grain sizes down to 0.003 µm [65], and VIMS studying plume ice grains with remote sensing using infrared wavelengths between 1 and 5 µm [9].

In-situ icy grain sampling inside E-ring

Goldstein et al. [26] used in-situ measurements to find that a minor fraction (5-10% by mass) of the solid plume particles larger than ≈ 0.1 µm is ejected at a velocity sufficient to escape Enceladus' gravitational pull, contributing to the formation of the E ring. By analyzing ice grain measurements in the E ring using CDA, it is observed that 95% of all E ring spectra fall into three distinct major families as shown in Figure 2.29. These families are likewise found in the plumes but in varying proportions.

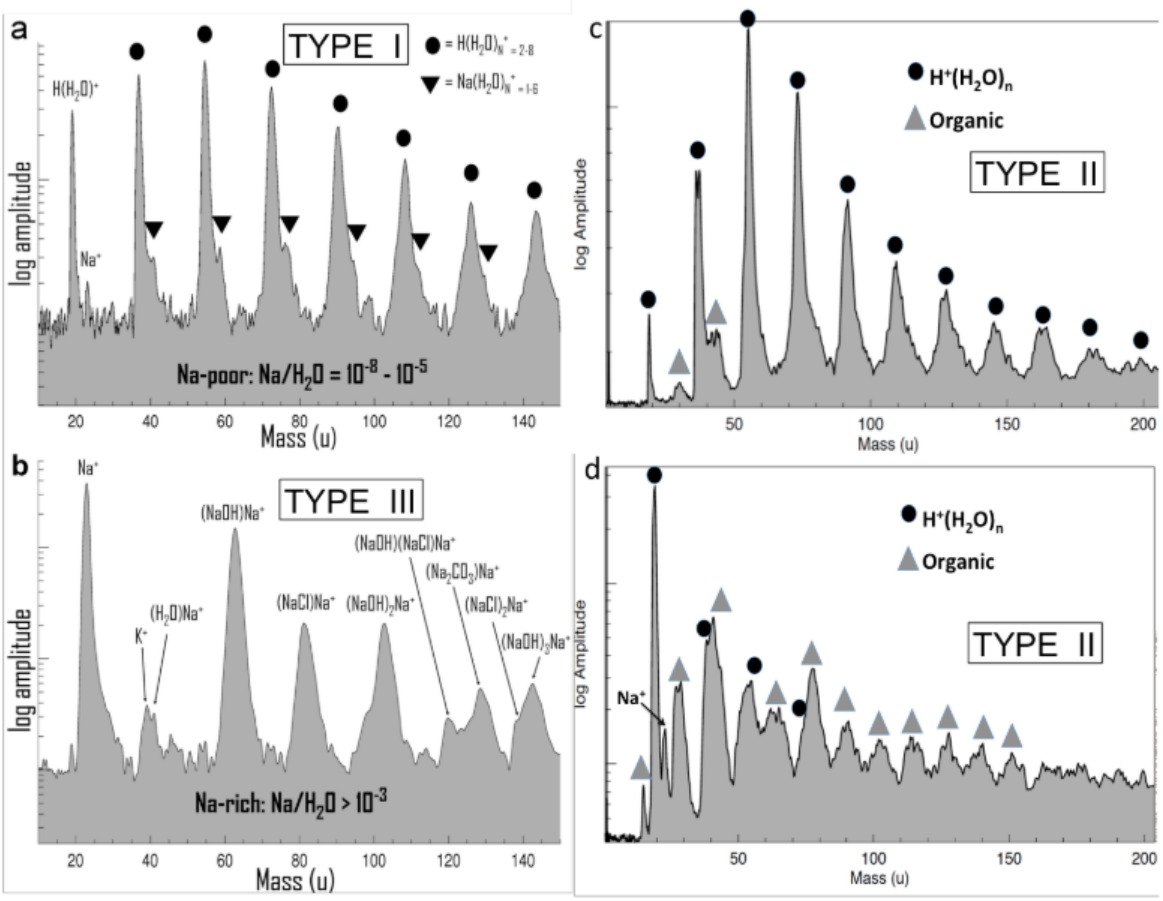

Figure 2.29: CDA mass spectra from Postberg et al. [64] showing different compositional types present in the E-ring [65].

- *Type I particles*: Particles classified as type I comprise around 65% of all E-ring spectra, and this percentage rises as particle size decreases. It appears that almost all of the material in these grains is water ice. There are very low concentrations of alkali salts in the ice grains with Na/H_2O species ratios on the order of 10^{-7}.
- *Type II particles*: Are on average larger than Type I particles. Type II spectra represent the second most abundant E-ring family ($\approx 25\%$, increasing with increasing grain size). In most cases, Type II particles show similar features as Type I with additional distinct features showing organics. Grains can differ significantly in terms of their organic matter fraction and composition. Like Type I, the majority of Type II particles are low in salt.

- *Type III particles*: comprises 10% of the E-ring spectrum and possesses entirely distinct characteristics. There are no prominent water cluster peaks, in contrast to Type I and Type II. Salt richness is indicated by defining characteristics that show Na/H_2O species ratios much higher than 10^{-3}. In addition, Type III particles are significantly bigger than Type I particles.

The CDA instrument in the E ring has detected another category of dust particles known as 'stream particles.' These are nanometer-sized dust particles with high speeds (often exceeding 100 km/s), ranging from 2 to 9 nm. Numerical simulations tracking their trajectories suggest that most of Saturn's stream particles originated from the E ring prior to being expelled into streams that are not gravitationally bound to the Saturnian system [33]. Furthermore, analysis of their composition and dynamic modelling suggests that these particles are likely fragments released from significantly larger ice grains within the E ring due to erosion by magnetospheric plasma [32]. The stream particles offer distinctive insights into the composition of the plume because, unlike grains in the E ring, a significant number of the larger Saturnian stream particles primarily consist of silicon and are deficient in water-ice [65]. A full overview of the particle characteristics on the inner E-ring near Enceladus is given in Table 2.3 and Table 2.4.

Table 2.3: Abundances of main ice grain types as identified by CDA in the E ring and their non-water constituents [65].

	Type I	Type II	Type III	Stream Particle Nanograins
Number fraction	60-70%	20-30%	$\approx 10\%$	-
Main non-water constituent (MNWC)	Na, K	Organic	Na and K salts	SiO_2
Typical MNWC concentration in individual grains	<0.0001%	0.000001-10%	0.5-2%	High

Table 2.4: Integrated abundances of constituents found by CDA in the inner E ring [65].

	Water Ice	Organic Material	Na and K Salts	SiO_2
Concentration in E ring solids	99.0-99.9%	0.01-0.3%	0.1-0.4%	0.015-0.35% (upper limit)
Concentration in plume solids	Decreasing	Increasing	Increasing	Similar(?)

Postberg et al. [64], constructed a model that could explain the presence of the three particle types inside the E-ring with their origin at the subsurface ocean of Enceladus. The research proposed that the grains rich in Na are directly frozen droplets from the liquid sub-surface ocean, with a size of submicrometers. The process can be seen in Figure 2.30 (a). Blue, aerosol-like droplets are produced when the salty liquid disperses above it. Dispersion can occur due to the rising of plume gases ($CO_2, N_2, CO, and CH_4$) or boiling of the sub-surface ocean. The droplets maintain the composition of the ocean. Submicrometer- to micrometer-sized droplets of this kind would nucleate more water from the supersaturated gas that pulls them upward. Thus, the lowest possible salt concentration for an Enceladus ocean's surface might be found in Na-rich (type III) grains.

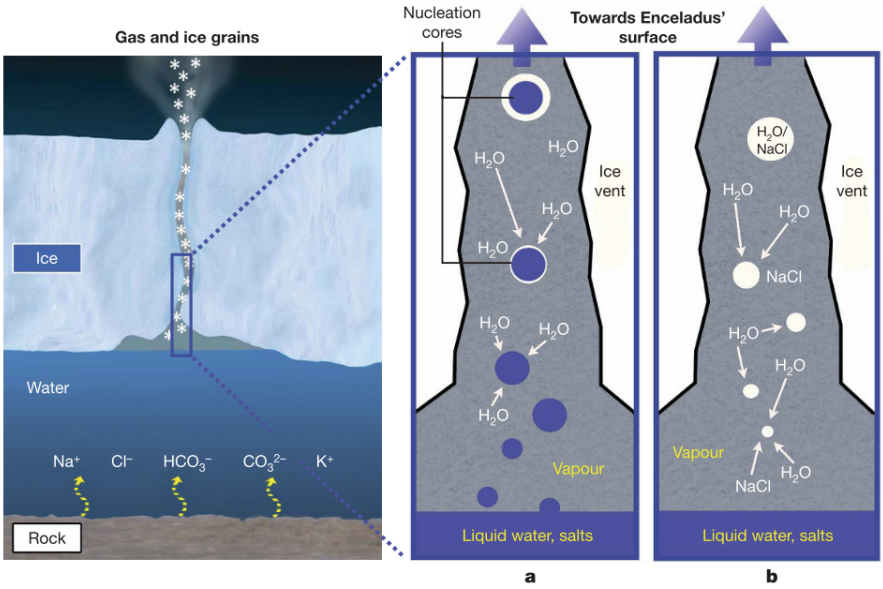

Figure 2.30: Diagram showing how ice particles with drastically differing Na contents are formed through liquid dispersion and condensation from vapour [64].

Within the ice channels, direct nucleation of the ascending vapour is another efficient method for grain formation. Figure 2.30 (b) depicts the typical process by which ice grains are formed: water vapour rising from a liquid reservoir, then growing and moving through a vent. The initial Na/H_2O ratio of the particles is the same as that of the gas. The Na-rich grains may interact directly or indirectly (for example, through crackwalls) to add traces of Na salt, further enriching them. Consequently, the maximum salt content of the plume gas can be regarded as the salt content of the Na-poor grains. Thus, the low concentration of NaCl molecules in the water vapour above the liquid may be immediately reflected in the low Na content of type I and II grains, which make up more than 90% of the spectra that were recorded Figure 2.30 (b) [64].

In-situ icy grain sampling inside the plume

After performing measurements inside the plume, the CDA observed strong differences in particle type abundances between those of the plume and the E ring shown in Figure 2.31. The most plausible explanation for these differences is given by the model shown in Figure 2.32 from the E5 fly-by. In the left panel, background colours indicate the modelled proportion of salt-rich grains (Type III), with pure water ice (Type I) and organic-bearing grains (Type II) collectively categorised as salt-poor in this model. Contours of constant mean particle radius derived from the model are shown in red. The projection aligns with the E5 spacecraft trajectory (solid black line, shown at 10-second intervals). From Figure 2.31, the expectation is to observe both the largest particles and the highest fraction of salt-rich grains a few seconds after the closest approach to Enceladus. It is important to highlight that the model exclusively considers particles with radii exceeding the estimated instrument's detection threshold ($r \geq 0.2$ µm). The concurrent rise in Type III and decline in Type I proportions in the fringe section of the plume can be attributed to the phenomenon that salt-rich grains are expelled at slower velocities compared to salt-poor grains. The slow Type III grains are dominant at low altitudes. On the contrary, the faster Type I grains show enrichment at higher altitudes and in the E ring but are depleted close to Enceladus. In contrast, the heightened ratio of organic-containing Type II ice grains in the central region of the plume appears to be independent of altitude and, consequently, ejection speed [65]. Other fly-bys, such as E17 and E18, show similar differences between the Type I and Type II spectra but are less strong. The discrepancies could be caused by the different fly-by profiles. Fly-bys E17 and E18 flew almost parallel to the surface while E5 grazed the plume more vertically (see Figure 2.32).

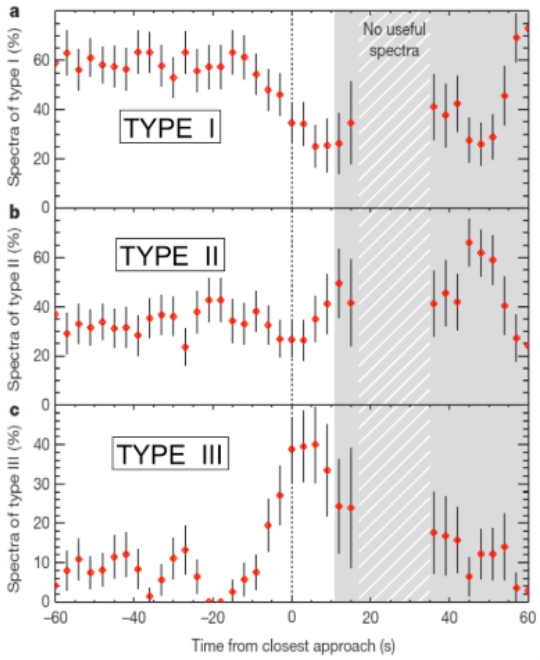

Figure 2.31: Relative frequencies of the compositional grain types (I, II, and III) during the E5 fly-by measured by the CDA [63].

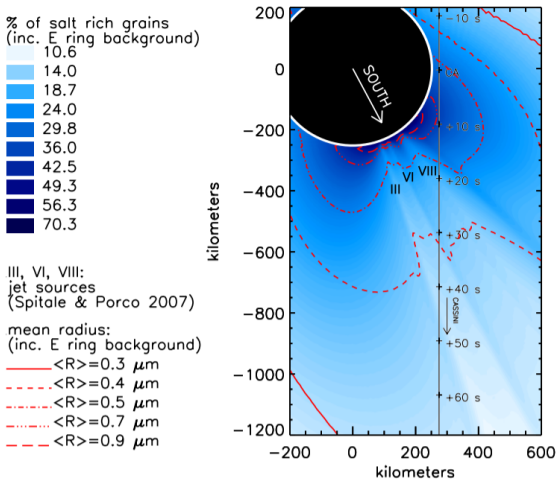

Figure 2.32: Visual representation of the model plume, based on data from the E5 flyby, illustrating the E ring background. [65] [63].

Remote sensing of icy grains

Details regarding the composition of plume ice particles can also be inferred from remote-sensing spectral data. However, challenges arise due to the plume's low optical depth (light passes through easily) and the strong forward scattering of plume particles. The former leads to spectra with low signal-to-noise ratios, while the latter results in observations with high signals typically lacking strong absorption signals. Near-infrared plume spectra primarily exhibit a dip at three microns, attributed to the robust fundamental water-ice absorption band, with no other component securely identified so far. Figure 2.33 shows how the VIMS spectral data offer crucial constraints on the physical structure of the ice grains. For instance, the position of the band minimum depends on whether the ice is in an amorphous or crystalline state, and the observed spectra suggest that the plume particles are predominantly composed of crystalline water ice [16]. This crystalline state implies formation at temperatures above 130 K, consistent with other indications of warm plume sources. Further investigations into the spectral and photometric properties of the plume particles may unveil whether they are compact grains or loose aggregates of smaller particles [65].

VIMS's highest-resolution near-infrared spectral data can distinguish material from three of the fissures, enabling the detection of spatial variations in plume particle properties. Ice grains emanating from Baghdad, Cairo, and Damascus all exhibit a robust three-micron water-ice absorption band with a band minimum position consistent with primarily crystalline water ice. However, the detailed shape of this band and the spectral slope at shorter wavelengths vary between fissures. This observation likely reflects differences in particle size distributions erupted from various fractures, but it could also imply variations in the structure and compositions of grains from different sources [65].

It is known that the plumes can vary with time. The plume brightness from emitted ice grains varies by a factor of four between the apocenter (maximum) and pericenter (minimum). This variation could be attributed to alterations in total mass flux, significant shifts in the grain size distribution, or a combination of both factors [65]. Apart from the compositional stratification observed in the macroscopic ice grains within the plume, Cassini measurements have not provided well-defined constraints on the spatial and temporal variations in the plume's composition [35]. Nevertheless, considering the intricate dynamical fine structure and the substantial diurnal orbital changes in plume brightness, there is a strong likelihood that yet-to-be-discovered compositional variations align with fluctuations in activity [65].

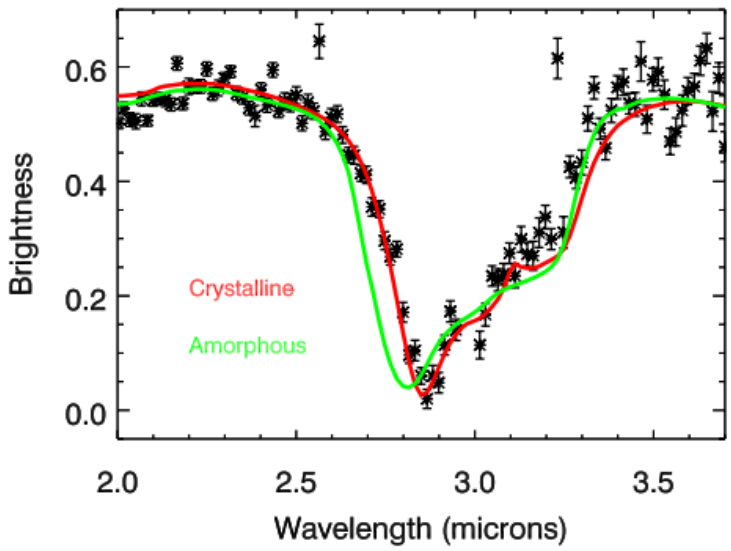

Figure 2.33: Spectra of ice in Enceladus' plume. Mie theory-based model spectra for crystalline and amorphous ice compared with VIMS plume spectra [16].

2.3.3. Vent Locations and Distributed Sources

While various instruments have observed the material emerging from the South pole, the most comprehensive details about the source locations are provided by ISS observations. These observations include highly detailed views of the particle-rich jets originating from the tiger stripe fissures [26]. Recent studies have employed triangulation of distinct jets to create maps depicting jetting activity at different times. In a study by Spitale et al. [74], it was demonstrated that a significant portion of the eruptive activity can be elucidated by broad, curtain-like eruptions. Optical illusions in these curtain eruptions, resulting from the combination of viewing direction and local fracture geometry, give rise to image features that were likely previously misinterpreted as discrete jets. These features, known as 'phantom' jets, stem from variations in curtain optical thickness caused by the meandering of source fractures in relation to the line of sight.

A clear example is depicted in Figure 2.34 (b); the top raw Cassini image seems to depict two strong jets, while the bottom image reveals that the same picture can be created through a curtain-like model. Therefore, the two jets in the image are an optical illusion and thus are called phantom jets. As a result of this phenomenon, it is frequently impossible to determine relative eruptive intensities along a fracture since phantom jets and local fluctuations in eruptive intensity sometimes appear to be indistinguishable. The phantom jet phenomena suggest that there are fewer localized eruption sources along tiger stripes than previously believed. Although prominent separate jets are still needed to explain the activity seen in some photos (particularly brilliant areas at high altitudes), the curtain-like sprays, on the other hand, appear to have heights closer to 10 km and possibly consist of material released at lower velocity [26].

Figure 2.35 illustrates key features and underlying physics in different eruption regions. Region A, well below the surface, involves liquid, yielding droplets and vapour that ascend to the surface. Moving to region B, close to the surface, the mixture accelerates through a constriction or gas-dynamic throat, expanding and accelerating further below the surface in region C. In region D, the flow interacts with the icy conduit through heat, mass, and momentum exchange. Upon reaching above the surface, the gas/icy grain flow encounters expansion waves in region E, converting thermal energy to directed energy during upward acceleration and cooling. As the geyser expands further, gas and grain densities decrease in region F, expanding into vacuum without interference from a background atmosphere. In region G, above the vent, particulate motion decouples from vapour motion, allowing some particulates to fall back to the surface. In region H, located even higher above the vent, intermolecular collisions become less frequent, and particles follow ballistic trajectories under gravitational and, when ionized, electromagnetic forces. Cassini observations primarily occurred near and above region G, where par-

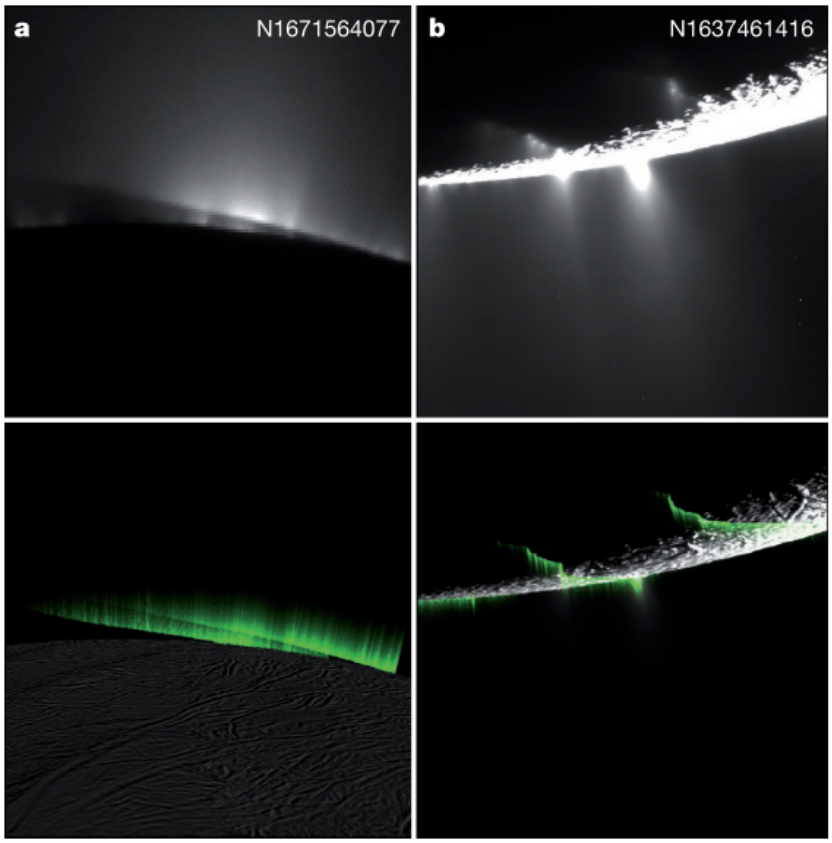

Figure 2.34: a, Top, Cassini image N1671564077 showing jet curtains from Baghdad and Damascus Sulci. b, Top, Cassini image N1637461416. Bottom, simulated uniform curtains overlain on the images [74].

ticles and vapour had already separated [26].

2.3.4. Plume Particle Distributions

Based on the velocity at which the grains were expelled, three regimes of erupted grains could be identified. The group that moves slowly emerges from the vents and descends from the plume near the tiger stripes. These particles are often large. A different, swifter group disperses itself widely across the surface. A third group completely departs the satellite at velocities higher than Enceladus' escape speed. The correlations between the various populations' sizes and speeds provide insight into the physics of their creation [26].

Nucleation and dispersion above the vent

When a high Mach number geyser exits the surface (area E and beyond, Figure 2.35), its highly supersaturated vapour condenses on the water droplets and ice grains already present, increasing their size by heterogeneous nucleation. According to Yeoh et al. [83], if meter-scale vent openings and sonic exit conditions are assumed (the throat being at the surface in their discussion), then condensation growth via heterogeneous nucleation above the vents is proportional to vent size. If the grains start at a negligible size at the vents, then fairly large vents several tens to hundreds of meters in size are required to produce the micron-sized grains detected by CDA (radii 1.6 µm). Particulates can only grow up to $\approx$1 µm until the collision rate decreases, preventing grain growth within a few vent diameters of the exit [26]. Condensation of supersaturated gas can also result in the formation of new grains ranging in size from a few molecules to several hundred nanometers. These nanograins, some of which accumulated a charge, were measured using CAPS. Other mechanisms, such as liquid dispersion [64], should also be considered [26]. The study also found that nanometer-sized grains disengage from the gas at altitudes of 10-100 vent diameters and spread considerably, while micron-sized grains decouple at <10 vent diameters and remain in collimated beams. Even with considerable velocity differences at

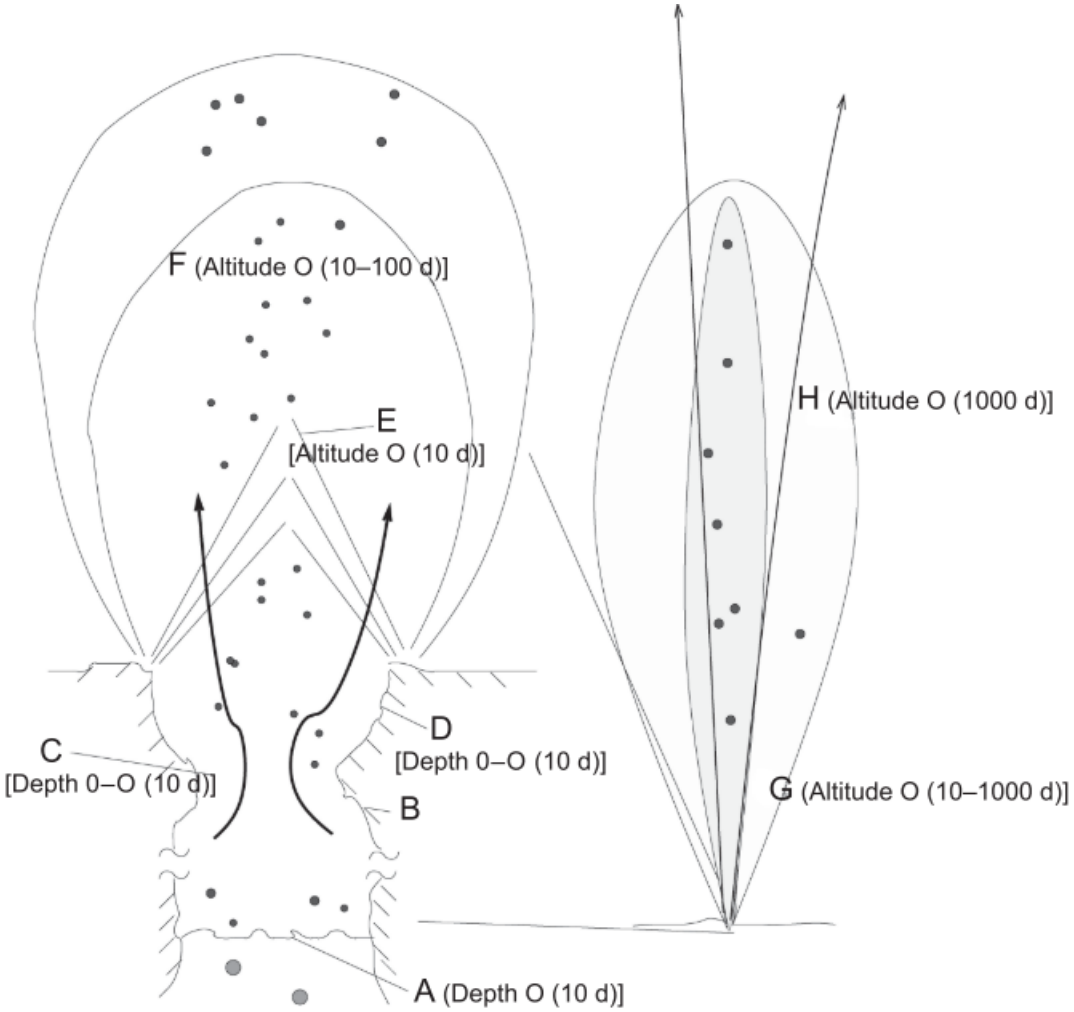

Figure 2.35: Illustration of a geyser's characteristics and areas of dominant physics (A–H which are explained in the text). An order of magnitude multiple of vent diameters (d) is used to express the region's depth or altitude [26].

the vent, the micron-sized grains spread maximally 12° compared to the boresight of the vent. As a result, the inferred spreading angles of 30° by Postberg et al. [63] cannot be generated by the velocity differential at the vent. According to VIMS [25], vent diameters typically measure 9 m and decouple within 1 km of the surface.

Total Particulate Mass in Plumes from ISS

Ingersoll and Ewald [34] exploited the Saturn system's eclipse mosaic (PIA08329) shown in Figure 2.36, which was captured on September 15, 2006, while Cassini was in Saturn's shadow. It includes many colour views of the E ring and the Enceladus plume at phase angles between 173° and 179°. In this forward-scattering study, a diffraction peak was sampled for particle radii in the range of 1-5 µm. The overall brightness and phase angle dependence proved to be sensitive measures of the total mass of solid material in the plume. The brightness of the plume, which is dependent on particle size, is proportional to the scattering cross-section of the particles times their phase function since it is optically thin. Using a range of particle sizes and shapes, Ingersoll and Ewald [34] fitted the data and discovered that the equivalent-volume sphere's median radius is 3.1 µm, with a ±0.5 µm margin of error. A narrow power law distribution was found to give the best fit. Particle mass in the plume as a whole was determined to be 1.45 ± 0.5 $\times 10^5$ kg. Particle size and shape distribution variations with altitude were not taken into account. They discovered that the brightness of the E ring changes with orbital location due to an unidentified inherent variability as well as viewing geometry variations, such as phase angle

variations. In the plume, the mass per unit time exiting the vents is 51 ± 18 kg/s.

Figure 2.36: This image (PIA08329) from NASA/JPL shows a mosaic made from photos captured on September 15, 2006, as Cassini was under Saturn's shadow. The pictures were captured at an average distance of 2150,000 km using Cassini's wide-angle camera. The lower left section of the E ring displays the scattering angle expressed in degrees [34].

Particle distribution from VIMS

For particles with a radius of 1 to 4 μm, the near-infrared spectra of the plume acquired by VIMS offer quite direct observations of the size distribution. The VIMS plume measurements are made at high phase angles, therefore the signal is predominantly caused by light diffracting around individual particles [26]. In this limit, a particle scatters light most efficiently when $x \sin\theta \approx 2$, which corresponds to the first diffraction peak of the first-order Bessel function as seen in Equation 2.8. Here $x = 2\pi r/\lambda$ with particle radius r. θ is the scattering angle and can be converted to phase angle α with $\theta = \pi - \alpha$. Hedman et al. [30], used observations at a phase angle of $160°$ which gave an almost one-one relation between particle size and wavelength $r/\lambda \approx 1$. Therefore, VIMS IR spectra are primarily sensitive to particle size distributions in the 1-5 μm range, assuming wavelength directly correlates with particle size. These spectra demonstrated that the plume's particle component is predominantly composed of fine-grained water ice. The spectral data is used to produce profiles of particle densities vs height, which are then transformed into measurements of the velocity distribution of particles propelled from the surface between 80 and 160 m/s (between one-third and two-thirds of the escape speed). Particles with 1 μm radii have similar launch speeds (80-160 m/s), but those with 2 and 3 μm radii exhibit steeper velocity dispersion. Therefore, larger particles are launched less high and are deposited closer to the vents [30].

Plume stratification

CDA in situ examinations of grains near Enceladus and in the E ring offer valuable insights into particle size, velocity, and source. Postberg et al. [63] discovered that near Enceladus, sodium-rich grains are larger and slower, and account for 99% of the particulate matter ejected from surface vents Figure 2.37. The proportion of salt-rich grains in the plume reduces as altitude rises, and larger, slower salt-rich grains return to the surface. The majority of the grains that escape from Enceladus are salt-poor, whereas the majority of the grains that emerge from the vents are larger salt-rich grains [65]. Figure 2.38 depicts the expected correlation between particle size and altitude. The grey band, which at 1 m height spans particle sizes of 2×10^{-4} to 10^{-3} m, indicates acceleration is limited by particle collisions with walls, while in the other band acceleration is limited by gas drag. The upper and lower limits for each band are for gas temperatures between 190 K and 273 K [26]. While the model is solely bound by surface observations, it is consistent with high-altitude CDA, VIMS, and E-ring measurements, implying that surface and high-altitude particle sizes are derived from the same eruptions but that larger particles move slower than smaller particles. It is important to note that the topology of particles affects particle-size distributions in ISS (visible) images. For example, smooth spheres interact with light differently than rough-surfaced aggregates of the same mass. The model has two implications, as do the surface grain

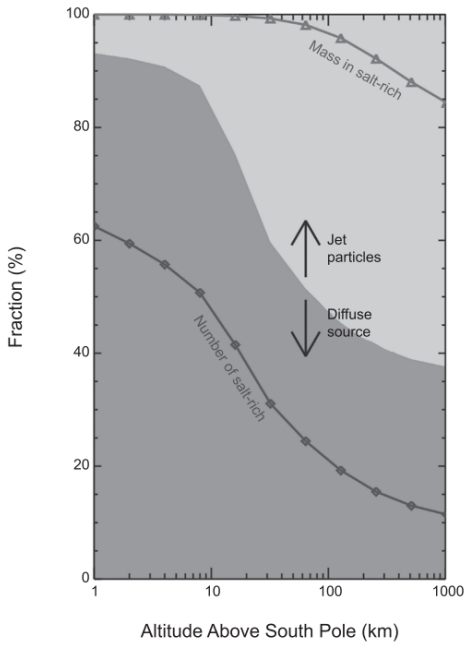

Figure 2.37: Fraction of salt-rich grains in Enceladus' plumes versus altitude [65]

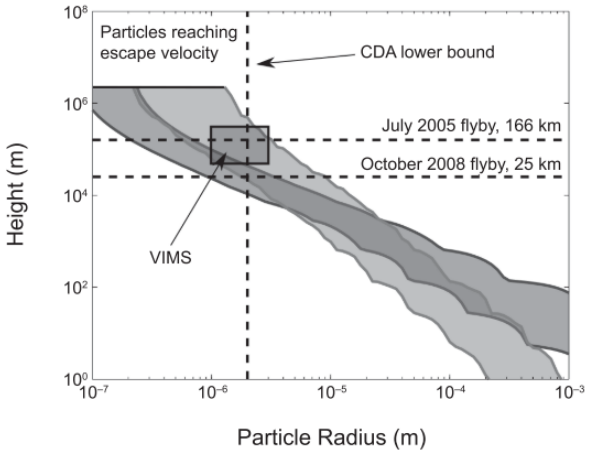

Figure 2.38: Peak particle elevation in relation to particle dimensions for two sets of models, both limited by VIMS deductions of particle dimensions close to the tiger stripes [14].

size findings. First, particles larger than tens of micrometres erupt, which exceeds what would simply condense from vapour [83]. Large particles can be frozen droplets from the ocean or mechanically created particles from the conduit walls. Larger particles may erupt, but they will settle near the surface vents [26].

2.4. Cassini Specifications

After exploring the physical origin of optical phenomena and the particles responsible for them, the next parameter that requires investigation is the observer. First, an overview of Cassini's mission profile will be given in subsection 2.4.1. Next, an overview of the instrument characteristics of the ISS and VIMS will be shown in subsection 2.4.2 and subsection 2.4.3, respectively.

2.4.1. Mission Profile

Enceladus has intrigued scientists since the early 1980s due to its unique characteristics. During the Voyager encounters in 1980 and 1981, Enceladus revealed its remarkably high albedo, unmatched by any other solid body in the solar system, along with its varied terrain marked by craters and fractures. Coincidentally, ground-based observations around the same period identified a concentration of Saturn's tenuous E-ring along Enceladus's orbit. This concentration hinted at the presence of a continuous source of supply at Enceladus. Researchers suggested that the short lifetimes of the micron-sized E-ring particles could originate from ongoing geyser-like activity on the moon. Furthermore, the detection of a neutral OH cloud in the 1990s by the Hubble Space Telescope further emphasized the need for a significant source in close proximity to Enceladus. Thus, from the beginning of the Cassini mission, Enceladus was a top priority target. The prime mission tour featured ten flybys of Saturn's mid-sized satellites, including three of Enceladus [17]. After entering the Saturn system in 2004, NASA's Cassini spacecraft studied Saturn, its rings, and its several satellites over the following 13 years. Cassini conducted three close flybys of Saturn's small moon Enceladus in February, March, and July of 2005. A fourth near, non-targeted flyby of Enceladus was also part of the tour in February 2005. These flybys provided insights into the geologically diverse surface of Enceladus, which includes cratered terrain, heavily tectonized regions, thermal anomalies, and cryovolcanic plumes emanating from south polar fractures [60]. These findings made Enceladus a high priority for Cassini's follow-up missions, which led to 23 planned flybys of the satellite during the mission's 13-year duration—nearly five times more than any other midsized satellite. The details of these close fly-bys are listed in Table 2.5, and Fig-

ure 2.39 shows the orbit geometries with respect to Enceladus. Additional information was received from about thirty farther-off non-targeted flybys [6].

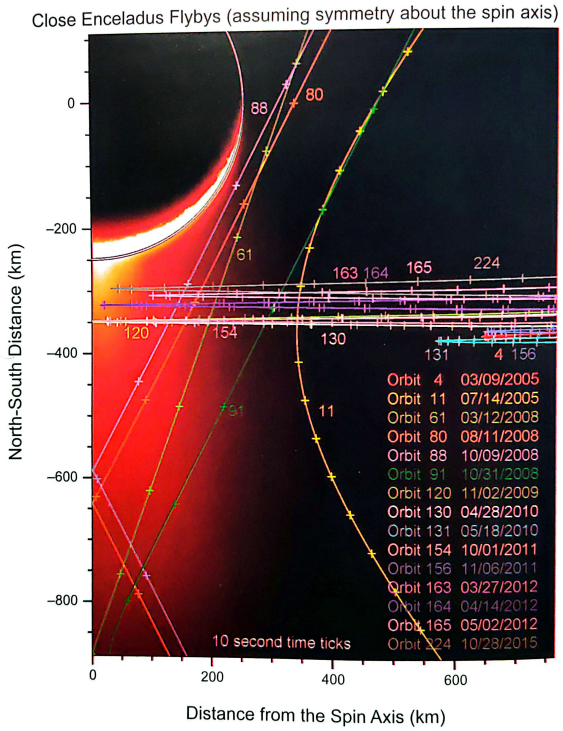

Figure 2.39: Schematic showing the geometries of the targeted Cassini flybys relative to Enceladus. The different orbits and dates are colour-coded. [17]

2.4.2. Cassini Imaging Science Subsystem (ISS)

The Cassini ISS consists of two fixed focal length telescopes known as 'cameras'. These are called the Narrow Angle Camera (NAC) and Wide Angle Camera (WAC). They are located on the Cassini Orbiter's Remote Sensing Palette (RSP), between the Visible and Infrared Mapping Spectrometer (VIMS) and the Composite Infrared Spectrometer (CIRS) sensors, and above the Ultraviolet Imaging Spectrometer (UVIS). The apertures and radiators of both telescopes are parallel [60]. The FOV of the NAC, WAC, and other remote sensing devices on the palette are depicted in Figure 2.40. The NAC is an f/10.5 reflecting telescope with a spectral range of 200 to 1100 nm, an image scale of $\sim$ 6 µrad/pixel, and a 0.35° × 0.35° field of view (FOV). There are 24 spectral filters in its filter wheel subassembly, with 12 filters on each of the two wheels. The WAC's optical train is an f/3.5 refractor with a $\sim$ 60 µrad/pixel image scale and a 3.5° x 3.5° field of view. The refractor design limits the WAC's lower spectral range, which is 380-1100 nm. The WAC filter subassembly contains nine filters in each of the two filter wheels, totalling 18 filters. In both cameras, images are captured through two filters, one on each wheel, allowing in-line combinations of filters for greater flexibility: polarizers in line with other spectral filters, new bandpasses generated by overlapping two spectral filters, and so on [60]. A detailed overview of the ISS system characteristics can be found in Table A.1.

A complete overview of the ISS filters is given in Table A.3 along with a short scientific reasoning for the selection of the specific filters. The narrow-band filters will not be discussed further as these are not used for plume observations looking at the image database. Filters which were extensively used in plume observations where the clear filters (CL1 and CL2). These allow for transmission across the entire spectral range of the ISS and thus have the highest sensitivity to the optically thin plumes [36]. Medium- and broad-band filters were also included, enabling colour imaging of a variety of targets (including Enceladus plumes) and imaging scenarios. An overview of the medium- and broad-band filters on the NAC and WAC is given in Figure 2.41. The NAC filters consist of: UV1, UV2, UV3 (purple:

Table 2.5: Cassini's close Enceladus flybys [17]

Orbit, encounter name	Date Time (UT)	Speed (km/s)	Closest approach		Geometry 1h before encounter		Geometry 1h after encounter	
			Altitude (km)	Sub-spacecraft point	Sub-spacecraft point	Solar phase	Sub-spacecraft point	Solar phase
3, E0	2005/02/17 03:30	6.7	1260	239W, 51N	318W, 1N	27	163 W, 3 N	159
4, E1	2005/03/09 09:08	6.6	497	304W, 30S	202W, 1S	45	41 W, 0 S	130
11, E2	2005/07/14 19:55	8.2	166	327W, 22S	197W, 48S	46	36 W, 47 N	132
61, E3	2008/03/12 19:06	14.4	47	135W, 21S	125W, 70N	114	327 W, 70 S	65
80, E4	2008/08/11 21:06	17.7	50	97W, 28S	87W, 62N	107	289 W, 63 S	72
88, E5	2008/10/09 19:06	17.7	25	97W, 31S	86W, 62N	107	289 W, 63 S	72
91, E6	2008/10/31 17:14	17.7	197	97W, 26S	86W, 62N	107	288 W, 63 S	72
120, E7	2009/11/02 07:41	7.7	99	159W, 88S	329W, 1S	174	170 W, 0 N	5
121, E8	2009/11/21 02:09	7.7	1602	112W, 82S	189W, 3S	145	31 W, 3 S	33
130, E9	2010/04/28 00:10	6.5	99	147W, 89S	317W, 1S	172	159 W, 0 S	7
131, E10	2010/05/18 06:04	6.5	434	304W, 34S	201W, 0S	154	42 W, 1 S	27
136, E11	2010/08/13 22:31	6.9	2550	29W, 78S	198W, 17S	153	39 W, 4 N	23
141, E12	2010/11/30 11:53	6.3	47	53W, 62S	315W, 0S	166	156 W, 0 S	14
142, E13	2010/12/21 01:08	6.3	47	232W, 62S	314W, 0S	166	156 W, 0 S	15
154, E14	2011/10/01 13:52	7.4	99	204W, 89S	192W, 0S	151	34 W, 1 S	28
155, E15	2011/10/19 09:23	7.5	1229	114W, 14S	189W, 0S	154	36 W, 1 S	31
156, E16	2011/11/06 04:59	7.4	495	295W, 30S	193W, 0S	151	34 W, 0 S	29
163, E17	2012/03/27 18:29	7.2	82	191W, 76S	191W, 0N	160	32 W, 1 S	20
164, E18	2012/04/14 14:00	6.5	175	206W, 49S	191W, 0N	160	32 W, 1 S	20
165, E19	2012/05/02 09:31	7.6	73	291W, 49S	191W, 0N	159	32 W, 1 S	21
223, E20	2015/10/14 10:41	8.4	1838	106W, 78N	185W, 4N	23	24 W, 4 N	148
224, E21	2015/10/28 15:22	8.5	48	66W, 84S	336W, 0N	41	177 W, 1 S	139
228, E22	2015/12/19 17:48	9.5	4999	353W, 88S	342W, 6S	46	183 W, 10 S	144

solid, dotted, and dashed); BL1, BL2 (blue: solid and dashed); GRN (green); RED, (red); IR1, IR2, IR3, and IR4 (orange: solid, dot-dash, dashed, and dotted). For the WAC: VIO (purple), BL1 (blue), GRN (green), RED (red), IR1, IR2, IR3, IR4 and IR5 (orange: solid, dashed, dotted, and the latter two not shown). The CL1/CL2 filter combination is given by the solid black line in both plots.

Additionally, a series of polarised filters equipped on both cameras enables polarimetry observations aimed at examining the scattering characteristics of atmospheres, rings, and satellite surfaces. Their transmission functions are shown in Figure 2.42. The NAC features a primary filter wheel housing three polarisers – P0, P60, and P120 – designed for visible wavelengths. These filters are aligned with their principal transmission axes positioned at a 60-degree angle to each other. In contrast, the WAC, equipped with fewer filter wheel slots than the NAC, accommodates only two polarised filters – IRP0 and IRP90 – operating in the infrared spectrum and positioned perpendicular to each other. Additionally, the NAC incorporates a single polarised filter sensitive to infrared wavelengths, IRP0 [36]. The three visible polarisers and one IR polariser in the NAC can be used with a suite of spectral filters on the opposite wheel that range from UV to near-IR. The WAC allows for a combination of two broadband filters, IR2 and IR4. The polarisers on both the NAC and WAC were used to reduce scattering by atmosphere haze, particularly with the IR polarisers [61].

Another important parameter to take into account is the effect of stray light. Figure 2.43, depicts the effects of stray light in the NAC and WAC. While the NAC image displays internal reflections, including the pattern from the secondary mirror support from a bright object just outside of the frame, the high phase angle WAC image contains multiple diffraction rings from dust particles on the optics, illuminated by off-axis sunlight [36]. Stray light in the WAC is approximately three orders of magnitude greater than in the NAC due to the WAC's refractive optical design, and it is slightly worse in the infrared than in visible wavelengths. Solar stray light is especially problematic, reaching an I/F of roughly 0.1 when the WAC is pointed 20 degrees from the sun; the detector becomes saturated in test observations when pointed within 15 degrees. In practice, the WAC is unsuitable for imaging most dim or hazy targets at

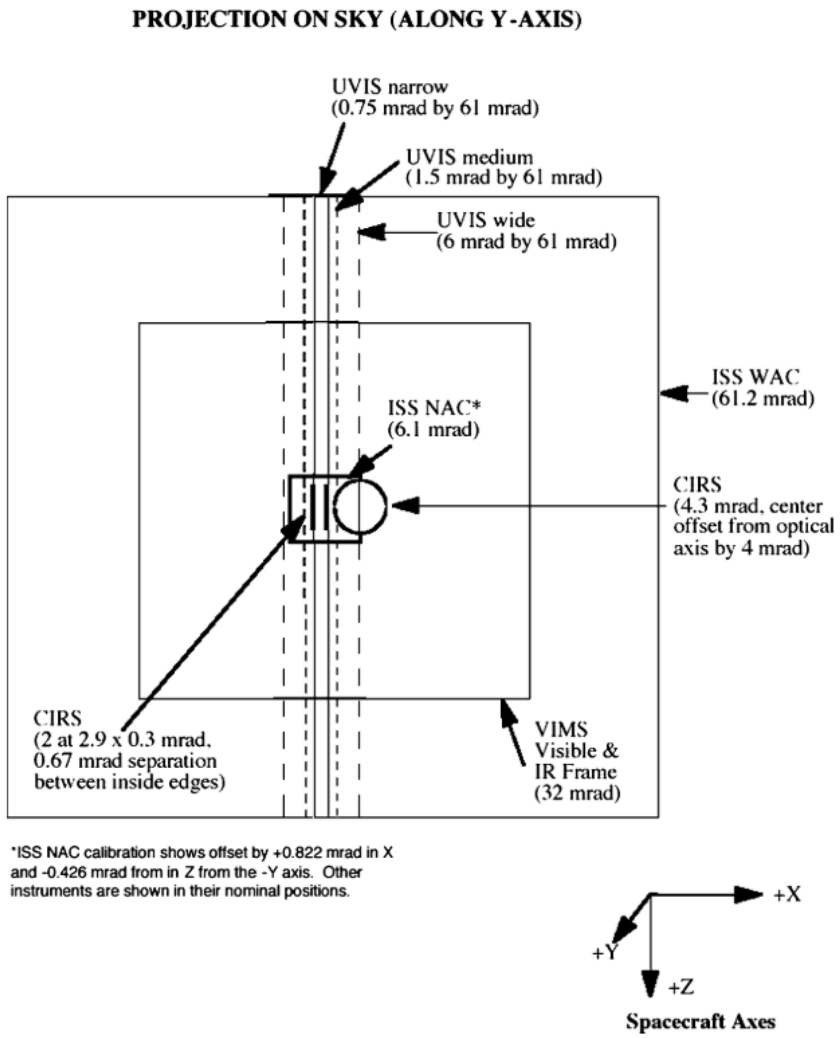

Figure 2.40: An illustration showing the fields of view of the ISS NAC and WAC cameras, as well as the UVIS, CIRS, and VIMS [61].

phase angles above 150° [36].

2.4.3. Cassini Visual and Infrared Mapping Spectrometer (VIMS)

The Visual and Infrared Mapping Spectrometer (VIMS) consists of two imaging grating spectrometers that measure visible and near-infrared light from atmospheres, rings, and surfaces with wavelengths ranging from 0.35 to 5.1 microns. VIMS aimed to analyse the composition and structure of Saturn's atmospheres, rings, and surfaces using optical and infrared spectral mapping [9]. Two optical systems are used: a VIS channel with a diffraction grating and a 288×576 pixel CCD detector, producing 2D spatial-spectral images with 64 pixels at 0.35-1.1 µm, and an IR channel with a diffraction grating and a 256-element linear InSb detector, producing single-pixel spectra from 0.88 to 5.11 µm. Typically, a 1D scanning mirror in the VIS channel and a synchronized 2D scanning mirror in the IR channel are used to create 3D hyper-spectral 'cubes' of the target scene, each with 64×64 spatial pixels and 352 spectral channels. The standard pixel (IFOV) measures 0.5×0.5 mrad and divides the spectrum into 96 VIS and 256 IR channels [8]. A full overview of the VIMS characteristics is shown in Table A.2. The much lower spatial resolution of VIMS compared to the ISS is evident from Figure 2.44. This figure contains the approximately highest achievable spatial resolution images of the plumes for both VIMS and ISS. On the left, a VIMS cube is shown at a distance of around 17,000 km from the centre of Enceladus with a spatial resolution of $\sim$ 10 km/pixel. The ISS image on the right achieves $\sim$400 m/pixel resolution. Therefore, material launched from specific fractures can not be distinguished in the majority

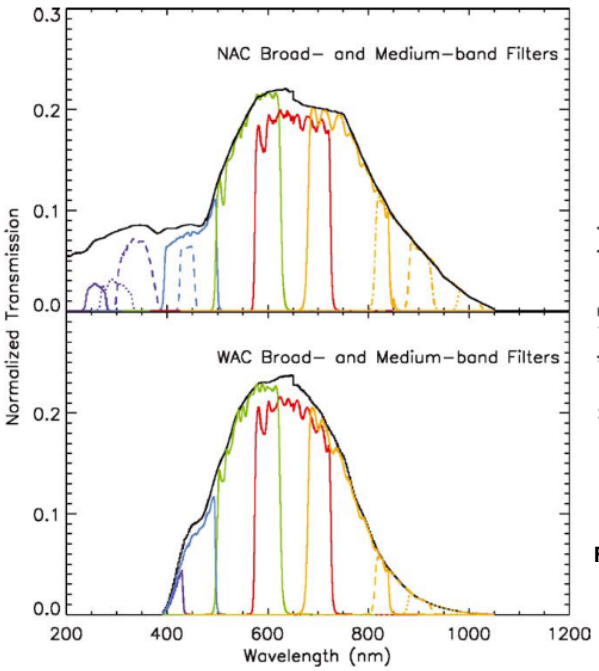

Figure 2.41: System transmission functions for NAC and WAC broad- and medium-band filters

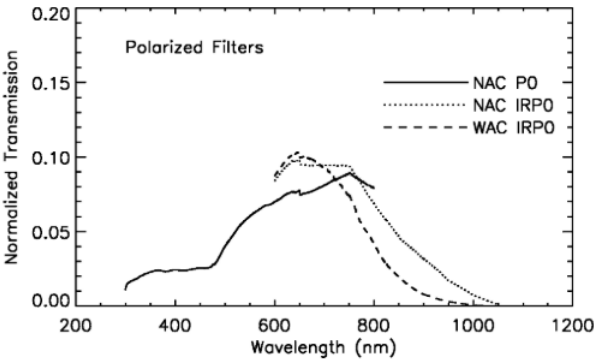

Figure 2.42: System transmission functions for the NAC visible and infrared, and the WAC infrared, polarizers.

of the VIMS images.

Past research of the plumes' spectral properties such as Hedman et al. [30], [29], and Dhingra et al. [16] have so far only employed the VIMS IR-channel. Hedman et al. [29] focused on the IR spectra as these were proven to be the most sensitive to the light scattered from micron-sized particles in the plume. UVIS, on the other hand, proved to be sensitive to the light scattered by the gas in the plume. Following the same approach, VIMS-VIS would mostly be sensitive to the forward-scattering of sub-micron particles with a similar size as the observed wavelength. Dhingra et al. [16], stated that the signal-to-noise ratio is lower in VIMS-VIS compared to VIMS-IR. Calibration can also be very difficult when aligning both the VIS and IR channels for high spatial resolution observations, resulting in a preference for analysis of a single channel. Prominent water absorption bands are also present in the IR spectrum making it easier to characterise water constituents than in the VIS. With the plumes mainly consisting of water as shown in section 2.3, it is, therefore, more scientifically interesting to look at IR than VIS. In the VIMS-IR channel, the noise level increases drastically at longer wavelengths ($>$4 µm). There are also known hot channels in the VIMS-IR (at 1.24 µm, 1.33 µm, 3.23 µm, 3.24 µm, 3.83 µm), and IR focal plane blocking filters (at 1.6–1.67 µm, 2.94–3.01 µm and 3.83–3.89 µm) [8]. The wavelength uncertainty associated with VIMS near-infrared wavelengths is less than 0.01 µm [16]. Aside from plume observations, VIMS-VIS has been used in publications regarding the characterisation of Saturn's main rings [28]. Spectral slope variations in the visible were found that could be attributed to contaminants other than water. No known issues with signal-to-noise ratios compared to VIMS-IR were reported.

2.5. Implications for Optical Phenomena Search in Enceladus' Plumes

This section aims to combine the background information on optical phenomena, Enceladus' plumes, and Cassini instrument characteristics to draw guidelines for the search for optical phenomena within the plumes. First, the plume particle properties and optical phenomena will be linked in subsection 2.5.1. Next, in subsection 2.5.2, the VIMS and ISS instruments will be compared in terms of the observability of optical phenomena.

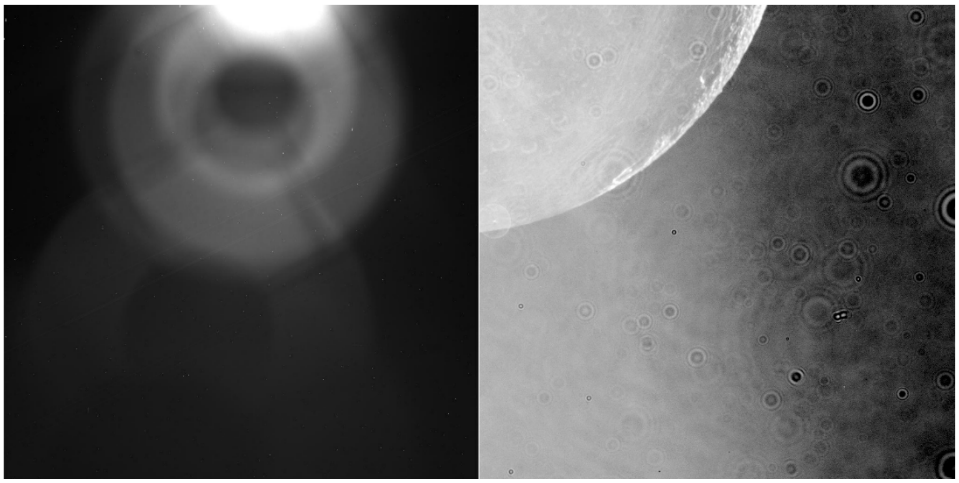

Figure 2.43: Instances of off-axis stray light in the WAC (right) and NAC (left) [36].

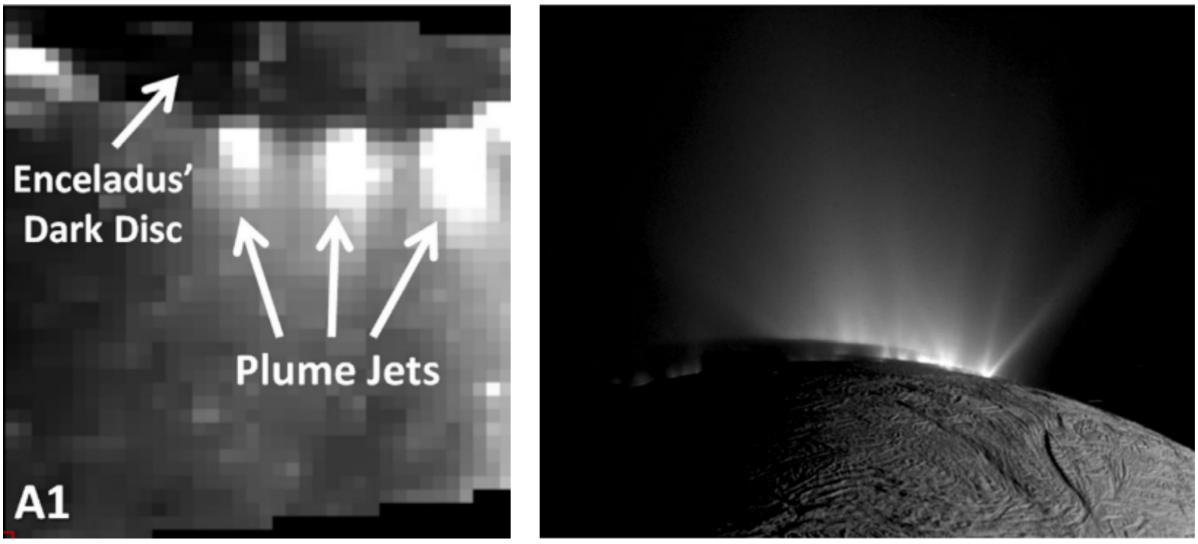

Figure 2.44: Comparison of plume observations of VIMS (left) [16] and ISS (right) [76] with approximately the highest achievable spatial resolutions.

2.5.1. Optical Phenomena and Plume Particles

After summarizing the conditions for optical phenomena as shown in Table 2.1 and the properties of plumes section 2.3, some conclusions can be drawn regarding the likelihood of optical phenomena occurring within plumes:

- **Rainbow:** From section 2.3, there appears to be no liquid plume material after ejection from Enceladus' crevices. However, it was found that liquid water is a must for creating rainbows. Therefore, it is extremely unlikely to find rainbows on Enceladus.
- **Halo:** The plumes were found to consist mainly of crystalline water ice. This is necessary for creating ice particle halos, as amorphous ice will not produce the required hexagonal structures to create dispersing ice prisms. Difficulties in observing halos in Enceladus plumes may arise from the required minimal particle size of 11 µm. This is large compared to the expected average particle sizes of around 6 µm. Nevertheless, larger particles are more likely to occur closer to the surface of Enceladus.
- **Corona:** The plume particles fall well within the particle size range to observe coronas in the visible and near-infrared. However, coronas require homogenous or very narrow particle size distributions to produce resolved rings. The plumes were found to have a stratified structure with different particle sizes and a combination of q =-3 (narrow) power law distributions. This could

potentially wash out the corona rings. Therefore, coronas are best sought in plume areas with known narrow particle size distributions.

- **Glory:** Similar to the rainbow, spherical liquid particles are required to produce a glory. In addition, there should be a minimal plume material optical thickness of 0.1 for a glory to appear. The plumes are too optically thin to meet this requirement. Therefore, it is not possible to observe glories in Enceladus' plumes.

2.5.2. Instrument Trade-offs

Knowing the properties of the possible optical phenomena and the instrument characteristics, it can be decided what the pros and cons are for observing optical phenomena through the ISS or VIMS. Table 2.6 shows relative scoring for instrument characteristics in terms of observability of optical phenomena. A characteristic is scored either $++$ (great), $+$ (good), $\pm$ (ok), $-$ (bad), or $--$ (very bad) scores for observing optical phenomena.

Table 2.6: Instrument characteristics for VIMS and ISS classification for observing optical phenomena. Aspects are assigned either $++$ (great), $+$ (good), $\pm$ (ok), $-$ (bad), or $--$ (very bad) scores.

	FOV	Spectral Resolution	Spectral Coverage	Angular Resolution	Data Availability
VIMS-VIS	$\pm$	$++$	$++$	$-$	$--$
VIMS-IR	$\pm$	$++$	$+$	$-$	$++$
ISS-NAC	$--$	$--$	$++$	$++$	$++$
ISS-WAC	$+$	$--$	$++$	$+$	$-$

A large FOV is desired for observing optical phenomena. To observe complete coronas and halos in the visible, one would need FOVs in the order of $+44^\circ$. However, this is likely impossible because of the plume's localised nature compared to the extended atmosphere on Earth (see subsection B.1.4 for more details). Partial observations of sections of the halo or corona could be possible. A resolvable section of the halo could be achieved with a FOV of 2° wide. For the corona, larger FOVs are needed to observe the colour transitions between rings, given the order of the particle radii of Enceladus plumes. The ISS-WAC scores the best with a FOV of $3.5\times3.5^\circ$ followed by VIMS with $1.8\times1.8^\circ$. The ISS-NAC scores the worst with a FOV of $0.35\times0.35^\circ$.

Optical phenomena are best observed with high spectral resolution, which enables the separation of individual wavelength contributions to arcs and rings. These contributions have been shown to exhibit spatial dependence. As a result, cycling through these components and linking them to specific positions within the images aids in identifying and characterising optical phenomena. VIMS has the best spectral resolution as a spectrometer, while the ISS can only use its filters to reveal spectral dependencies. In addition, a single VIMS cube can display the same image for each wavelength channel, leading to an identical observation geometry. However, the ISS needs to capture separate images, which leads to slightly different observation geometries between each image. This could complicate the analysis of the spectral movement of optical phenomena. Spectral coverage throughout the visible spectrum is the most desired as observations can be directly compared to the known optical phenomena on Earth. However, near-infrared coverage should also be able to reveal these phenomena as shown in subsection 2.1.7.

The highest angular resolution is essential for revealing fine-scale structures in the plumes and optical phenomena, making the ISS-NAC the most suitable instrument for this purpose. Next, data availability is critical in selecting the instruments for analysis. A malfunction in the VIMS-VIS read-out chip caused the cubes to display stripes, which must be corrected before any meaningful analysis can be conducted [39]. Furthermore, the VIMS-VIS has fewer observations of Enceladus' plumes compared to VIMS-IR, based on NASA's Planetary Data System (PDS) "Planetary Image Atlas" archive [57]. Similarly, high-phase observations are less frequent in the ISS-WAC than in the NAC, primarily due to the WAC's sensitivity to stray light, as discussed in subsection 2.4.2. As noted in Table 2.1, high-phase observations are critical for detecting coronas and halos. Consequently, there is significantly

less data from the ISS-WAC compared to the NAC.

Given the importance of data availability, it was determined that VIMS-IR and ISS-NAC observations should be prioritised in the search for optical phenomena. The VIMS-IR's broader field of view and superior spectral resolution make it ideal for initial identification. At the same time, the ISS-NAC can be used to examine these phenomena in greater detail, thanks to its higher angular resolution and spectral coverage in the visible range.

3

Research Plan

This chapter integrates the previously discussed background information into a research plan. First, the project's relevance will be discussed in section 3.1. Next, the main research questions are formulated in section 3.2. Finally, section 3.3 will present a strategy for addressing the research questions.

3.1. Introduction and Relevance of the Project

As shown in section 2.3, extensive research has been conducted to establish the relationship between the light-scattering properties of Enceladus' plumes and the particles they contain. Ingersoll and Ewald [34] derived estimates of particle column densities and total particulate mass in Enceladus plumes using forward-scattering absolute brightness measurements obtained by the ISS. This methodology has been refined and further explored in subsequent studies [35, 60, 62]. An alternative approach was employed by Hedman et al. [30], who used spectral observations from the VIMS infrared channel to generate particle densities versus height profiles. Discrepancies in the results of plume particle number densities between these instruments persist, with variations as significant as factors of approximately two to three [62].

An opportunity for a new plume characterisation method was identified. Optical atmospheric phenomena, with their unique appearances and the specific conditions needed for their occurrence, hold valuable insights into the nature of the particles responsible for their formation as shown in section 2.2. For instance, glories observed atop clouds on Earth provide crucial clues about cloud formation and evolution [49]. While such phenomena are abundant on our planet, their observation beyond Earth's atmosphere is rare. Nevertheless, some optical phenomena have been discovered in the Solar System. For instance, the Venus Express orbiter captured a glory on the upper cloud layer of Venus, shedding new light on the material and size distribution of the cloud particles [46, 58]. Similarly, the Mars Perseverance rover documented an ice particle halo generated by hexagonal prisms within crystalline water-ice clouds, offering valuable data on particle sizes and cloud formation conditions [44].

Another promising candidate for observing such optical phenomena is Enceladus' large geyser-like plumes [26]. Cassini captured over 4000 images of Enceladus' plumes during its 23 targeted flybys and more distant observations (see section 2.4) [57]. The images were created by the ISS and the VIMS, which detect light scattered by solid particles in the optically thin plumes, a process very similar to observing optical phenomena in Earth's atmosphere. Therefore, searching for colour variations in Enceladus' plumes caused by optical phenomena may provide a novel and unique opportunity to characterise the particles within the plume. This led to the creation of a research plan which aims at answering the research questions in the following section.

3.2. Research Questions

The goal of this research is to give an answer to the main research question below.

RQ: Can optical phenomena be observed in Enceladus' plumes from Cassini measurements and what can these reveal about the physical and chemical structure of the particles within?

This main research question is divided into sub-questions, which when combined will help to answer the main question. Before any optical phenomena can be discovered, it is necessary to have a thorough understanding of how the optical phenomena are expected to appear in Cassini images. RQ1 addresses this issue.

RQ1: What are the expected projections of the rainbow, corona, halo, and glory optical phenomena onto Enceladus' plumes when observed from the ISS and VIMS for a complete 3-dimensional observer geometry?

RQ1 will be answered by completing the tasks in work package 1 (WP1). These include:

- **WP1.1**: Construct a 3-dimensional overview tool of the lighting geometry of scattered light from Enceladus' plumes resulting in the optical phenomena.
  - Write a Python program with fixed Sun-Enceladus reference frame.
  - Create light scattering projections of optical phenomena onto a celestial sphere with the plume at its center for the VIS, NIR, and SWIR using simple ray and diffraction theory.
  - Add spacecraft observation geometries and ISS/VIMS FOVs.
  - Add additional parameters like varying materials, particle sizes and Fresnel reflections.
- **WP1.2**: Build a function in the tool of WP1.1 that projects a simple 2-dimensional outlook of the optical phenomena onto the Cassini images.
  - Add Python function to import Cassini Images and metadata into the tool of WP1.1.
  - Find the lighting and pointing geometry of the Cassini images in the WP1.1 reference frame. Use the metadata on the target geometry generated by Cassini's Autonav software and transform it to the new coordinate system.
  - Project optical phenomena onto image.

The finished projection tool will give a better understanding on where to search for optical phenomena and colour variations in the Cassini images. Next, the focus shifts to how to extract evidence of optical phenomena from Cassini data. First, a general approach must be developed by providing a response to RQ2.

RQ2: How will the plume data be analysed to find signatures of the optical phenomena?

This research question will be answered by adhering to the tasks listed in WP2:

- **WP2.1**: Investigate relative changes in spectral curves within a single VIMS plume cube
  - Analyse results from the WP1 projection tools and select calibrated images with the most desired lighting geometries from NASA's Planetary System Data (PDS) "Planetary Image Atlas" search tool.
  - Select sampling direction. The possible sampling directions are shown in Figure 3.3. The y-direction results in spectra with varying altitudes, the x-direction samples spectral differences in a horizontal slice of the plume, and the radial r-direction compared to the (anti-)solar point allows for comparison of spectra for different phase angles.
  - Extract spectra using the Integrated Software for Imagers and Spectrometers (ISIS) [59]. For example, Hedman et al. [30] sampled pixels from the cube seen in Figure 3.1 similar to the y-direction of Figure 3.3. This allows for comparison of spectral variations in the plumes compared to surface altitude as shown inFigure 3.2.

– Compare spectra and verify possible correlations between spectral variations and the expected optical phenomena.

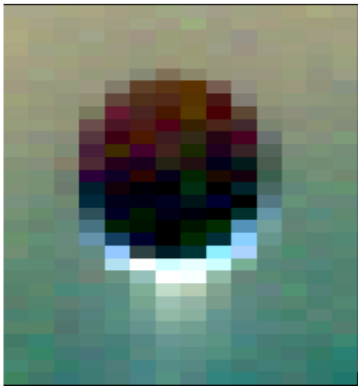

Figure 3.1: Example VIMS cube of Enceladus at mean range of 131,700 km. The red, green, and blue colors correspond to 2.37, 1.70, and 0.88 µm, respectively [30].

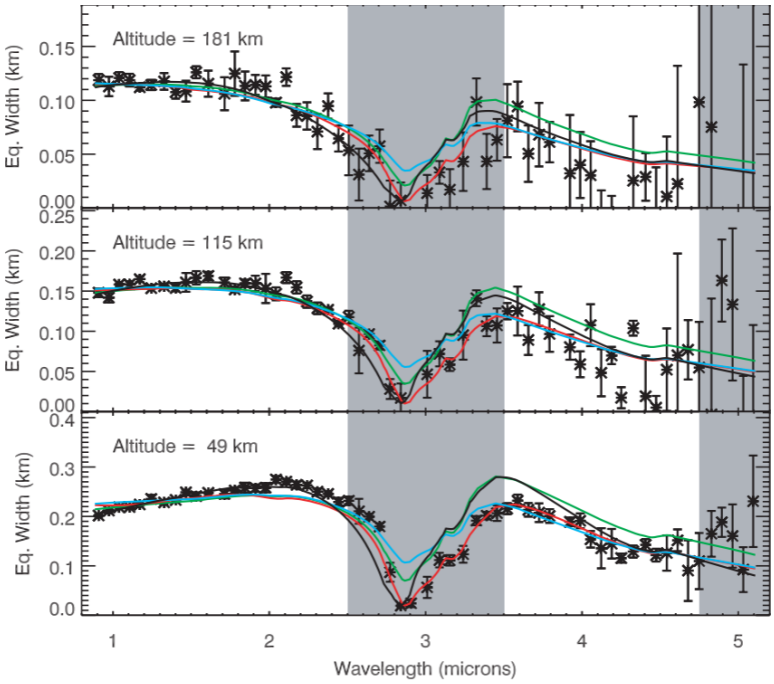

Figure 3.2: Spectra derived from example cube in Figure 3.1. The solid curves depict different scattering models [30].

- **WP2.2**: Investigate variations in standard measure of reflectance I/F from spectral filtered ISS images.
  - Select calibrated ISS image campaigns containing images with different filters taken in quick succession. Multiple of these campaigns need to be selected with similar observed geometry with respect to the plume but at different phase angles. Additional lighting geometry constraints will come from the WP1 tool.
  - Extract I/F profiles of each image for each medium-broad band filter. This will be done by selecting a strip of pixels containing the plume. Possible sampling directions are the same as in WP2.1 (see Figure 3.3). These result in intensity profiles versus sampling direction for a single filter.
  - Compare relative differences between I/F profiles of different filters for a single image campaign with respect to the sampling direction (both WAC and NAC). An example of I/F scans in the x-direction can be seen in Figure 3.4. However, in this research the altitude would be constant and the different I/F curves would represent the different filters.
  - Compare the relative differences between I/F profiles for different image campaigns at varying phase angles but with the same sampling direction (Only NAC)
  - Verify possible correlations between spectral variations and the expected optical phenomena.

The goal of this work package is to first analyse VIMS cubes for spectral variations in WP2.1. If anomalies are found that could indicate optical phenomena, the ISS images are used to investigate the anomaly with higher spatial resolution in WP2.2. It was decided to start with the VIMS measurements because these seem easier to handle. The reason being, larger FOVs which makes it easier to spot spectral variations across the plume, higher spectral resolution, and the convenience of analysing a single image with a single geometry. The ISS images will be more difficult to analyse because of the combination of the broad- and medium-band filters, different image geometries and the smaller FOV of the NAC. To summarise, VIMS images will only be analysed by comparing spectra in a single cube. However, the ISS analysis will also investigate variations among different image campaigns. This was

decided on the basis that the NAC has a very small FOV compared to the VIMS and WAC. This results in images that will likely not show multiple colour bands of the optical phenomena but rather will zoom in a single colour or colour transition. Therefore, spectral variations are harder to observe. To mitigate the narrow FOV, multiple campaigns must be included to compare colour variations over lager phase angle ranges for NAC observations. Specific sampling directions will be selected based of the projections from WP1 tool.

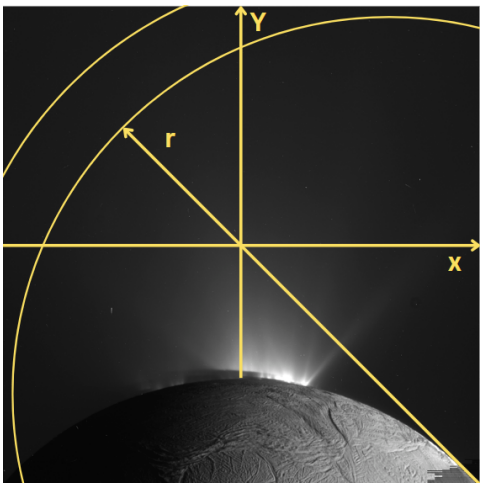

Figure 3.3: Example sampling directions for close-up plume RGB analysis

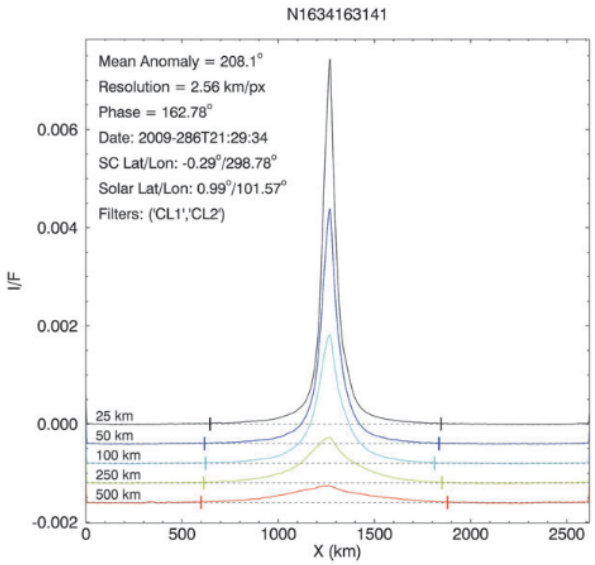

Figure 3.4: The scans of average I/F taken of image N1634163141, The vertical tick marks on the scans in this plot are the X boundaries used to delineate the full extent of the plume [62]

Once the presence or absence of the optical phenomena are confirmed, the next question that should be asked is:

RQ3: What can the (lack of) optical phenomenon signatures reveal about the physical and chemical structure of the plume particles?

Answers to this question will be found through the activities listed in WP3:

- **WP3.1**: Explain possible causes for the presence or absence of the optical phenomena from a theoretical background. Reasoning from atmospheric optics can reveal general information on: particles sizes, shapes, materials and optical thickness.
- **WP3.2**: If a signature is found, compare it to different light-scattering models to test optimal size distributions, particle shapes or material properties.

Next, an attempt will be made to replicate the optical phenomena through plume experiments within a vacuum chamber. RQ4 follows directly from the main research question and seeks to apply the knowledge gained from previous research questions on an experimental scale.

RQ4: Can optical phenomena be observed using artificial plume experiments and what can these reveal about the plumes' composition?

WP4 will answer this question through the following sub-work packages:

- **WP4.1**: Analyse the characteristics of the experimental plume particles from past research and select the most likely optical phenomena that could be recreated.
- **WP4.2**: Create a test set-up, define illuminations and observe geometries compatible with the PISCES laboratory to observe the selected optical phenomena and make observations.

- **WP4.3**: Relate observations to the characteristics of the experimental plume particles (repeat WP3.1 and WP3.2).
- **WP4.4**: Relate the experimental plume observations to the Cassini optical phenomena search results.

Finally, the results of this research can serve as guidelines for future observations by asking the question:

RQ5: What recommendations can be made for future missions to observe and exploit optical phenomena for particle characterisation?

This question will be answered by means of WP5:

- **WP5.1**: Define optimal observation methods (imaging or spectroscopy, filters) and other instrument requirements.
- **WP5.2**: Define optimal observation campaigns in terms of orbital and lighting geometry requirements.
- **WP5.3**: Relate WP5.1 and WP5.2 to upcoming missions to Enceladus or for example, JUICE and Europa Clipper for Europa geyser observations.

3.3. Planning

This thesis is planned in accordance with the Gantt chart below. The project is divided into five different work packages that each correspond to a research sub-question. The work packages are further divided up into sub-work packages. The first work package aims to create a 3D projection model of the optical phenomena according to RQ1. Work package two revolves around RQ2, with emphasis on searching the Cassini VIMS and ISS for signatures of optical phenomena. Following the completion of this work package, a mid-term review will be conducted. Subsequently, work package three involves comparing the data to the plume characteristics. This will be done based on theoretical knowledge first. The following steps depend on the confirmed presence or absence of the optical phenomenon in the data. If signatures of optical phenomena have been identified, the light blue path is continued. Resulting in time being allocated to fit the data to theoretical models while less time will be spent on the experiments in WP4. If the signatures prove to be very scientifically interesting, WP4 could be removed entirely to allow more time for WP3. However, if no phenomena are observed, the purple path will be followed which allocates more time to WP4. Both paths join again upon completion of WP4. Lastly, recommendations for future mission will be drawn up in WP5. Tasks are left open after the draft is submitted; these spots will be filled by flexible tasks that are required at the time.

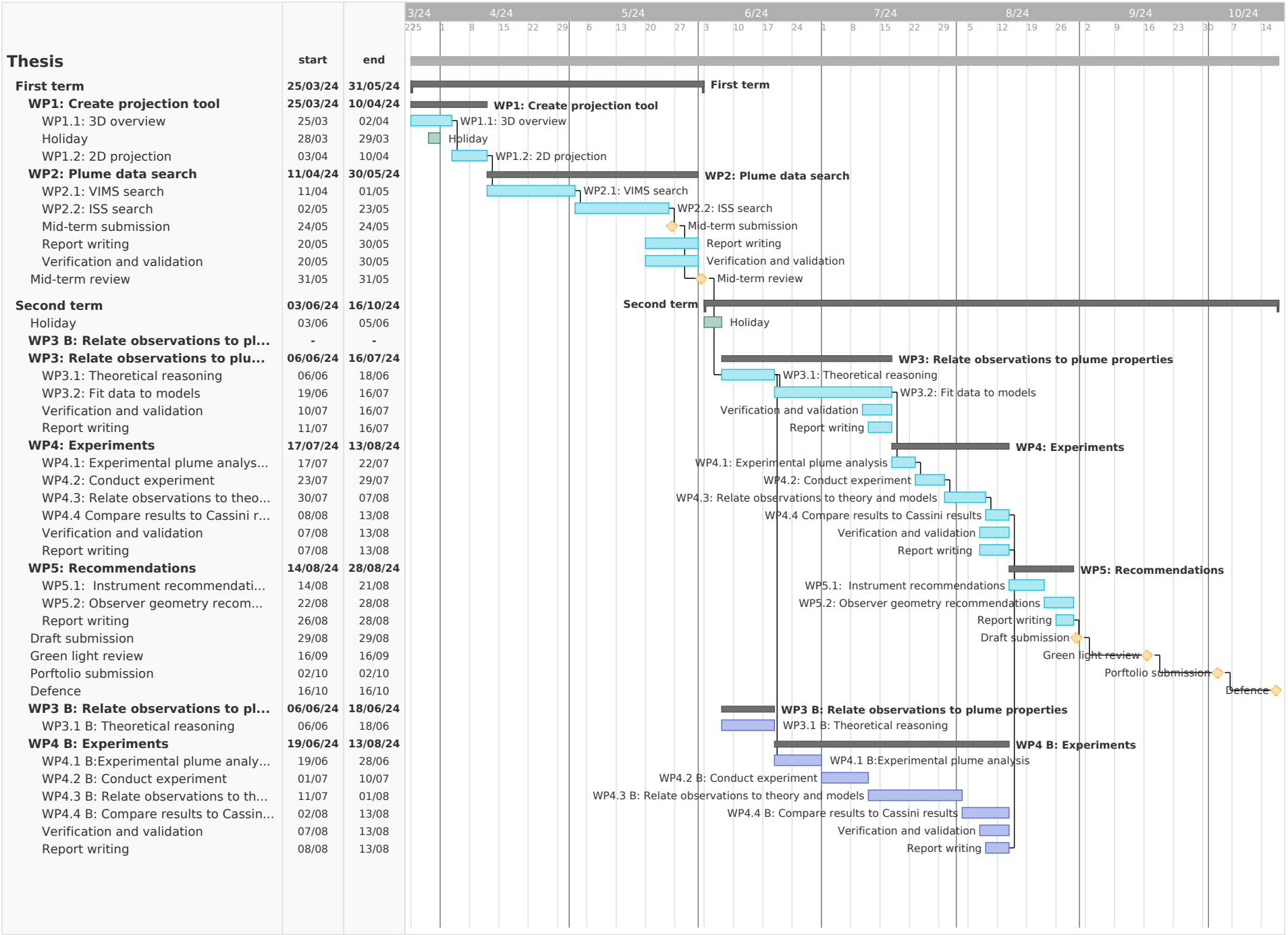

4

Scientific Article

An initial search for the atmospheric corona and ice particle halo in Enceladus' plumes was conducted, following the structure outlined in section 3.2. In alignment with work package one, the necessary tools were developed (described in Appendix B) to verify the observational requirements for optical phenomena in the images. This process produced a set of images from targeted Enceladus flybys, which were analysed using the method detailed in work package two. Line samples taken within individual VIMS and ISS images did not reveal any corona or halo signatures in the selected flybys. Additionally, attempts were made to reconstruct phase intensity functions by combining plume observation intensities throughout a flyby, but this also did not yield a clear corona or halo signature.

During this search for optical phenomena in Enceladus' plumes, peculiar stripe features were discovered. This anomaly did not match any known atmospheric phenomena mentioned in chapter 2. However, various indicators, such as its appearance in both VIMS and ISS instruments, suggested that it was a physical phenomenon rather than stray light. As a result, the following research effort aims to explain this anomaly. This chapter contains the research findings written in Elsevier's scientific article style with the intention of submitting it to the Icarus scientific journal dedicated to the field of planetary science.

Appendices with results are directly attached to this article. Additional information, such as an explanation of the tools used to investigate the optical phenomena and stripe features, can be found in Appendix B, which is separate from the article.

Discovery of an Inclined Periodic Structure in the Saturnian System

Niels Rubbrecht[a], Stéphanie Cazaux[a], Jérôme Loicq[a], Benoît Seignovert[b], Matthew Kenworthy[a,c], Nicholas Kutsop[d] and Stéphane Le Mouélic[b]

[a]Faculty of Aerospace Engineering, Delft University of Technology, Kluyverweg 1, Delft, 2629 HS, The Netherlands
[b]Observatoire des Sciences de l'Univers Nantes Atlantique, Campus Lombarderie, 2 rue de la Houssinière, Nantes, 44322, France
[c]Leiden Observatory, Leiden University, P.O. Box 9513, Leiden, 2300 RA, The Netherlands
[d]Department of Astronomy, Cornell University, 404 Space Sciences Building, Ithaca, NY, 14853, United States

ARTICLE INFO

Keywords:
Saturn, rings
Planetary rings
Ices, IR Spectroscopy
Diffraction grating
Enceladus

ABSTRACT

We report observations of stripe-like features in Enceladus' plumes captured simultaneously by Cassini's VIMS-IR and ISS NAC instruments during flyby E17, with similar patterns seen in VIMS-IR data from flyby E13 and E19. These parallel stripes, inclined at approximately 16° to the ecliptic and 43° to Saturn's ring plane, appear continuous across images when projected in the J2000 frame. A bright stripe, most visible at wavelengths around 5 µm, acts as the zeroth-order diffraction peak of a reflection grating with an estimated groove spacing of 0.12–2.60 mm, while adjacent stripes are attributed to higher-order diffraction peaks. Two hypotheses are proposed to explain this phenomenon. The first suggests an ordered structure within the orbits of Saturn's Norse group moons acting as a reflection grating. This hypothesis is supported by the similar inclinations of the stripes to the Norse group orbits as well as the apparent stripe alignment between the images. The second hypothesis posits an inclined ordered structure within Saturn's E-ring, which could explain the stripes appearing brighter and in front relative to Enceladus.

1. Introduction

Since reaching the Saturnian system in 2004, NASA's Cassini spacecraft has revolutionised our understanding of Saturn, its rings, and its diverse moons (Spilker, 2019). Among Cassini's most significant discoveries was the detection of active water-ice plumes erupting from Saturn's icy moon, Enceladus (Porco et al., 2006). Cassini's remote sensing instruments, including the Imaging Science Subsystem (ISS) and Visual and Infrared Mapping Spectrometer (VIMS), detected light scattered by the micrometre-sized ice particles ejected from fissures on the moon's south polar region (Ingersoll et al., 2020). These observations have proven essential for refining models of plume particle size distributions and their dynamics (Hedman et al., 2009b; Ingersoll and Ewald, 2011). It became evident that these plumes represent the primary source of particles contributing to Saturn's diffuse E-ring (Schmidt et al., 2008; Kempf et al., 2008).

The plumes and E-ring provide a unique opportunity to investigate Enceladus' internal processes and evolutionary history. In-situ analysis of E-ring particles with Cassini's Cosmic Dust Analyzer (CDA) revealed the presence of ice enriched in sodium salts (Postberg et al., 2009). When combined with gravity field measurements (Park et al., 2024), these findings support the existence of a global subsurface ocean beneath Enceladus' icy crust, from which the plumes originate. As a result, the plumes and E-ring particles provide direct samples of this subsurface ocean. Subsequent research detected complex organic molecules in the icy grains of the plumes (Postberg et al., 2018; Choblet et al., 2022). These findings point to a potentially habitable environment beyond Earth, which makes Enceladus a prime target for future missions aimed at searching for extraterrestrial life (Carr et al., 2013; Porco et al., 2017). This emphasis is further supported by ESA's Voyage 2050 program, which prioritizes the exploration of icy moons, including Enceladus, as part of its long-term strategy for Solar System exploration (Favata et al., 2021). Awaiting future missions, Cassini's extensive observations from the ISS and VIMS continue to yield new scientific insights nearly 20 years after its initial deployment, e.g. Morello and Berg (2024) and Denny et al. (2024).

This report introduces a novel remote-sensing technique aimed at characterising particles within Enceladus' plumes by observing optical phenomena similar to those seen in the Earth's atmosphere, such as rainbows and halos (Lynch and Schwartz, 1991; Tape and Moilanen, 2006). These phenomena result from light interactions with particles like water droplets or ice crystals, providing insights into particle properties through unique visual effects and specific occurrence conditions (Laven, 2004; Nussenzveig, 2012; Moilanen and Gritsevich, 2022). While rare beyond Earth, such phenomena have been recorded elsewhere in the Solar System. For instance, the Venus Express orbiter captured a glory on the upper cloud layer of Venus, shedding new light on the material and size distribution of the cloud particles (Markiewicz et al., 2014; Petrova et al., 2015). Similarly, the Mars Perseverance rover documented an ice particle halo created by hexagonal ice crystals within water-ice clouds, offering new insights into Martian cloud formation conditions (Lemmon et al., 2022).

Images of Enceladus' plumes captured by the ISS and VIMS instruments offer a unique opportunity to observe similar optical phenomena. These remote-sensing techniques rely on scattered light from particles within the optically thin plumes (Ingersoll et al., 2020), conditions

reminiscent of those that produce rainbows and halos in the Earth's atmosphere. In the search for optical phenomena in Enceladus' plumes, we identified faint stripe-like features captured simultaneously by Cassini's ISS and VIMS instruments. This study aims to investigate these features in detail and link them to underlying physical processes.

This paper is articulated as follows. Cassini VIMS and ISS observations of the stripes in Enceladus targeted flybys E13, E17, and E19 will be detailed in section 2. These, stripe observations will be characterised in terms of spectral variations, source location, and material properties in section 3. In section 4, two hypotheses will be proposed and discussed for the potential origin of the stripes.

2. Stripes in Cassini ISS & VIMS Observations

This section reports an overview of Cassini's observations of similar stripes in the ISS and VIMS during its targeted flybys of Enceladus (E13, E17, and E19). These measurements will then be compared and related to Cassini's observation geometry for the Saturnian system.

2.1. ISS Data Retrieval

The ISS, detailed in Porco et al. (2004), consists of two fixed focal length telescopes: the Narrow Angle Camera (NAC) and the Wide Angle Camera (WAC). The NAC has a field of view (FOV) of 0.35° × 0.35° and a spectral range of 200–1100 nm, while the WAC offers a wider FOV of 3.5° × 3.5° and a spectral range of 380–1100 nm. Both cameras use filter wheels to combine spectral filters for flexible imaging capabilities. This research solely focuses on NAC images which have an angular resolution of 6 µrad/pixel. The images are retrieved from NASA's PDS Ring-Moon Systems Node's OPUS search service and calibrated using the CISSCAL 4.0 pipeline (Porco et al., 2004) to convert raw data to I/F, which is a standardised measure of reflectance that equals unity for a Lambertian surface at normal incidence and emission. The Cassini ISS data is handled using the Integrated Software for Imagers and Spectrometers (ISIS) version 8.0.0 developed by the USGS Astrogeology Science Center (Laura et al., 2023).

2.2. VIMS Data Retrieval

The VIMS instrument, described in Brown et al. (2004), is a spectrometer which records spectra at 352 wavelength channels, ranging from 0.35 to 5.2 µm, over a maximum viewing window of 64 × 64 spatial pixels. The resulting spectral map is known as a "cube." It has two different channels focusing on either visible (VIS) or infrared (IR) wavelengths. This study focuses solely on the IR channel, which captures spectra at 256 wavelengths between 0.85 and 5.1 µm, with an average spectral resolution of 16 nm and an angular spatial resolution of 0.25 x 0.5 mrad. VIMS-VIS data was not acquired for most of the observations used in this report and is therefore not used in the subsequent analysis. The calibrated VIMS-IR spectral cubes are directly downloaded from vims.univ-nantes.fr, which contains a collection of multispectral summary products created by Le Mouélic et al. (2019). These cubes are handled using the PyVIMS (Version 1.0.4) - Zenodo Python package from Seignovert et al. (2023).

2.3. Flyby E17

Stripe features were first identified in observations during Cassini's Enceladus targeted flyby E17. This subsection discusses the stripe observations captured by the ISS and the VIMS, analyses them within the context of the flyby approach, and compares the findings from both instruments.

2.3.1. Initial ISS Observations

Figure 1 a) shows ISS NAC image N1711553432 of Enceladus' South pole and its plumes captured during targeted flyby E17. The image is shown over an I/F range between 2.4×10^{-4} and 2.8×10^{-3}. In this high phase (160°) observation, the forward scattering of light hitting the plume particles reveals two bright jets emanating from Enceladus' body, which appears darker against the E-ring background. In Figure 1 b), the same image is shown but with a linear I/F stretch between 4.7×10^{-4} and 7.6×10^{-4}. This range highlights three faint parallel stripes that appear oriented from the image's top left to the bottom right corner. The I/F of the stripes is one order of magnitude lower than that of the brightest areas of the jets.

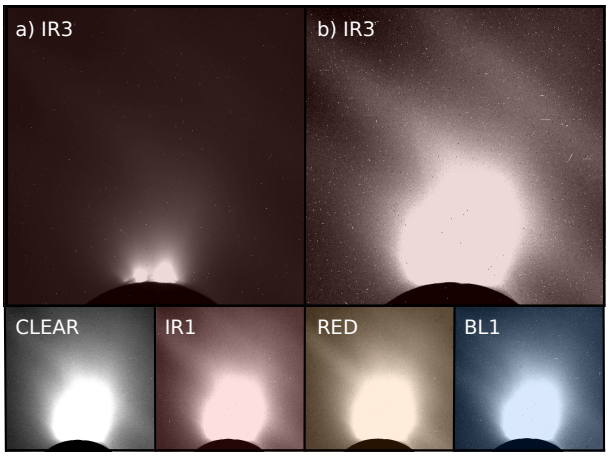

Figure 1: a) Cassini ISS NAC image N1711553432 of Enceladus' plumes with I/F linear stretch of $[2.4 \times 10^{-4}, 2.8 \times 10^{-3}]$, and b) $[4.7 \times 10^{-4}, 7.6 \times 10^{-4}]$. The bottom row shows images N1711553312, N1711553502, N1711553572, and N1711553692, respectively, with the latter I/F stretch.

The bottom row of Figure 1 displays four additional images, each captured within a maximum time difference of five minutes from N1711553432, resulting in similar observational geometries. Each image was taken using a different broad or medium-band filter, with the filter names indicated in the top left corners. In every image, similar parallel stripes can be seen. These stripes are thus visible across a spectral range covering both the visible and the near-infrared.

2.3.2. ISS Mosaic

To investigate the extent of the stripe features found in Figure 1, the same linear stretch is applied to all plume images captured during Cassini's E17 approach. A total of ten images have been found to contain similar stripe features. The final 16 images out of the 60 captured during the E17 approach are mosaicked based on their right ascension (RA) and declination (DEC) in the J2000 reference frame. Here, the ISS NAC image corner coordinates are retrieved from "SPICE" (Spacecraft, Planet, Instrument, C-matrix, Events) system, designed by NASA's Navigation and Ancillary Information Facility (NAIF) (Acton, 1996) for the observation mid-times.

Projecting these coordinates results in the mosaic shown in Figure 2. During the approach, the ISS NAC cycles through a filter sequence in the order CLEAR–IR3–IR1–RED–BL1 in quick succession. After a short waiting period, the sequence repeats. In the mosaic, images captured at a later time are superimposed on the earlier ones. Therefore, images captured in a single sequence would appear overlapped due to the minor variation in observation geometry. To allow for comparison in Figure 2, the projections are separated for each filter by a DEC offset of $-0.5°$. The original mosaic coordinates are displayed for images captured with the IR3 filter. The imaging sequence starts from the right side of the figure at $RA = 9.2°$ with the first IR3 image and ends with the last BL1 image at $RA = 10.5°$. The observations in Figure 2 were further processed by subtracting the CLEAR images from the same sequence. This subtraction reduces the plumes' background brightness, enhancing the stripe features' visibility. The CLEAR and filtered images were subtracted without precise alignment, as the similar observational geometries within each filter sequence made this approach adequate.

The mosaic reveals that stripe features are visible only in the last eight images of the E17 approach, with the final four corresponding to those shown in Figure 1. The stripes appear near-continuous across images taken with the same filter. However, there is a slight misalignment where the last image is shifted by $DEC \approx 0.1°$ compared to the second-to-last image. This misalignment could result from small pointing errors in the SPICE kernels. Nevertheless, the intensity variations remain consistent across the images, as seen in the order and intensity of the bright and dark regions in the IR1 images.

Comparing different filters reveals notable differences: the IR3 filter shows fewer, thicker stripes with high contrast, while the visible filters display more numerous, thinner, and closely spaced stripes. Stripe visibility also changes across filters, with some stripes appearing or disappearing depending on the filter used. Despite these variations, the stripes consistently run parallel throughout the mosaic and are inclined approximately 16° with respect to the ecliptic and 43° inclined to Saturn's ring plane. An overview of the key observational parameters of the E17 images containing stripe features is shown in Table 1. Here, the phase is the mean phase angle of the pixels in the observation window.

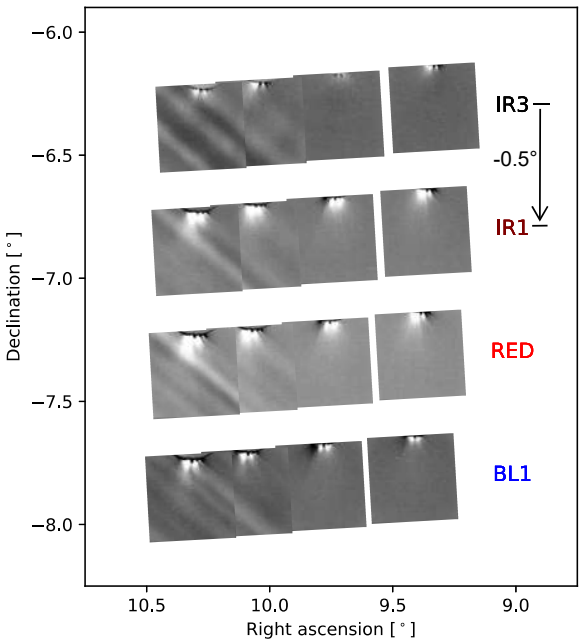

Figure 2: Cassini flyby E17 ISS NAC mosaic in terms of right ascension and declination in the J2000 reference frame for different medium-band filters. Images were subtracted by the nearest CLEAR filter image and have an I/F range of $[-10^{-4}, 10^{-4}]$. The original mosaic is given on top; every following filter mosaic is shown with an additional declination of $-0.5°$ for clarity.

Table 1
E17 ISS NAC images containing stripes.

Image ID	Image Mid Time	Filter	Phase [°]
N1711552042	2012-03-27 14:15:56	CLEAR	160.22
N1711552162	2012-03-27 14:17:24	IR3	160.23
N1711552232	2012-03-27 14:19:02	IR1	160.25
N1711552302	2012-03-27 14:20:13	RED	160.26
N1711552422	2012-03-27 14:21:50	BL1	160.27
N1711553312	2012-03-27 14:37:06	CLEAR	160.39
N1711553432	2012-03-27 14:38:34	IR3	160.40
N1711553502	2012-03-27 14:40:12	IR1	160.41
N1711553572	2012-03-27 14:41:23	RED	160.42
N1711553692	2012-03-27 14:43:00	BL1	160.43

2.3.3. Initial VIMS Observations

During Cassini's E17 approach to Enceladus, simultaneous observations were made using the ISS and VIMS instruments. Figure 3 shows VIMS cube 1711553290 which was captured with an image mid-time 35 seconds later than ISS NAC image N1711553432 from Figure 1. The top of the figure shows the I/F values of the cube at wavelength $\lambda = 0.92$ µm, which is similar to the central wavelength of the ISS IR3 filter ($\lambda = 0.93$ µm) (Knowles, 2018). For comparison, the same stretch of I/F values is used as in Figure 1 a). The dark body of Enceladus, highlighted in red, is seen against the faint E-ring background. The bright

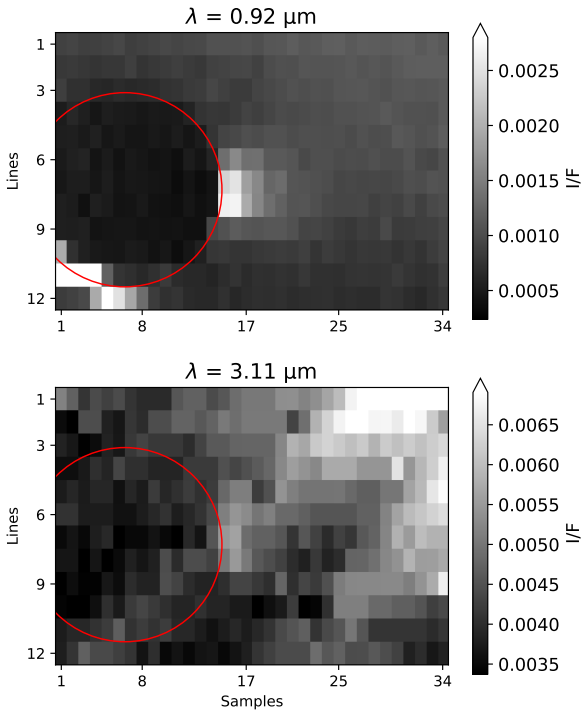

Figure 3: Cassini VIMS cube 1711553290 with Image Mid Time = 27/03/2012 14:39:09 showing I/F for wavelengths 0.92 μm and 3.11 μm. The limb of Enceladus is highlighted in red for reference.

pixels in the lower left corner of the image are the limb of Enceladus illuminated by the Sun. The bright pixels in the centre of the image are caused by the forward scattered light from the plumes. No stripes can be identified in this image, as was the case for Figure 1 a). Considering an interval of the I/F values similar to ISS shown in Figure 1 b) leads to the saturation of most of the pixels in the image and thus was not reported. However, the same cube for $\lambda = 3.11$ μm is reported instead, highlighting a large diagonal stripe, which is brightest in the top right corner and reduces in intensity when moving to the bottom left corner of the image. Note that the stripe appears in front of the dark body of Enceladus. A second stripe can be observed to the right of the former. Both stripes appear approximately parallel to each other. In addition, the bright region in the corner is significantly brighter than the plume itself with an increase of $I/F \approx 10^{-3}$.

2.3.4. VIMS Mosaic

Similarly to the ISS observations, VIMS cubes were captured during the entire flyby E17 approach. These are mosaicked according to their RA and DEC coordinates in the J2000 reference frame as shown in Figure 4. The projected pixel coordinates are directly retrieved via PyVIMS. This figure shows every cube from the beginning of the E17 flyby ($RA \approx 1°$) up to the last cube 1711553290 ($RA \approx 11°$) for a total of 56 cubes. Observations start at a phase angle of 154° and a distance of 3.4×10^5 km from Enceladus, which evolve to a phase angle of 160° and a distance of 1.2×10^5 km at the final cube. During the approach, VIMS continuously tracks Enceladus, ensuring the moon remains in roughly the same pixel location relative to the instrument for each observation. This is illustrated by a few sample cubes extracted from the mosaic, where Enceladus' body is marked with a red circle. In the mosaic, each consecutive image is overlaid onto the previous one. As a result, Enceladus is only visible in the final image, although it is present in each cube near the top centre of the image window.

The flyby mosaic is shown for a discrete set of wavelengths (indicated on the right). The chosen wavelengths are based on milestones in the VIMS-IR spectral range, which represent a significant shift in the cube appearances. The original projection is shown at the top for $\lambda = 0.89$ μm, plotting each subsequent wavelength with an additional declination offset of $-0.5°$ for comparison. In reality, observations for every wavelength have the exact same projected location in the mosaic. The pixel intensities are normalised over all E17 cubes at a single wavelength, providing a relative view of the intensity throughout the flyby.

Starting from the shortest available wavelength channel of 0.89 μm, no stripes can be seen throughout the flyby. However, the pixel region around $RA = 9.8°$ and $DEC = -6.5°$ shows a faint brightness increase over multiple images. This region becomes increasingly bright as the wavelength increases. By the 1.48 μm channel (shown on the second row in Figure 4), this bright area has grown to be approximately as bright as Enceladus' plumes.

The first stripes appear at $\lambda = 2.24$ μm (third row). These parallel stripes become more visible and brighter as Cassini approaches Enceladus, starting from $RA > 5°$. The bright area around $RA = 9.8°$ remains, exhibiting the most visible stripes. It is important to note that the stripes are continuous over multiple overlapping cubes. As the wavelength increases, the stripes become brighter and more distinct, as shown for $\lambda = 3.11$ μm (row 4). At this point, the bright area is much brighter than the plumes of Enceladus. Additionally, when comparing rows 3 and 4, it becomes evident that the position and brightness of the stripes change with wavelength.

The stripes remain visible at the longer wavelength of $\lambda = 4.26$ μm (row 5), with continued variations in position and brightness. A single bright stripe at $RA = 8.2°$ stands out, also faintly visible at $\lambda = 3.11$ μm. Finally, at $\lambda = 5.11$ μm (row 6), the end of VIMS-IR's available spectrum, the data becomes increasingly noisy, and most stripes fade away. However, the single bright stripe at $RA = 8.2°$ persists. Regardless of wavelength, all stripes in the mosaic are parallel and inclined to the ecliptic by approximately 16° which is the same inclination observed in the ISS mosaic.

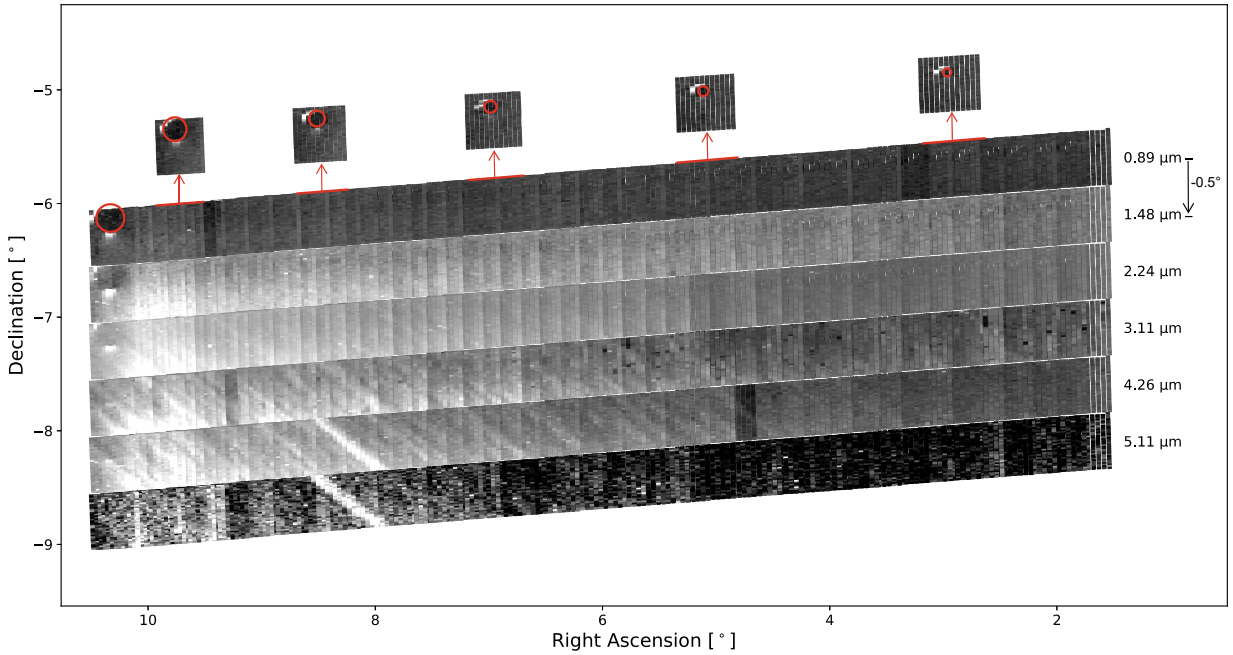

Figure 4: Cassini flyby E17 VIMS mosaic in terms of right ascension and declination in the J2000 reference frame for a discrete set of wavelengths. The original mosaic is given on top; every following wavelength mosaic is shown with an additional declination offset of −0.5° for clarity. The body of Enceladus is marked by a red circle for reference.

2.3.5. Comparison between ISS and VIMS Stripes

Unlike the few stripes observed in the ISS data, clear stripes appear in almost every VIMS cube captured during the E17 approach. In Figure 5, a combined mosaic of ISS NAC image N171155216 and four VIMS-IR cubes captured around the same time during flyby E17 is shown. This figure proves that the stripe direction is the same in the VIMS and ISS observations. The stripe width is also similar, with an angular size range of 0.5 to 1.5 mrad. This is comparable to the apparent angular diameter of the Sun at Cassini's position, which is approximately 1 mrad.

As the VIMS and ISS instruments have completely separate optics (Brown et al., 2004; Porco et al., 2004), the stripes cannot be caused by stray light originating from within the instruments. Therefore, it must have an external origin. This conclusion is further supported by the continuous appearance of the stripes across images, a characteristic not typically associated with stray light. In-flight calibration of the ISS-NAC revealed a prominent stray light artefact that appears as a diagonal streak of light (see Figure 18 from West et al. (2010)). This artefact originates from a bright object just outside the ISS NAC's field of view, like a moon. However, this artefact is dependent on the off-sight object's position. In Flyby E17, the position of Enceladus remains fixed in the image window for each observation. Therefore, if a similar artefact occurs, it would also be fixed in the same position relative to Enceladus in each image window. This is not the case. Unfortunately, these results cannot be compared to known VIMS artefacts as no in-flight stray light analysis was performed for this instrument (Brown et al., 2004).

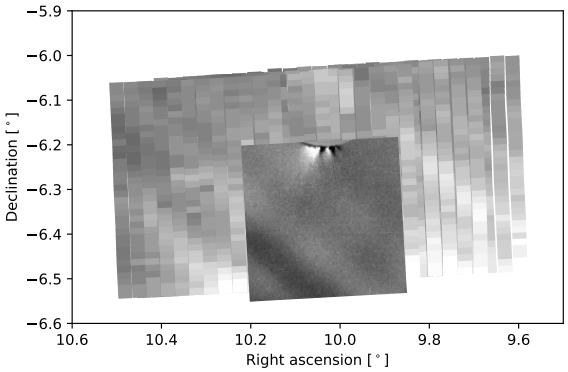

Figure 5: Cassini flyby E17 VIMS and ISS combined mosaic in terms of right ascension and declination in the J2000 reference frame. ISS NAC image N1711552162 taken in IR3 filter and subtracted by closest geometry CLEAR filter image with VIMS cube $\lambda = 3.11$ µm.

2.3.6. Cassini Observation Geometry

An overview of the observation geometry of Cassini during flyby E17 is shown in Figure 6. Starting from the edge-on view of Saturn's ring plane, it can be seen that at the beginning of the approach, Cassini is at a distance of 8.5 R_S (Saturn Radii) and at an altitude of 2600 km above the ring plane. During its approach, Cassini moves closer to Saturn and the ring plane. The observation window of the bright band observed by six VIMS cubes in Figure 4 is shown in

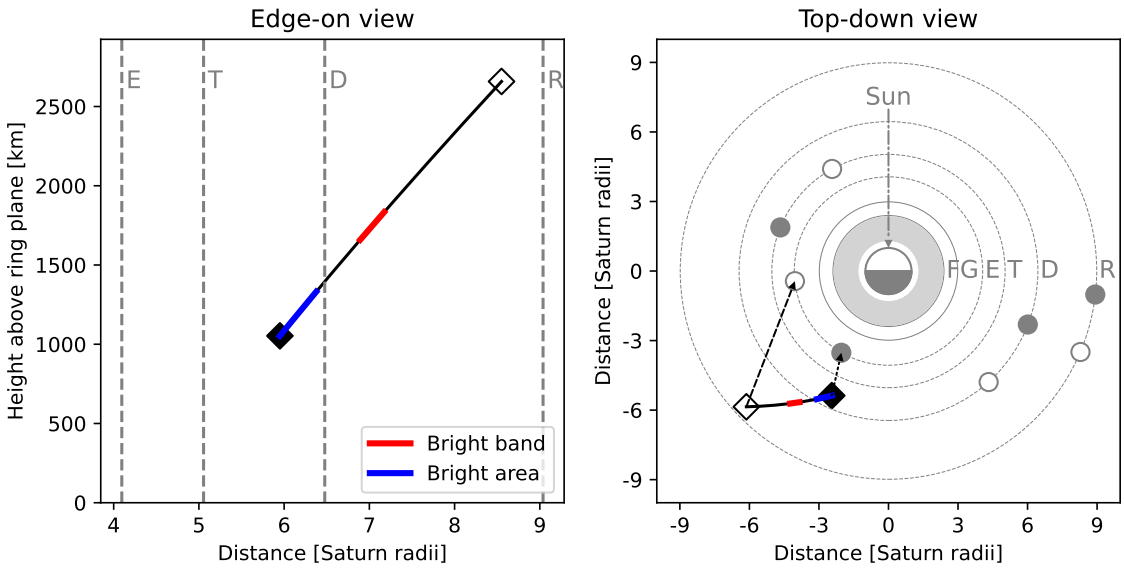

Figure 6: Cassini's E17 flyby geometry on 27/03/2012 from 09:53:14 to 14:49:33 UTC, shown from a Saturn-centered perspective with edge-on (left) and top-down (right) views of Saturn's ring plane. Cassini's position is marked by a diamond, and the moons' positions are indicated by circles. The open symbol represents the start position, and the filled symbol represents the end position. The orbits of Enceladus, Tethys, Dione, and Rhea (E, T, D, R) are represented by dashed grey lines, while the F-ring and G-ring (F, G) are shown with solid grey lines. The solar direction is indicated by a dash-dotted arrow, and the ISS/VIMS viewing direction by black dashed arrows.

red. The bright band appears for a range of $6.9 < R_S < 7.2$, before crossing Dione's orbit. Shortly after this crossing, the bright area appears and remains visible till the end of the imaging approach. A top-down view is shown on the right side of Figure 6, revealing the observed sections of Saturn's inner moon system. Note that the Sun's elevation above the ring plane is not zero but 13.7° North from the centre of the ring plane. The bright stripe is visible when the F-ring should appear in the background of the field of view. In addition, the G-ring and other inner rings (indicated by the grey area) can also be present in the background of images after the bright band observations.

2.4. Search Methodology for Similar Stripe Observations

To investigate the nature of the stripes it is important to consider their possible appearance in other observations. To this end, Cassini ISS NAC and VIMS-IR observations with similar observation and illumination conditions to flyby E17 were checked. The image search is separated into two components: images containing Enceladus' plumes and images of other targets (without plumes).

The selection criteria for the ISS NAC images flybys are based on the phase angles of the E17 flyby images where stripes were observed. Specifically, the stripes appeared at phase angles ranging from 160.2° to 160.4°. Consequently, flybys with phase angles within this range with an added boundary ±2° are included in this analysis. This boundary results in conservative geometry requirements while increasing the number of observations (previously 80). The ISS NAC images in each flyby are first analysed by applying a linear stretch of the I/F values so that the plumes are saturated. This method reveals the faint stripes in flyby E17 as shown in Figure 1. Secondly, observations in the CLEAR filter are subtracted from images captured with medium/broad-band filters (if available). This method reveals clear stripe signatures without manually adjusting the pixel intensity scale. No stripes in ISS NAC images were found after applying both checks.

Stripes in the VIMS cubes can be identified more straightforwardly by visually inspecting cube previews available in the VIMS Data Portal from Le Mouélic et al. (2019). The stripes observed in Figure 4 from flyby E17 are clearly visible in these previews, which show the cubes at wavelengths of 1.78, 2, 3.1, 3.45, and 5 µm. As a result, this method proves to be a quick and efficient way to locate similar stripes across other targeted flybys. Consequently, every targeted flyby of Titan, Enceladus, Dione, Rhea, Phoebe, Tethys, Hyperion, and Iapetus was checked for stripes. This analysis identified similar stripe features in two additional Enceladus-targeted flybys: E13 and E19. Candidate stripes with differing appearances were also

found. Examples include cubes targeting Dione, Rhea, Titan, and Tethys as shown in Figure 16. These show bright parallel stripes at similar wavelengths to the stripes in E17. However, either not enough observations are available to mosaic the stripes or the stripes do not align between images. Additional key differences in appearance are stripes that are strictly localised to the lowest-phase corner of the image, an additional set of stripes perpendicular to the other stripes, and stripes that are perfectly parallel to the sun-direction vector (flyby E17, E13 and E19 show an off-set to this vector). Therefore, these observations are disregarded in the subsequent analysis.

2.5. Flyby E13

Figure 17a presents a mosaic of the E13 flyby cubes at various wavelengths, revealing several notable similarities to the flyby E17 observations shown in Figure 4. Stripes are visible for wavelengths between 2.24 µm and 4.26 µm, and they remain continuous across the cubes, as can be seen in the second and third cubes at $\lambda = 3.10$ µm. The stripes appear parallel and are inclined 16° to the ecliptic, the same inclination of the stripes in flyby E17. The stripes in flyby E13 have an angular thickness of approximately 0.7–2.6 mrad, similar to the stripes observed in flyby E17.

Despite these similarities, several key differences exist between the E13 and E17 flybys. Unlike E17, no localised bright area is visible in E13, and the consecutive cube observations alternate between darker and brighter overall intensity. The stripes at $\lambda = 4.26$ µm are significantly less bright than those at $\lambda = 3.10$ µm, while for E17, there is no such difference. Additionally, E13 lacks the bright band and exhibits less global intensity overall at $\lambda = 5.11$ µm. Due to an instrument artefact creating horizontal stripes and an increased background brightness, ISS NAC images taken at the same time could not be brightened to detect faint stripe features in the plumes.

Cassini's observer geometry compared to Saturn's ring plane is shown in Figure 18. From the edge-on view, it can be seen that Cassini is located closer to the ring plane than in flyby E17, with a ring plane altitude ranging from 150 km to 225 km. From a top-down perspective, Cassini observes Enceladus from the inner edge of the E-ring rather than the outer-edge as for flyby E17. The phase has increased by 4° compared to the maximum phase in flyby E17 with a phase angle of 164° at the start of the E13 approach to 165° at the end.

2.6. Flyby E19

Figure 17b presents a mosaic of 11 VIMS cubes in flyby E19 at the same discrete wavelengths as the previous mosaics. All cubes in this range appear to be located within a bright area, with an intensity roughly consistent with the bright area observed in E17. Stripes are visible for the same spectral range as flyby E17 between 2.24 µm and 4.26 µm, and remain continuous across the cubes. The stripes are parallel and inclined 16° to the ecliptic, just like the flyby E13 and E17 stripes. Stripe width is approximately 0.6–1.1 mrad.

Differences between E17 and E19 include a brightness increase in the low-phase corner of the E19 images that does not appear to correlate with the continuous stripes mapped in the RA and DEC projection. This non-continuous shift in brightness between cubes can be seen in the final cube, which has a slight DEC increase. Additionally, the E19 flyby lacks the bright band observed in E17. ISS NAC images at the same observation time during flyby E19 are available. Stripes were sought according to the method described in subsection 2.4 but could not be detected. A potential cause for this could be that the ISS NAC stripe observations are phase-dependent and only show stripes for the highest phase images (>160°) as seen in flyby E17. The flyby E19 ISS NAC images have a mean phase of 159.5° which is similar to the right-most images in Figure 2. These images also do not show stripes. So, the observations between flyby E17 and E19 can be consistent, assuming a phase-dependent stripe visibility.

Figure 19 illustrates a similar observation geometry in flyby E19 as in flyby E17, with Cassini positioned at the same altitude above the ring plane as during the bright area observation of E17. The radial distances from Saturn are also comparable, with the approach beginning shortly after crossing Dione's orbit and concluding midway between the orbits of Tethys and Dione, mirroring the conditions during the bright area observations in E17

2.7. Stripe Observation Summary

An overview of the stripe observations is provided in Table 2, encompassing four independent detections by the Cassini ISS and VIMS instruments. The recorded stripes are observed during high-phase, Enceladus-targeted observations, all showing a consistent inclination of 16° relative to the ecliptic. The simultaneous detection of the stripes in both ISS and VIMS during Flyby E17, along with the continuity of the stripes between the mosaicked images, suggests an external origin rather than stray light. The stripes' angular widths vary from 0.5 to 2.6 mrad. These may appear brighter and in front of Enceladus. Their visibility depends on the observed wavelength, with peak visibility in the VIMS data at wavelengths between 2.2 and 4.3 µm for all flybys. Notably, stripes detected in VIMS-IR do not necessarily correspond to stripes in the ISS NAC under the same observation geometry. This may be due to reduced stripe visibility at wavelengths below 2.2 µm (as seen in VIMS flybys E13, E17, and E19) combined with a phase angle dependence, where stripes are visible only at phase angles greater than 160°. A distinct bright stripe, referred to as the "bright band", emerges in flyby E17 at $\lambda > 4.26$ µm, which stands out from the other stripes. The observations, spanning up to 1.37 years apart, suggest that the stripe phenomena may persist for at least that duration.

A summary of the top-down geometry of the VIMS stripe observations relative to the Saturn system and aligned with Saturn's solar illumination is presented in Figure 7. All observations were conducted when Cassini was near the ring plane and within the extent of the E-ring. Flybys E17 and

Table 2
Summary of stripe observations.

Flyby	Instrument	Time Range [UTC]	Phase Range [°]
E13	VIMS-IR	2010-12-20 22:53:39–2010-12-21 00:00:40	164.0–165.0
E17	VIMS-IR	2012-03-27 09:53:14–14:43:56	154.0–160.3
E17	ISS	2012-03-27 14:15:56–14:43:00	160.2–160.4
E19	VIMS-IR	2012-05-02 05:07:13–06:02:00	159.0–160.0

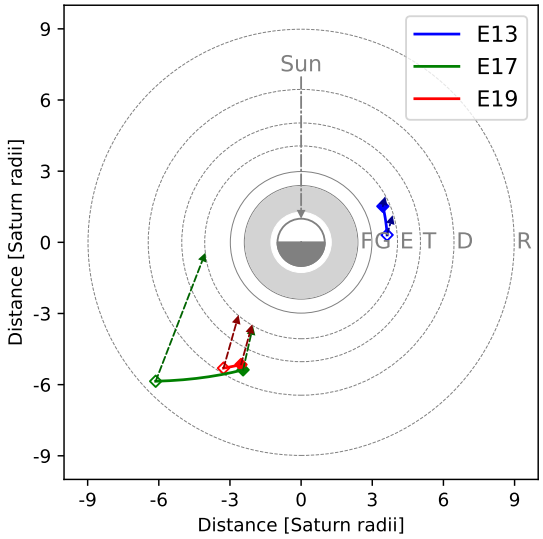

Figure 7: Observation geometry summary of flybys containing VIMS stripe features represented in a top-down view of Saturn's ring plane.

E19 exhibit very similar viewing geometries, with Cassini positioned between the orbits of Tethys and Rhea, facing Saturn. In contrast, flyby E13 features a different geometry, with Cassini located between the G-ring and Enceladus' orbit, this time looking away from Saturn.

From the flyby mosaics shown in Figure 4, Figure 17a, and Figure 17b, it became apparent that the stripes are fixed in RA and DEC space. Yet, Enceladus's location is not; it traces its orbit with time, as seen from the Enceladus-centered VIMS cubes (each cube contains Enceladus in the same area of the viewing window). Therefore, the observed stripe phenomenon occurs in a system decoupled from the motion of Enceladus and can thus not occur due to a physical structure which co-rotates with Enceladus orbit. This means that the origin of the stripes likely lies in front or behind Enceladus along Cassini's line of sight. Different hypothesis will be discussed in section 4.

3. Stripe Characterisation

The objective of this section is to characterise the stripe features observed in the Cassini ISS and VIMS data. This will involve examining the spectral variations in the appearance of the stripes, leading to the identification of the source of the stripe features. Subsequently, we will analyse the material responsible for the formation of these stripes.

3.1. Spectral Variations & Source Localisation

The ISS images and VIMS cubes show spectral dependencies in the intensity and positioning of the stripes. This section aims to analyse these effects and identify their origin. We will start by examining spectral variations in individual observations, followed by a comparative analysis across multiple flyby images. Finally, we will identify the source of the stripes and determine its location within the Saturn system.

3.1.1. Stripe Spectral Dependencies within Single ISS and VIMS Images

We compare the spectral variations between the simultaneous flyby E17 ISS NAC and VIMS stripe observations. For the ISS these include the last sequence of images corresponding to the last four entries in Table 1 and the leftmost images in each filter in Figure 2. The VIMS cube 1711553290_1 previously shown in Figure 3 is used for comparison with a mid-time between the IR3 and IR1 ISS images.

The intensities of the respective images along a line perpendicular to the direction of the stripes are sampled. This sampling line is marked with a red arrow in Figure 8. The intensity curves from the ISS, displayed at the top of the figure, are adjusted for pixel drift because each ISS image was taken at a different time and with a different filter. This introduced slight shifts between the image projections, as seen in the mosaic in Figure 2.

The ISS NAC intensity samples reported in Figure 8 show a bright peak around the 400 to 500-pixel mark for every filter. This is the bright diagonal stripe feature from Figure 1. It can be seen that these peaks are slightly offset from each other. In addition, there is a continuous shift to the right for the intensity peaks with increasing wavelength. If it is assumed that this stripe is the same feature observed in every image, then an increase in λ results in the stripes moving to the right along the direction of the sample line.

The VIMS intensity curves for different wavelengths are examined at the bottom of Figure 8. The line samples are obtained using linear interpolation of the pixel values along the line and then processed through a moving average smoothing algorithm to achieve smooth intensity curves despite the limited number of available pixels. Noise in the data is further reduced by sampling the average intensity of spectral bands with a bandwidth of 50 nm (4 VIMS channels) instead of a single wavelength. Starting from the shortest wavelength of 2.81 µm in deep blue, a peak at a sampling line distance of 9 pixels appears. With increasing wavelength, this peak shifts further to the right along the

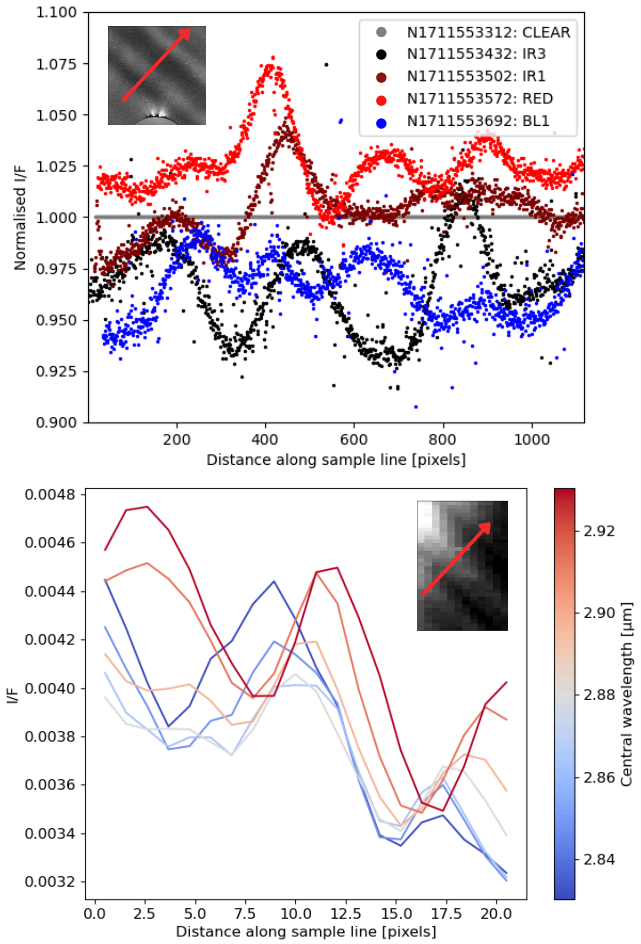

Figure 8: Intenstiy curves of ISS NAC sequence 12 (top) and VIMS cube 1711553290 (bottom) along a sample line indicated by the red arrows. The ISS I/F values are normalised by CLEAR filter images. The VIMS I/F samples are shown for spectral bands with varying central wavelengths and a bandwidth of 50 nm.

sample line and decreases in intensity until 2.88 µm (shown in grey). Increasing the wavelength further, the intensity increases again, and the peak continues to shift towards the right. Extending the analysis to the neighbouring VIMS channels results in the same periodic intensity fluctuations and the continuous shift in stripe spatial position with increasing wavelengths. Additionally, the periodic intensity fluctuations follow a sinusoidal pattern, where the global intensity decreases with increasing wavelength while the amplitude remains constant. The direction of this spatial shift is the same for the ISS and VIMS images.

To conclude, it is shown that the stripes features seen in both VIMS and ISS experience a continuous shift in positions perpendicular to their tilt when observed at different wavelengths. This wavelength-dependent shift is paired with a periodic stripe intensity fluctuation following a sinusoidal pattern.

3.1.2. Retrieval of Spectral Structures on a Flyby Scale

After observing the localised spectral shifts of the stripes, we aim to map these variations across the entire flyby. To achieve such a map, spectral information is extracted from VIMS cubes using the methodology outlined in Figure 9. This method adapts a graphical representation from cell biology known as a kymograph (Nitzsche et al., 2010). Kymographs are space-time plots that depict intensity values along a predefined path over time by trading one spatial dimension for a temporal one. However, this analysis replaces the temporal axis with a spectral dimension.

The process begins by considering a single VIMS cube observed in a specific wavelength channel, as depicted in the top left of Figure 9. In step **A**, the image is rotated so that the VIMS cube stripes align vertically with the observation window. The tilt of the stripes with respect to the image horizontal (samples axis) differs for each flyby. Yet, because of Cassini's varying orientation, they all result in a 16° tilt to the ecliptic when mosaicked in the J2000 reference frame. The rotation angles for vertical stripe alignment in the cubes are 49.8°, 54.2°, and 47.8° for flybys E13, E17, and E19, respectively. In step **B**, the pixels within a single column of the rotated image are averaged, resulting in a single line where the horizontal axis represents the physical dimension of the cube's field of view. The vertical axis now corresponds to a single wavelength. This procedure is repeated across the 256 VIMS-IR channels for the same cube. The resulting lines are then stacked to encompass the full VIMS-IR wavelength range on the vertical axis, as shown in step **C**. The result is a spectral kymograph for a single cube, with the horizontal axis representing the number of pixels (called samples) and the vertical axis representing wavelength. In this kymograph, continuous structures display the gradual displacement of the stripes across different wavelengths. For example, the bright stripe at sample 17, observed in the cube at $\lambda = 3.11$ µm, intensifies as the wavelength increases, while its position remains unchanged along the sample direction. Another stripe can be seen from a high-intensity region starting from $\lambda = 3.11$ µm at sample 24. The bright region gradually shifts to the right with increasing wavelength along the sample direction, indicating a rightward displacement of the stripe.

This methodology can also be extended to an entire flyby mosaic, as illustrated starting from the top right of Figure 9. Initially, the mosaic is rotated, and then the column averages are retrieved for each wavelength channel. These averages are then stacked to generate a spectral kymograph mosaic. However, the horizontal physical dimension now depicts an angular distance projected onto the celestial sphere. Step **D** demonstrates how an individual image cube is integrated within the kymograph mosaic. In practice, the kymograph mosaic is constructed by superimposing each individual cube kymograph onto the next in a manner analogous to the creation of the cube mosaics. The intensity values in each cube kymograph are normalized over the entire flyby, such that an I/F value of 0 corresponds to the global minimum,

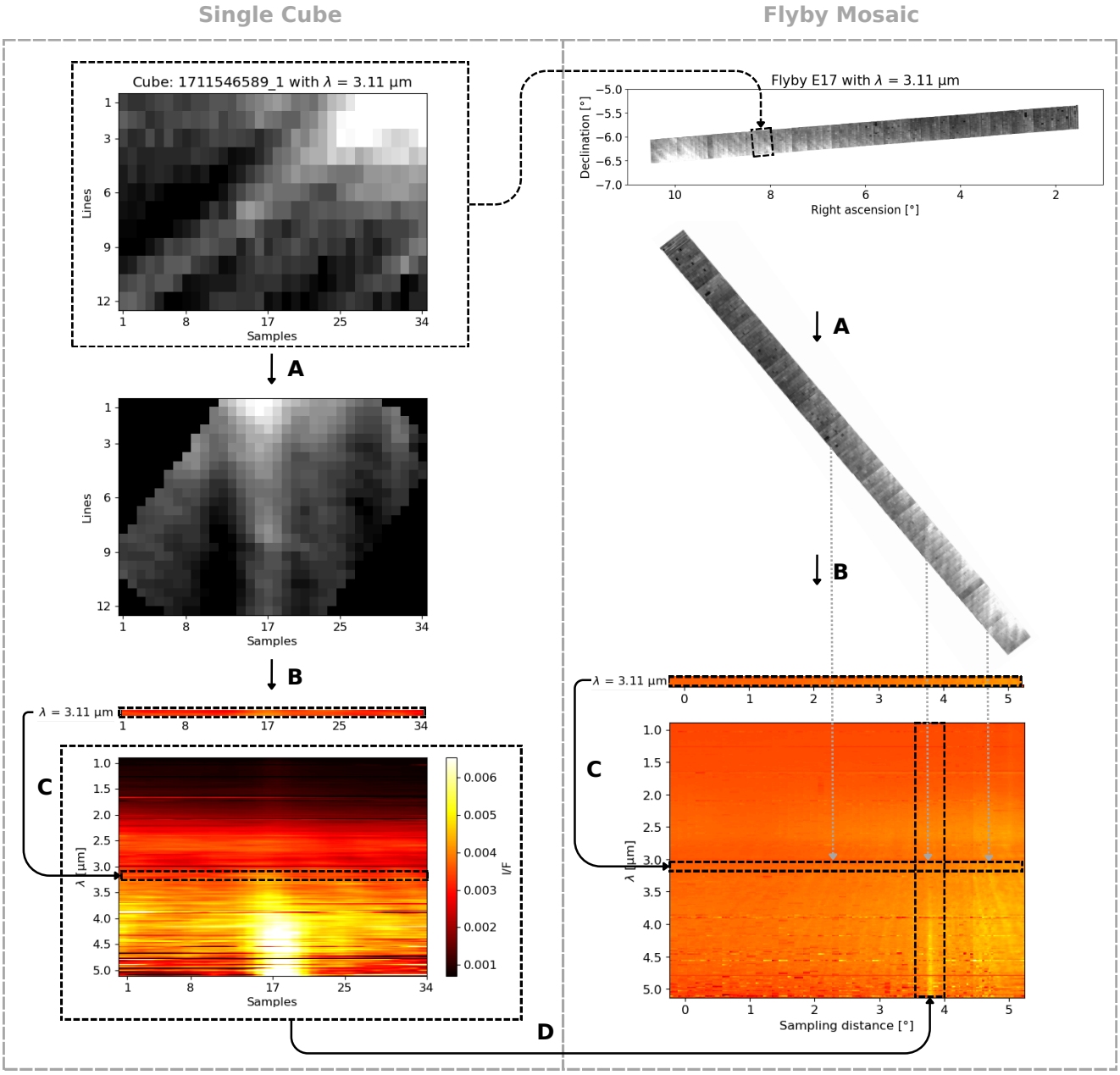

Figure 9: Flow diagram for the creation of a Cassini VIMS flyby spectral kymograph.

and an I/F value of 1 represents the global maximum throughout the flyby.

Figure 10 presents a spectral kymograph mosaic after applying the methodology above on flyby E17. A single vertical bright line can be seen at a sampling distance of 3.85°. This line becomes visible at $\lambda = 3$ µm and gains contrast as λ increases, standing out as the sole bright feature at $\lambda = 5$ µm. The vertical alignment indicates that the feature's position remains constant across all wavelengths. These characteristics correspond to the bright band described in Figure 4. The bright area can also be observed in the kymograph with a global brightness increase after a sampling distance of 4.4°. Other notable features are the multiple slanted lines symmetrically arranged around the bright band. These lines suggest a physical phenomenon where the stripes observed in Figure 4 shift symmetrically and continuously away from the bright band as λ increases.

The spectral shift of the stripes observed in flyby E17 resembles the diffraction of light. Assuming that there is an ideal diffraction grating with plane light waves propagating normal to the grating, the grating intensity I as a function of the diffracting angle θ_d is given by Equation 1 (Thorne, 1988). The first term represents the Fraunhofer diffraction distribution for a single slit with width b. The second term equals the contributions from N slits with equal spacing d.

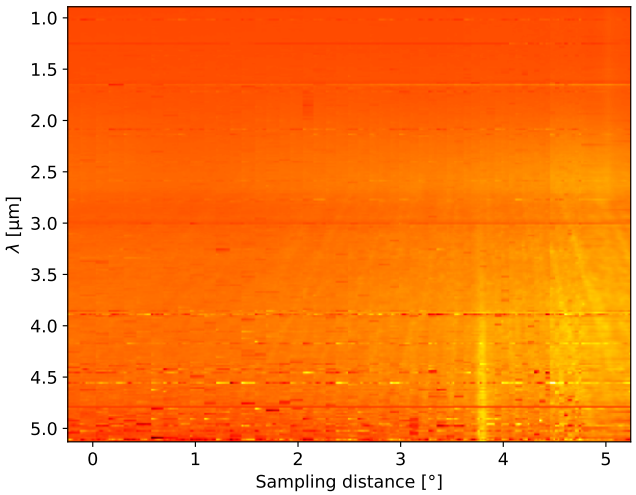

Figure 10: Spectral kymograph mosaic of Cassini flyby E17.

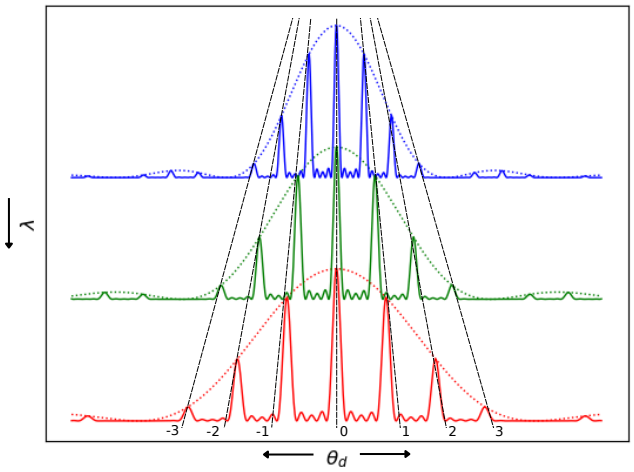

Figure 11: Diffraction pattern from a finite grating with 5 slits and $b = d/4$ in relation to diffraction angle and wavelength similar to the spectral kymograph.

$$I(\theta_d) = \left(\frac{\sin(\beta)}{\beta}\right)^2 \left(\frac{\sin(N\alpha)}{\sin(\alpha)}\right)^2 \text{ where } \beta = \frac{\pi b \sin(\theta_d)}{\lambda}, \quad \alpha = \frac{\pi d \sin(\theta_d)}{\lambda} \tag{1}$$

Figure 11 illustrates the resulting intensity patterns for a grating with five slits for three discrete wavelengths. The diffraction angle is represented on the x-axis, while the wavelength is plotted on the y-axis, similar to the spectral kymographs. The dotted curves show the intensity envelope for a single slit, and the full line curves include the contributions of the five slits. The result is a symmetric diffraction pattern for a given λ, with a 0^{th}-order diffraction peak at $\theta_d = 0$ and higher order peaks emerging from constructive interference at larger $|\theta_d|$. Figure 11, represents a simplified case. In reality, the 0^{th}-order peak cannot be created by forward diffraction from a transmission grating but must be produced by reflection because Cassini observes the bright band at a phase angle of 159° rather than 180°. Therefore, a reflection grating consisting of an orderly-spaced reflecting surface must create the diffraction pattern.

Thorne (1988) proved that the θ_d for a diffraction peak or maxima of integer order m created from a grating with slit spacing d at a particular λ is determined according to the diffraction grating equation shown in Equation 2. θ_i is the incidence angle of the plane wave with respect to the grating normal. For the 0^{th}-order, $\theta_i = -\theta_d$, making it independent of λ. This corresponds to specular reflection in a reflection grating.

$$\sin\theta_i + \sin\theta_d = \frac{m\lambda}{d} \tag{2}$$

Equation 2, can be adapted to get $\sin\theta_d - \sin\theta_0 = \frac{m\lambda}{d}$ which is the angle between the maxima of the m order and the 0^{th}-order. This linear relation between θ_d and λ for a discrete set of m is presented in Figure 11 by the black dashed lines with the orders annotated. These connect the same order peaks for diffraction patterns created by multiple wavelengths but with the same d. The result is a pattern of slanted lines similar to those observed in the spectral kymograph.

In the case of a single slit, represented by the dotted curves in Figure 11, there is a substantial fall intensity for higher-order maxima which conforms to the diffraction hypothesis as the slanted lines in the kymograph are less intense than the bright band. However, orders beyond the third contribute only marginally to the intensity. In contrast, the kymograph shows several distinct lines of roughly equal intensity at various scattering angles. The presence of multiple slits could explain this behaviour. A conservative range of slit widths can be obtained from Equation 2 by assuming that the brightest of both the closest and furthest lines from the bright band are created from a 1^{st}-order diffraction peak. The nearest line is observed at an angular distance of 0.113° from the bright band at $\lambda = 5.11$ µm, resulting in an upper groove spacing limit of 2.60 mm. Identifying the most distant and brightest line from the bright band is challenging due to the similar brightness levels of the lines. In this instance, the stripe crossing the $\lambda = 3$ µm dip at a sampling distance of 2.4° is selected as the most distinguishable. This gives a lower limit for the groove spacing of 0.12 mm. Consequently, the expected groove spacing range for the reflection grating is 0.12–2.6 mm.

Spectral kymographs are also created for the flyby E13 and E19 mosaics. These are shown in Figure 20 and Figure 21 respectively. No vertical or slanted lines can be seen in flyby E13. However, E19 does display at least two distinct slanted lines. No vertical line representing the bright band can be seen in the E19 kymograph, which matches the absence of the bright band in the E19 VIMS mosaic in Figure 17b. From Figure 7, the E19 observations occur at

a location similar to E17 just after crossing Dione's orbit. From Figure 6, it was reported that the bright band is observed in flyby E17 just before this crossing. Therefore, assuming the bright band remains in the same radial distance to Saturn, flyby E19 VIMS observations should occur just after the bright band is observable. The earliest observations in the kymographs are on the left, while the latest are on the right. In Figure 10, kymograph lines to the right of the bright band observation have a negative slope. Since the flyby E19 cubes are assumed to occur after the bright band observation, the kymograph lines for flyby E19 should also have this negative slope. This is true from observing Figure 21.

3.1.3. Localisation of the Stripe Material

The bright band is the origin of the stripes, assuming that these are caused by a distant reflection grating. The apparent location of this bright band can be triangulated with respect to Saturn in 3-dimensional space using multiple cubes. An interactive tool was developed to enhance the visualisation and analysis of the stripe observation geometries using SPICE. Two tool versions were created: one centred on Enceladus and another on Saturn. The Enceladus-centered tool was designed to explore the geometry difference in ISS and VIMS observations in order to link these to potential optical phenomena in Enceladus-targeted flybys. The Saturn-centered version, utilised in this analysis, simulates the observation geometry of Cassini flybys within the Saturn system while also allowing for the simultaneous projection of the observed VIMS cubes along the line of sight. Both tools are detailed in the appendix, and the source code is available at nrubbrecht/thesis_tools_pub.git.

Five VIMS cubes contain the bright band in their field of view. In Figure 4, it is shown that these cubes create a continuous mosaic showing a single bright line when projected in RA and DEC space. In addition, the fixed positions of the stripes in the mosaic suggest that the bright band appears stationary in the J2000 reference frame. These observations could indicate that the medium producing these diffraction patterns can be localised by finding the origin of the pattern. From this assumption, two edge observations of the bright band can be used to triangulate its location. In this case, the cubes are projected at varying distances from Cassini along the line of sight until the bright band aligns between both images.

The bright band's start and end observation geometries were retrieved using the SPICE tool. These include the VIMS cubes 1711545954_1 and 1711547227_1. The result is shown in Figure 12. The orbits of Saturn's mid-sized inner moons are shown here with annotated dashed lines. Cassini's positions during the observation times of both cubes are shown with an open and full diamond, respectively. Similarly, the positions of Enceladus are shown with an open and solid grey dot. The VIMS field of view during both observation times is shown in cyan. The projected fields of view showed that large distances beyond Saturn's inner-mid-sized moon orbits are necessary for the stripes in the two cubes to align/coincide. No alignment of the stripes in

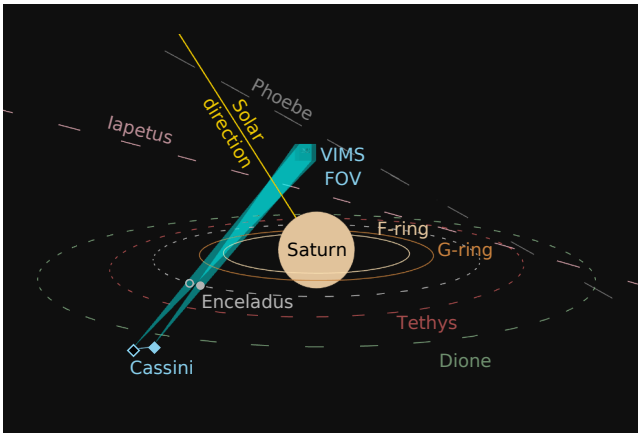

Figure 12: 3-Dimensional view of Cassini's flyby E17 observation geometry for two VIMS bright band observations from the SPICE tool.

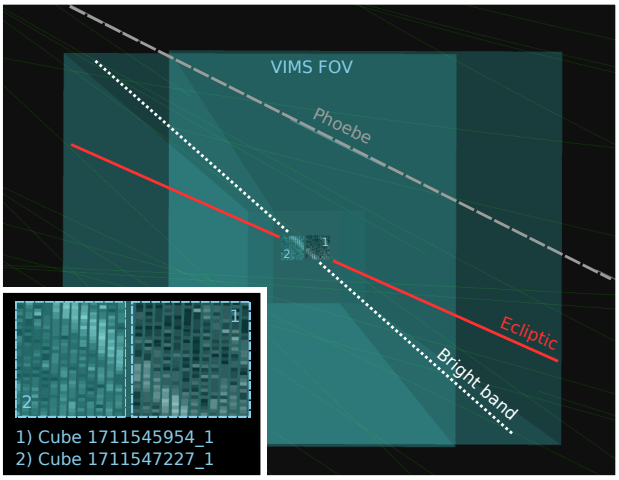

Figure 13: VIMS view showing the bright band observations for two VIMS cubes during Cassini's flyby E17 from the SPICE tool.

both cubes could be observed until increasing the projecting distance near Phoebe's orbit. It was found that the alignment could be achieved starting from a distance of approximately 180 R_S; from there, the distance could be increased to infinity and result in perfect alignment. In comparison, Phoebe's elliptical orbit ($e = 0.16$) has a semi-major axis $a = 215$ R_S (Desmars et al., 2013). This alignment behaviour is consistent with the bright bands' continuity in the RA/DEC mosaic, which assumes a projection at an infinite distance.

The alignment between the bright band in cubes 171154 5954_1 and 171154722_1 can be seen in Figure 13, which shows a VIMS-centred field of view at the orbital distance of Phoebe. A zoomed-in version of the projections of the VIMS cubes is shown on the lower left. The dashed grey line presents the phoebe orbit, which is located ~ 9.7 R_S above the observed bright band. The orientation of the ecliptic (shown in red) can be compared to the orientation of the extended bright band (dotted white line) and the Phoebe orbit.

The orbital plane of Phoebe is tilted 5.3° relative to the J2000 Ecliptic; however, the orbital inclination of the moon is 174.7° due to its rotation in the opposite direction of the inner satellites of Saturn (Gladman et al., 2001). From Figure 4, it was noted that the bright band appears to be inclined 16° from the ecliptic. Therefore, the inclination becomes 164° if we assume a phoebe-like retrograde orbit. Note that the inclinations of the bright band and Phoebe's orbit seen in Figure 4 and Figure 13 are not necessarily the true inclinations in the J2000 frame but are apparent inclinations projected onto the J2000 reference frame from Cassini's position. Nevertheless, it can be seen that Phoebe's orbit is inclined about 11° compared to the bright band.

Verbiscer et al. (2009) found a large diffuse ring centred around Phoebe's orbit, conventionally called the Phoebe ring. This ring has a radial extent of at least 128–207 R_S and a vertical thickness of 40 R_S. The ring subtends 10° in the sky from Cassini's position in flyby E17. Therefore, the Phoebe ring would be seen as a constant background of scattered light encompassing the entire field of view of the VIMS and ISS observations (Tamayo et al., 2014). Thus, the Phoebe ring cannot be the bright band Cassini observed in flyby E17.

Phoebe is part of a larger group of retrograde irregular satellites orbiting around Saturn (Denk et al., 2018). Other moons in this retrograde group (also called the Norse group) are much smaller than phoebe (213 km diameter) in the order of ∼40 to 4 km in diameter but can achieve very similar inclinations to the bright band ranging between $i = 145$–$180°$. The orbits of the Norse group satellites are shown by the thin green lines in the background of Figure 13. The combination of the required distance for alignment of the bright band and the similar inclination makes the retrograde orbits of these irregular moons a good candidate for the origin of the bright band.

An overview of the VIMS viewing geometry for flyby E13 and E19 is given in Figure 22. Flyby E19 has a similar viewing geometry to E17, below and to the left of the phoebe orbit. Although the bright band is absent in flyby E19, its location can be triangulated from the spectral kymograph in Figure 21. This is done using the assumption that the slanted lines are caused by diffraction and that the intersections of the lines at $\lambda = 0$ reveal the location of the 0^{th}-order diffraction, which is the bright band. In this case, the bright band would appear in the RA range of 8.5 to 9° in the flyby mosaic of Figure 17b if the imaging sequence was extended to earlier observation times. However, in flyby E19, a minimum distance of 400 R_S is required before the stripes align, nearly double the semi-major axis of Phoebe's orbit. Yet, retrograde orbits of irregular Saturnian moons still exist at this distance (Denk et al., 2018).

From the top of Figure 22, Cassini is observing the sky slightly to the right of the Phoebe orbit during flyby E13. No 0^{th}-order is observed in this flyby and no stripes are present in the kymograph. Therefore, the bright band cannot be localised for these observations. Nevertheless, the higher-order stripes have the same apparent inclination of 16° and minimum distance requirement of $180R_S$ for alignment similar to flyby E17. From these observations, it can be concluded that the possibility of the bright band existing in a Norse group orbit remains.

3.2. Characterisation of the Material at the Origin of the Stripes

To investigate the nature of the particles that create the bright band, VIMS-IR spectra can be retrieved and compared to other features like the plumes and the E-ring background. Noise is prominent for high-phase observations of faint structures like the plumes (Hedman et al., 2009b). Therefore, spectra of five cubes containing the bright band were averaged to extract meaningful spectra. Details regarding these observations are shown in Table 3.

Table 3
Cubes containing the bright band.

Cube ID	Cube Mid-Time [UTC]	Range [km]	Phase [°]
1711545954_1	2012-03-27 12:36:53	201,832	158.6
1711546301_1	2012-03-27 12:42:40	197,424	158.8
1711546589_1	2012-03-27 12:47:28	193,813	158.9
1711546939_1	2012-03-27 12:53:18	189,440	159.0
1711547227_1	2012-03-27 12:58:06	185,890	159.1

An example of the spectra retrieval inspired by the analysis of Dhingra et al. (2017) is illustrated in the left part of Figure 14. The bright band spectrum is extracted by averaging pixels along a line (shown in red) using spline interpolation on the pixels values in the line's vicinity. The bottom figure shows that the line does not extend the entire length of the bright band. This is because pixels in the bright band that correspond to the plumes or body of Enceladus are ignored. This is to prevent other contributions to the bright band spectra. Next, the spectra of the plumes are extracted by averaging the pixel intensities over the area shown in green. Similarly, the E-ring background is determined by averaging the pixel values in blue. The process is repeated for each of the five cubes containing the bright band. Note that in each image, the bright band is in a different location, therefore, the line samples are adjusted for each image. Sample locations for the plumes and the E-ring background remain the same, as justified by the similar observation geometries. A measure for the noise in the cubes is obtained by computing the standard deviation of the pixels used to calculate the E-ring background measurements similar to the method of Dhingra et al. (2017). Additionally, data from known hot channels (1.24 µm, 1.33 µm, 3.23 µm, 3.24 µm, 3.83 µm) and from IR focal plane blocking filters (1.6–1.67 µm, 2.94–3.01 µm, and 3.83–3.89 µm) is excluded in this analysis (Brown et al., 2004; Nicholson et al., 2008). The wavelength uncertainty for VIMS-IR channels is less than 10 nm (Dhingra et al., 2017).

Distinct differences between the plume, the bright band, and the E-ring background appear from the averaged spectra on the right of Figure 14. These are analysed through indicators inspired by the analysis of Dhingra et al. (2016).

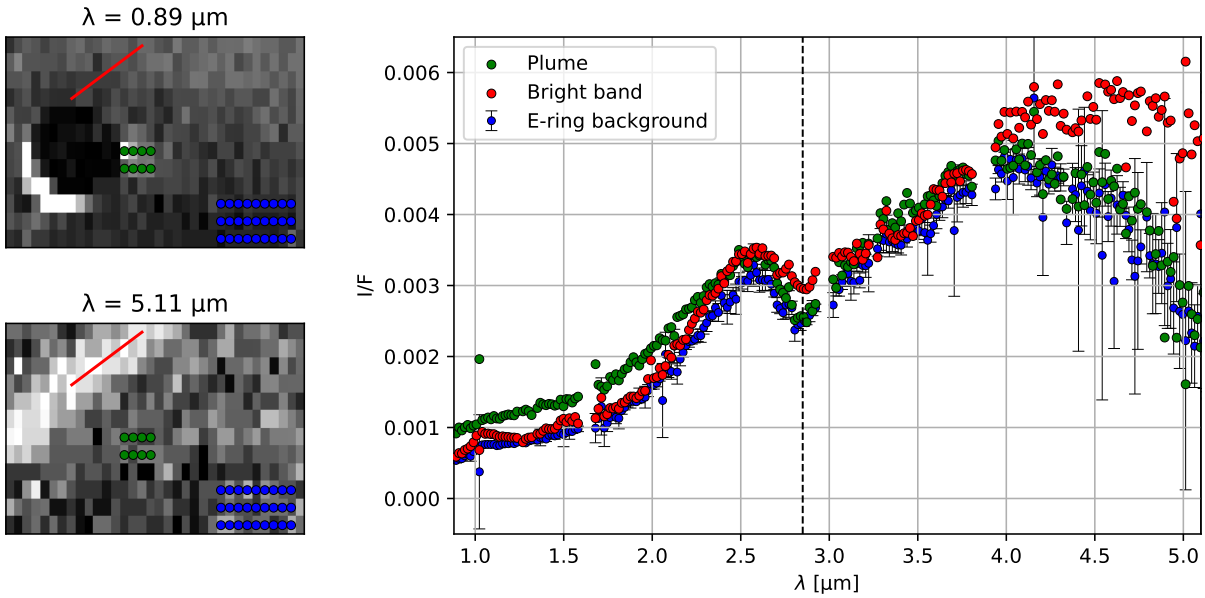

Figure 14: (left) Example of sampling areas of VIMS cube 1711547227_1, (right) spectra averaged over all bright band observations. The dashed line indicates the position of 2.85 µm for comparison.

(A) 1–2 µm & 2–2.6 µm Spectral Slopes: The bright band spectrum is similar to the E-ring background for $\lambda <$ 2 µm aside from two smooth peaks centred around 1 and 1.6 microns. The plume is generally brighter in this spectral range with a similar spectral slope as the bright band and the E-ring. In the spectral range of 2–2.6 µm, the bright band spectrum has a steeper slope than the plume and E-ring spectra. Because the wavelength range of the observations is related to the particle sizes in the scene, the spectrum of the bright band suggests a particle size distribution with a higher percentage of larger particles compared to the plumes and E-ring background (Hedman et al., 2009b; Dhingra et al., 2016).

(B) 3 µm Water-Ice Band Position: The position of the band minimum of the 3-micron water absorption band is identical for the plumes and the bright band, which is just to the right of the 2.85 µm mark shown by the dashed vertical line. The E-ring background spectrum has a minimum below 2.85 µm. Mastrapa et al. (2008) showed experimentally that the position of the band minimum can be used to distinguish amorphous and crystalline water ice. As the ice transitions from amorphous to crystalline, the band minimum shifts approximately 50 nm towards longer wavelengths. Therefore, the plume consists of mainly crystalline ice, which agrees with the results from Dhingra et al. (2017). The bright band has the same crystallinity, while the E-ring contains more amorphous ice.

(C) 3 µm Water-Ice Band Shape: The shape of the 3-micron water absorption band is similar for the plume and the E-ring background. However, the absorption feature is less steep and narrow for the bright band, with an added bump close to 3 µm. Dhingra et al. (2017) found that the 3-micron water absorption band shape strongly depends on particle size distributions. This bright band spectrum could be the result of a paucity of particles with a radius smaller than 2 µm. The plume spectrum shows the greatest band depth, followed by the E-ring and the bright band. This indicates that water ice is most abundant in the plume and least abundant in the bright band's material.

(D) > 4 µm Spectral Slope & CO_2 Absorption: The signal-to-noise ratio is low in the spectral region of $\lambda > 4$ µm as shown by the large error bars, yet some features can still be discerned. The bright band spectrum is significantly brighter than the plume and E-ring background, which was also observed directly from the cubes in this spectral range. This again suggests that larger particles are present in the bright band's material compared to the material in the plumes and E-ring. In addition, there is a dip in the bright band spectrum at around 4.27–4.42 µm, which can be associated with the absorption of solid phase CO_2 (Postberg et al., 2018). This absorption band is not seen in the other spectra.

In conclusion, the spectrum of the bright band suggests the presence of water ice that is as crystalline as the particles in Enceladus' plumes, though it contains less water than the plumes and E-ring. The particle size distribution in the bright band likely includes a higher proportion of larger particles than the plumes and E-ring, with fewer grains smaller than 2 µm. Additionally, CO_2 is thought to be present in the bright band material. The presence of large particles and CO_2 suggests that the material in the bright band may be very fresh, potentially shielded from radiation and thus less affected by space-weathering effects (Nölle et al., 2023).

4. Interpretation & Discussion

We summarise the observation of stripe observations in flybys E13, E17, and E19. Flyby E17 revealed stripes in concurrent VIMS-IR and ISS measurements, while the other flybys only included VIMS-IR observations. These high-phase observations show continuous stripes between images when projected at an infinite distance in the J2000 reference frame using RA-DEC coordinates. The stripes are all parallel and have an apparent inclination of ∼16° to the ecliptic and 43° to Saturn's ring plane. The stripes may also appear brighter than Enceladus and positioned in front of the moon. Interestingly, under the same observation geometry, stripes found in VIMS-IR do not always correspond to stripes in the ISS NAC. A combination of phase angle dependence, where stripes are visible only at phase angles greater than 160°, and decreased stripe visibility at wavelengths below 2.2 µm (as observed in VIMS flybys E13, E17, and E19) could be the cause of this.

A single bright line observed by VIMS-IR during flyby E17 lies at the centre of these stripe observations. This bright band becomes visible at $\lambda > 3$ µm and increases in contrast up until $\lambda = 5.11$ µm. The width of this bright band is approximately 1 to 1.5 mrad, which is similar to the apparent width of the Sun as observed by Cassini. It was found that this feature acts as a reflection grating where the bright band itself is observed as reflected light, while the other stripes in the flyby are likely created from higher-order diffraction peaks. The estimated groove spacing of the grating should be 0.12 to 2.60 mm according to the diffraction effects seen in Figure 10 and Figure 21.

The stripes appear continuous between images when projected at distances near or beyond Phoebe's orbit, specifically at orbital distances greater than $400 R_S$ from Saturn.

The spectrum of the bright band's material suggests that it consists primarily of crystalline water ice. The particle size distribution likely contains larger particles than the plume and E-ring background or a lack of particles with a radius smaller than 2 µm. Additionally, a trace of solid phase CO_2 was identified in the bright band's material, which was not seen in the other spectra. These findings suggest that the material could be fresh and potentially shielded from radiation.

These observations led to formulating two distinct hypotheses visually depicted in Figure 15. Their agreement with the observations is summarised in Table 4 and discussed below.

Hypothesis 1: *A millimetre-sized ordered structure within the Norse group.* This hypothesis is formulated around two key observational constraints. First, the minimum orbital distances from the triangulation of the VIMS cubes place the stripe phenomenon within the realm of Saturn's distant irregular moons (Gladman et al., 2001). Second, the observed inclination of the stripes (164°, retrograde to Saturn) aligns exclusively with the orbits of the Norse group moons among Saturn's known orbiting bodies (145–180°) (Denk et al., 2018). Additionally, the observed relative motion between Enceladus and the stripes is similar to the simulated relative movement from SPICE when the bright band is placed near Phoebe's orbit. Consequently, several rings or arcs near Phoebe and the Norse group, spaced millimetres apart, could generate aligned stripes with inclinations matching their orbits. Although proposed materials like crystalline water ice and CO_2 cannot be directly attributed to the Norse group and Phoebe ring, Hansen et al. (2012) detected traces of crystalline water ice and CO_2 on Phoebe's surface, which is the primary source of the Phoebe ring particles. However, this material comprises only a few per cent water ice, with the remainder being non-water ice constituents. In comparison, the E-ring material consists of +90% pure water ice (Postberg et al., 2018). Based on Figure 14, the bright band composition appears more similar to the region near Enceladus, although the composition of Phoebe's ring environment remains poorly constrained.

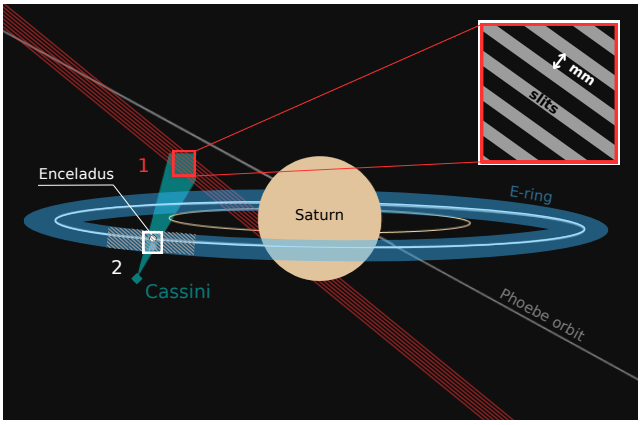

Figure 15: Visualisation of both hypotheses for the observed stripe features, with a reflection grating located either at the Norse group orbits (Hypothesis 1) or at the E-ring (Hypothesis 2). A zoomed-in view for both scenarios is shown in the top right corner.

Notably, there are observations that this hypothesis cannot explain at this state of the research. First, the bright band and higher-order stripes can appear brighter than Enceladus for $\lambda > 3$ µm. From Cassini's perspective during the bright band observations, an object in Phoebe's orbit must be around 5,500 times brighter than Enceladus (based on the inverse square law of brightness) to appear as bright as Enceladus. This scenario is highly improbable, especially considering that the Phoebe ring is extremely faint ($I/F \approx 10^{-9}$ at $\lambda = 0.635$ µm from Tamayo et al. (2016)). Another concern with this first hypothesis is that the stripes appear in front of Enceladus. If the material at the origin of these stripes is located beyond Phoebe's orbit, it is difficult to explain why the stripes are appearing in front of Enceladus. Lastly, no known periodic structures exist in the Norse group or seemingly randomly distributed Phoebe ring (Verbiscer et al., 2009; Tamayo et al., 2014; Hamilton et al., 2015).

Hypothesis 2*: A millimetre-sized inclined ordered structure within the E-ring.* In this scenario, the stripes are produced by an organized structure positioned between Cassini and Enceladus. For flybys E17 and E19, this structure lies

Table 4
Agreement of stripe observations with hypotheses (✓ = agree, – = neutral, X = disagree).

Observation	Hypothesis 1: Norse Group	Hypothesis 2: E-ring
Stripe brightness	X	✓
Stripe width	– , no direct correlation	– , no direct correlation
In front of Enceladus	X	✓
Stripe Tilt	✓ , ∼ 164° retrograde orbit inclination	– , if inclined ∼ 43° to Saturn's ring plane
Triangulation	✓	X
Movement to Enceladus	✓ , parallax	– , not fully understood
A periodic structure	X	– , sinusoidal E-ring tendrils
Crystalline water ice	– , water-poor, structure unknown	✓ , water-rich, crystalline fresh plume material
CO_2	– , only found on Phoebe's surface	✓ , fresh plume material

specifically between the orbits of Enceladus and Rhea, and for E13, between the G-ring and Enceladus' orbit. This range of radial distances from Saturn spans the E-ring's inner and outer regions. This hypothesis aims to provide the most convenient explanation for why the stripes can appear in front of Enceladus while also being significantly brighter at longer wavelengths. If the light-scattering object is closer to Cassini than Enceladus, it can naturally appear brighter. Additionally, for the stripes to appear in front of Enceladus, they must be produced by particles located physically in front of the moon.

The bright band's spectrum suggested the presence of crystalline water-ice and CO_2 that resembles fresh plume material. Dhingra et al. (2017) and the analysis in subsection 3.2 show that the plumes consist mainly of crystalline water ice while Brown et al. (2006) and Combe et al. (2019) detected CO_2 trapped in ice on the surface of Enceladus near the Tiger Stripes. However, the spectra of the plume and bright band's material in Figure 14 remain different, leaving questions about the connection between the bright band's material and the fresh plume material. If the bright band's material is similar to fresh plume material, the plume spectrum would be expected to exhibit the CO_2 absorption feature as well. However, the plume's signal is noisier compared to the bright band at these wavelengths (as shown on the bottom left in Figure 14), which may obscure the CO_2 absorption in the plume spectrum. From subsection 3.2, we noted that spectral differences could be attributed to particle size distributions favouring larger particles in the bright band compared to the E-ring and the plume. Fresh E-ring particles supplied by the plumes are generally larger than the older particles in the E-ring due to space-weathering effects, such as sputtering (Nölle et al., 2023). Also, space-weathering leads to a decrease in more volatile compounds in the ice, such as CO_2 and can transform crystalline ice to amorphous ice (Dartois et al., 2015). As a result, comparing the spectra in Figure 14 to "fresh" particles for the bright band's material and to "older" E-ring particles for the E-ring background aligns with what is expected from the literature.

Difficulties in supporting this hypothesis arise from the bright band's inclination of 43° to Saturn's ring plane. Kempf et al. (2010); Hedman et al. (2011) observed that E-ring particles launched from Enceladus' plumes can achieve orbital inclinations up to 1°, nowhere near the required inclination of the stripes. Ice crystals may become preferentially oriented with the electric field generated by Saturn's magnetosphere (Saunders and Rimmer, 1999; Jones et al., 2006), potentially creating the necessary inclination. This alignment can also lead to the formation of unusual halo displays (Moilanen and Gritsevich, 2022). However, the intricate interactions between the plumes of Enceladus and Saturn's magnetosphere, along with the uncertainty surrounding the shapes of the plume ice crystals, complicate predictions regarding halo phenomena and crystal orientations.

Mitchell et al. (2015) found sinusoidal structures within the E-ring near Enceladus called 'tendrils'. These tendrils originate from the highest velocity particles ejected from the plumes and follow Horseshoe orbits from Enceladus' leading and trailing edge. These horseshoe orbits' looping motion could potentially produce the necessary inclination and periodic structure for the stripe features. Simulations from Weiss et al. (2013) concluded that for particles smaller than ∼1 micron, the influence of Saturn's magnetic field blurs out the tendrils while larger particles ∼3 microns create distinct tendrils. This preference for larger particles aligns with the spectra shown in Figure 14.

Another much smaller source of particles in the E-ring comes from the impacts of existing E-ring particles on the inner mid-sized moons (Dobrovolskis et al., 2010). These impacts eject fresh surface material to the E-ring. Kempf et al. (2008) simulated orbits from these impact ejecta and found low inclinations up to 1° similar to those originating from the plumes. Other material, such as that from Saturn's inner rings, is also unlikely to produce high inclinations since it remains confined to Saturn's ring plane. The close alignment of the stripes with the ecliptic could hint towards a source beyond Saturn's Hill sphere, like interplanetary dust or cometary debris. However, such contributions are relatively small compared to material generated within Saturn's system (Hsu et al., 2011).

Another issue in supporting this hypothesis is the apparent misalignment of the stripes when projected at radial distances smaller than 180 R_S, as discussed in section 3. The previous triangulation assumed that the bright band's position remained fixed in the Saturnian system during flyby E17. Under this assumption, the bright band cannot be

located within the bounds of the E-ring. Consequently, in this hypothesis, the bright band must be moving, which renders the triangulation approach ineffective. This raises the question of how the stripe features can appear stationary in the RA/DEC mosaics. A possible explanation involves the interaction between the apparent movement of the features in Cassini's line-of-sight and the reflection of light, but this mechanism is not yet fully understood.

5. Conclusions

In this article, we report the observation of stripe features simultaneously captured by Cassini's ISS and VIMS-IR instruments during the Enceladus-targeted flyby E17. The stripes appear continuous across successive images when mosaicked at an infinite distance and are consistent between both instruments, suggesting an external origin. Similar patterns were also observed in VIMS-IR data from flybys E13 and E19. A central bright band, most prominent at a wavelength of ∼5 microns, is believed to result from reflected light, with the additional stripes forming as higher-order diffraction peaks, much like a reflection grating.

Two hypotheses are proposed to explain this phenomenon. The first suggests an ordered structure within the orbits of Saturn's Norse group moons, acting as a reflection grating, with alignment and inclination provided by the orbits of these moons. However, questions remain about the brightness and position of the stripes relative to Enceladus, given the small size and expected dimness of these distant moons. The second hypothesis proposes an ordered structure within the E-ring, which could explain the brighter stripes appearing in front of Enceladus. This hypothesis, however, faces challenges due to the high inclination of the observed stripes, which is unusual for orbits close to Saturn. Both hypotheses rely on the presence of millimetre-scale periodic structures capable of producing a reflection grating effect.

Recommendations for future research include filtering the VIMS cube to enhance the stripe contrast and reduce noise. This will aid in producing clearer spectral kymographs and deconstructing the contributions of the groove spacings and widths of the reflection grating.

A specific configuration should be identified where the stripes remain continuous when projected at an infinite distance while physically situated between Cassini and Enceladus. This could be explored through ray tracing software or by setting up an experimental model replicating the scene's motions and illumination.

Further, fitting the VIMS spectra of the bright band to particle size distributions using Mie theory, as done by Hedman et al. (2009a), is recommended. A similar comparison with different ice mixtures could provide additional insights.

A survey of ISS and VIMS-IR data was conducted to find stripe features similar to those observed during flybys E13, E17, and E19. Expanding this survey to include VIMS-IR non-targeted flybys at high phase angles, primarily when Cassini is located between the G-ring and Rhea's orbit, is advised. Investigating other instruments with similar near-infrared sensitivity and observation geometries would also be valuable.

References

C. H. Acton, 1996. Ancillary data services of NASA's Navigation and Ancillary Information Facility. Technical Report 1. Jet Propulsion Laboratory, California Institute of Technology.

R. H. Brown, K. H. Baines, G. Bellucci et al., 2004. The Cassini Visual And Infrared Mapping Spectrometer (Vims) Investigation. Space Science Reviews 115, 111–168. URL: https://doi.org/10.1007/s11214-004-1453-x, doi:10.1007/s11214-004-1453-x.

R. H. Brown, R. N. Clark, B. J. Buratti et al., 2006. Composition and physical properties of Enceladus' surface. Science 311, 1425–1428. doi:10.1126/science.1121031.

C. E. Carr, M. T. Zuber and G. Ruvkun, 2013. Life detection with the Enceladus Orbiting Sequencer, in: IEEE Aerospace Conference Proceedings. doi:10.1109/AERO.2013.6497129.

G. Choblet, G. Tobie, A. Buch et al., 2022. Enceladus as a potential oasis for life: Science goals and investigations for future explorations. Experimental Astronomy 54, 809–847. URL: https://doi.org/10.1007/s10686-021-09808-7, doi:10.1007/s10686-021-09808-7.

J.-P. Combe, T. B. McCord, D. L. Matson et al., 2019. Nature, distribution and origin of CO2 on Enceladus. Icarus 317, 491–508. URL: https://www.sciencedirect.com/science/article/pii/S001910351730667X, doi:https://doi.org/10.1016/j.icarus.2018.08.007.

E. Dartois, B. Augé, P. Boduch et al., 2015. Heavy ion irradiation of crystalline water ice: Cosmic ray amorphisation cross-section and sputtering yield. Astronomy and Astrophysics 576. doi:10.1051/0004-6361/201425415.

T. Denk, S. Mottola, F. Tosi et al., 2018. The irregular satellites of Saturn. Enceladus and the Icy Moons of Saturn , 409.

K. E. Denny, M. M. Hedman, D. Bockelée-Morvan et al., 2024. Constraining Time Variations in Enceladus's Water-vapor Plume with Near-infrared Spectra from Cassini's Visual and Infrared Mapping Spectrometer. Planetary Science Journal 5. doi:10.3847/PSJ/ad4c69.

J. Desmars, S. N. Li, R. Tajeddine et al., 2013. Phoebe's orbit from ground-based and space-based observations. Astronomy & Astrophysics 553, A36. doi:10.1051/0004-6361/201321114.

D. Dhingra, M. M. Hedman and R. N. Clark, 2016. Near Infrared Spectral Systematics of Enceladus' Plume: Links to Formation Conditions and Dominant Controls, in: 47th Annual Lunar and Planetary Science Conference, p. 2638.

D. Dhingra, M. M. Hedman, R. N. Clark et al., 2017. Spatially resolved near infrared observations of Enceladus' tiger stripe eruptions from Cassini VIMS. Icarus 292, 1–12. doi:10.1016/j.icarus.2017.03.002.

A. R. Dobrovolskis, J. L. Alvarellos, K. J. Zahnle et al., 2010. Exchange of ejecta between Telesto and Calypso: Tadpoles, horseshoes, and passing orbits. Icarus 210, 436–445. doi:10.1016/j.icarus.2010.06.023.

F. Favata, G. Hasinger, L. J. Tacconi et al., 2021. Introducing the Voyage 2050 White Papers, contributions from the science community to ESA's long-term plan for the Scientific Programme. doi:10.1007/s10686-021-09746-4.

B. Gladman, J. J. Kavelaars, M. Holman et al., 2001. Discovery of 12 satellites of Saturn exhibiting orbital clustering. Nature 412, 163–166. URL: https://doi.org/10.1038/35084032, doi:10.1038/35084032.

D. P. Hamilton, M. F. Skrutskie, A. J. Verbiscer et al., 2015. Small particles dominate Saturn's Phoebe ring to surprisingly large distances. Nature 522, 185–187. doi:10.1038/nature14476.

G. B. Hansen, E. C. Hollenbeck, K. Stephan et al., 2012. Water ice abundance and CO 2 band strength on the saturnian satellite Phoebe from Cassini/VIMS observations. Icarus 220, 331–338. doi:10.1016/j.icarus.2012.05.004.

M. M. Hedman, J. A. Burns, D. P. Hamilton et al., 2011. The three-dimensional structure of Saturn's E ring URL: http://arxiv.org/abs/1111.2568http://dx.doi.org/10.1016/j.icarus.2011.11.006, doi:10.1016/j.icarus.2011.11.006.

M. M. Hedman, C. D. Murray, N. J. Cooper et al., 2009a. Three tenuous rings/arcs for three tiny moons. Icarus 199, 378–386. doi:10.1016/j.icarus.2008.11.001.

M. M. Hedman, P. D. Nicholson, M. R. Showalter et al., 2009b. Spectral observations of the enceladus plume with cassini-vims. Astrophysical Journal 693, 1749–1762. doi:10.1088/0004-637X/693/2/1749.

H. W. Hsu, F. Postberg, S. Kempf et al., 2011. Stream particles as the probe of the dust-plasma-magnetosphere interaction at Saturn. Journal of Geophysical Research: Space Physics 116. doi:10.1029/2011JA016488.

A. P. Ingersoll and S. P. Ewald, 2011. Total particulate mass in Enceladus plumes and mass of Saturn's E ring inferred from Cassini ISS images. Icarus 216, 492–506. doi:10.1016/j.icarus.2011.09.018.

A. P. Ingersoll, S. P. Ewald and S. K. Trumbo, 2020. Time variability of the Enceladus plumes: Orbital periods, decadal periods, and aperiodic change. Icarus 344. doi:10.1016/j.icarus.2019.06.006.

G. H. Jones, E. Roussos, N. Krupp et al., 2006. Enceladus' varying imprint on the magnetosphere of Saturn. Science 311, 1412–1415. doi:10.1126/science.1121011.

S. Kempf, U. Beckmann, G. Moragas-Klostermeyer et al., 2008. The E ring in the vicinity of Enceladus. I. Spatial distribution and properties of the ring particles. Icarus 193, 420–437. doi:10.1016/j.icarus.2007.06.027.

S. Kempf, U. Beckmann and J. Schmidt, 2010. How the Enceladus dust plume feeds Saturn's E ring. Icarus 206, 446–457. doi:10.1016/j.icarus.2009.09.016.

B. Knowles, 2018. Cassini imaging science Subsystem (ISS) data User's Guide. PDS https://pds-rings. seti. org/cassini .

J. Laura, A. Acosta, T. Addair et al., 2023. Integrated Software for Imagers and Spectrometers. URL: https://doi.org/10.5281/zenodo.7644616, doi:10.5281/zenodo.7644616.

P. Laven, 2004. Simulation of rainbows, coronas and glories using Mie theory and the Debye series. Journal of Quantitative Spectroscopy and Radiative Transfer 89, 257–269. doi:10.1016/j.jqsrt.2004.05.026.

S. Le Mouélic, T. Cornet, S. Rodriguez et al., 2019. The Cassini VIMS archive of Titan: From browse products to global infrared color maps. Icarus 319, 121–132. doi:10.1016/j.icarus.2018.09.017.

M. T. Lemmon, D. Toledo, V. Apestigue et al., 2022. Hexagonal Prisms Form in Water-Ice Clouds on Mars, Producing Halo Displays Seen by Perseverance Rover. Geophysical Research Letters 49. doi:10.1029/2022GL099776.

D. K. Lynch and P. Schwartz, 1991. Rainbows and fogbows. Technical Report.

W. J. Markiewicz, E. Petrova, O. Shalygina et al., 2014. Glory on Venus cloud tops and the unknown UV absorber. Icarus 234, 200–203. doi:10.1016/J.ICARUS.2014.01.030.

R. M. Mastrapa, M. P. Bernstein, S. A. Sandford et al., 2008. Optical constants of amorphous and crystalline H2O-ice in the near infrared from 1.1 to 2.6 μm. Icarus 197, 307–320. doi:10.1016/j.icarus.2008.04.008.

C. J. Mitchell, C. C. Porco and J. W. Weiss, 2015. Tracking the geysers of enceladus into saturn's e ring. Astronomical Journal 149. doi:10.1088/0004-6256/149/5/156.

J. Moilanen and M. Gritsevich, 2022. Light scattering by airborne ice crystals – An inventory of atmospheric halos. Journal of Quantitative Spectroscopy and Radiative Transfer 290. doi:10.1016/j.jqsrt.2022.108313.

C. Morello and M. J. Berg, 2024. A light scattering analysis of the cryovolcano plumes on enceladus. Journal of Quantitative Spectroscopy and Radiative Transfer 322. doi:10.1016/j.jqsrt.2024.109018.

P. D. Nicholson, M. M. Hedman, R. N. Clark et al., 2008. A close look at Saturn's rings with Cassini VIMS. Icarus 193, 182–212. doi:10.1016/j.icarus.2007.08.036.

B. Nitzsche, V. Bormuth, C. Bräuer et al., 2010. Chapter 14 - Studying Kinesin Motors by Optical 3D-Nanometry in Gliding Motility Assays, in: L. Wilson and J. J. Correia (Eds.), Microtubules, in vitro. Academic Press. volume 95 of *Methods in Cell Biology*, pp. 247–271. URL: https://www.sciencedirect.com/science/article/pii/S0091679X10950140, doi:https://doi.org/10.1016/S0091-679X(10)95014-0.

L. Nölle, F. Postberg, J. Schmidt et al., 2023. Radial compositional profile of Saturn's E ring indicates substantial space weathering effects. Monthly Notices of the Royal Astronomical Society 527, 8131–8139. doi:10.1093/mnras/stad3621.

H. M. Nussenzveig, 2012. THE SCIENCE OF THE GLORY. Scientific American 306, 68–73. URL: http://www.jstor.org.tudelft.idm.oclc.org/stable/26014160.

R. S. Park, N. Mastrodemos, R. A. Jacobson et al., 2024. The Global Shape, Gravity Field, and Libration of Enceladus. Journal of Geophysical Research: Planets 129. doi:10.1029/2023JE008054.

E. V. Petrova, O. S. Shalygina and W. J. Markiewicz, 2015. The VMC/VEx photometry at small phase angles: Glory and the physical properties of particles in the upper cloud layer of Venus. Planetary and Space Science 113-114, 120–134. doi:10.1016/j.pss.2014.11.013.

C. C. Porco, L. Dones and C. Mitchell, 2017. Could It Be Snowing Microbes on Enceladus? Assessing Conditions in Its Plume and Implications for Future Missions. Astrobiology 17, 876–901. doi:10.1089/ast.2017.1665.

C. C. Porco, P. Helfenstein, P. C. Thomas et al., 2006. Cassini Observes the Active South Pole of Enceladus. Science 311, 1393–1401. URL: https://doi.org/10.1126/science.1123013, doi:10.1126/science.1123013.

C. C. Porco, R. A. West, S. Squyres et al., 2004. Cassini Imaging Science: Instrument Characteristics And Anticipated Scientific Investigations At Saturn. Technical Report.

F. Postberg, R. N. Clark, C. J. Hansen et al., 2018. Plume and Surface Composition of Enceladus, in: R. N. Clark, J. H. Waite, P. M. Schenk et al. (Eds.), Enceladus and the Icy Moons of Saturn. University of Arizona Press, pp. 129–162. URL: http://www.jstor.org.tudelft.idm.oclc.org/stable/j.ctv65sw2b.16.

F. Postberg, S. Kempf, J. Schmidt et al., 2009. Sodium salts in E-ring ice grains from an ocean below the surface of Enceladus. Nature 459, 1098–1101. doi:10.1038/nature08046.

C. P. R. Saunders and J. S. Rimmer, 1999. The electric field alignment of ice crystals in thunderstorms. Technical Report.

J. Schmidt, N. Brilliantov, F. Spahn et al., 2008. Slow dust in Enceladus' plume from condensation and wall collisions in tiger stripe fractures. Nature 451, 685–688. doi:10.1038/nature06491.

B. Seignovert, S. L. Mouélic, M. Heslar et al., 2023. PyVIMS. URL: https://doi.org/10.5281/zenodo.7535017, doi:10.5281/zenodo.7535017.

L. Spilker, 2019. Cassini-Huygens' exploration of the Saturn system: 13 years of discovery. Science 364, 1046–1051. URL: https://www.science.org/doi/abs/10.1126/science.aat3760, doi:10.1126/science.aat3760.

D. Tamayo, M. M. Hedman and J. A. Burns, 2014. First observations of the Phoebe ring in optical light. Icarus 233, 1–8. doi:10.1016/j.icarus.2014.01.021.

D. Tamayo, S. R. Markham, M. M. Hedman et al., 2016. Radial profiles of the Phoebe ring: A vast debris disk around Saturn. Icarus 275, 117–131. doi:10.1016/j.icarus.2016.04.009.

W. Tape and J. Moilanen, 2006. Atmospheric Halos and the Search for Angle x doi:10.1029/058SP.

A. P. Thorne, 1988. Diffraction gratings, in: A. P. Thorne (Ed.), Spectrophysics. Springer Netherlands, Dordrecht, pp. 144–170. URL: https://doi.org/10.1007/978-94-009-1193-2_6, doi:10.1007/978-94-009-1193-2{_}6.

A. J. Verbiscer, M. F. Skrutskie and D. P. Hamilton, 2009. Saturn's largest ring. Nature 461, 1098–1100. doi:10.1038/nature08515.

J. W. Weiss, C. P. Porco and C. J. Mitchell, 2013. The Identification of Non-Axisymmetric Features in Cassini Low-Resolution, High-Phase Images of Saturn's E Ring, in: 44th Annual Lunar and Planetary Science Conference, p. 2989.

R. West, B. Knowles, E. Birath et al., 2010. In-flight calibration of the Cassini imaging science sub-system cameras. Planetary and Space Science 58, 1475–1488. doi:10.1016/j.pss.2010.07.006.

A. Appendix

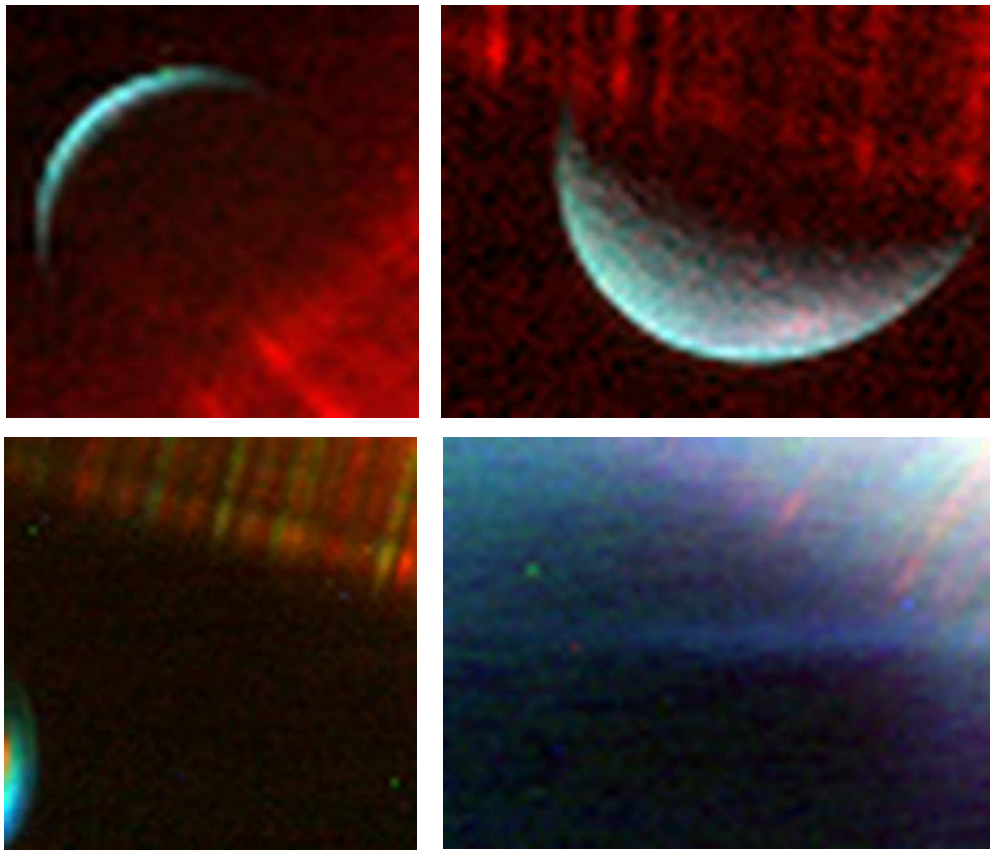

Figure 16: False colour image previews from the VIMS Data Portal (Le Mouélic et al., 2019) of other stripe observations in the VIMS-IR channel. These show RGB intensities (3.1, 2.0, 1.78 µm) of Dione cube 1818542624_1 (top left), Rhea cube 1710080519_1 (top right), and Tethys cube 1805596800_1 (bottom right). Titan cube 1536295561_1 (bottom left) is shown with RGB wavelengths of 2.77, 3.27, 3.32 µm, respectively.

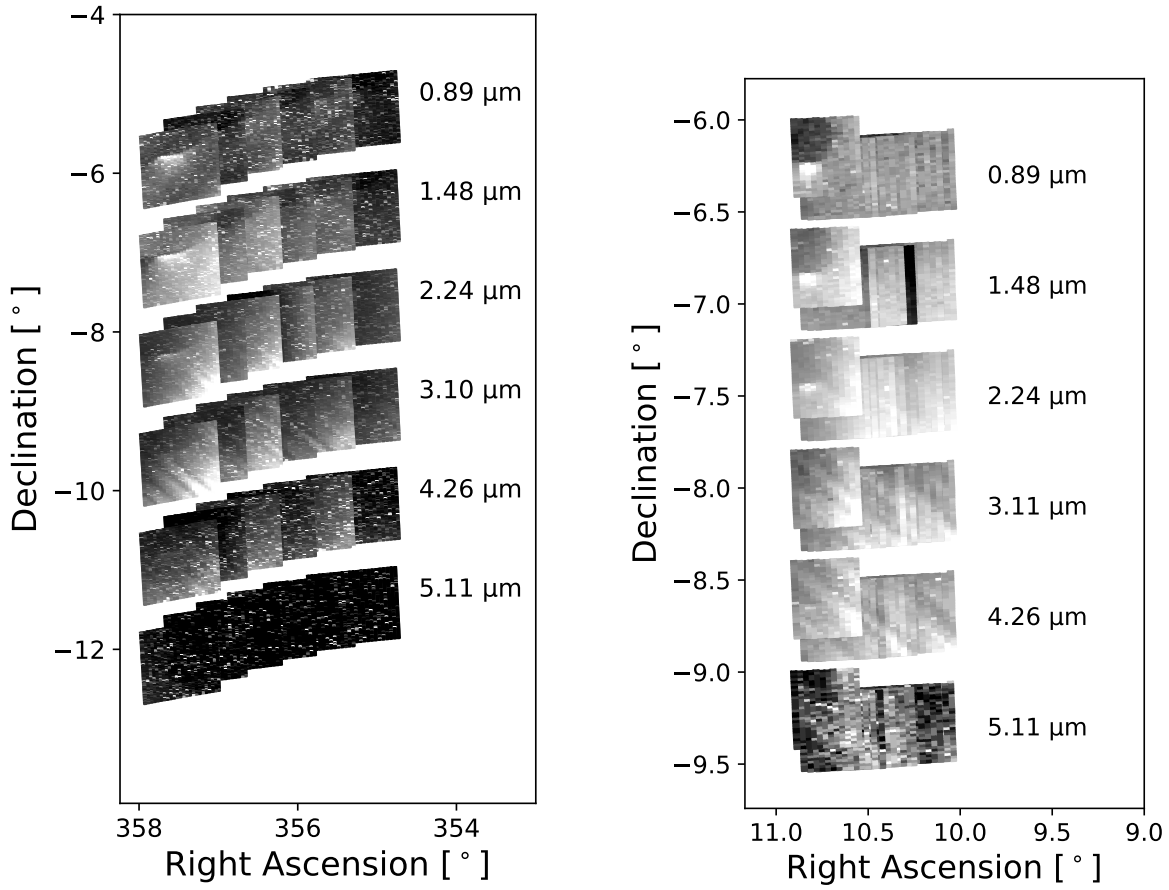

Figure 17: Cassini flyby E13 (a) and E19 (b) VIMS mosaic in terms of right ascension and declination in the J2000 reference frame for a discrete set of wavelengths. The original mosaic is given on top; every following wavelength mosaic is shown with an additional declination for clarity.

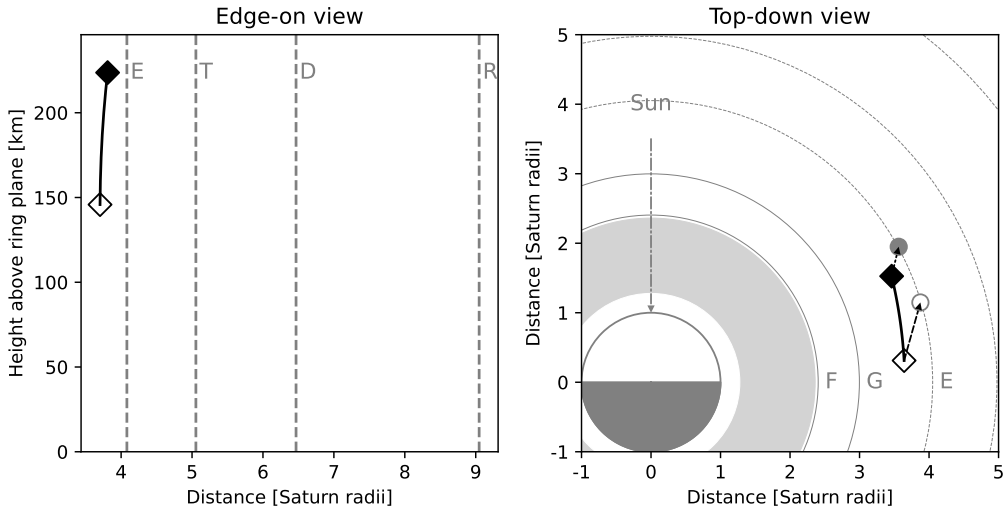

Figure 18: Cassini's E13 flyby geometry from 20/12/2010 22:53:39 to 21/12/2010 00:00:40 UTC. Cassini's position is marked by a diamond, and the moons' positions are indicated by circles. The open symbol represents the start position, and the filled symbol represents the end position. The orbits of Enceladus, Tethys, Dione, and Rhea (E, T, D, R) are represented by dashed grey lines, while the F-ring and G-ring (F, G) are shown with solid grey lines. The solar direction is indicated by a dash-dotted arrow, and the ISS/VIMS viewing direction by black dashed arrows.

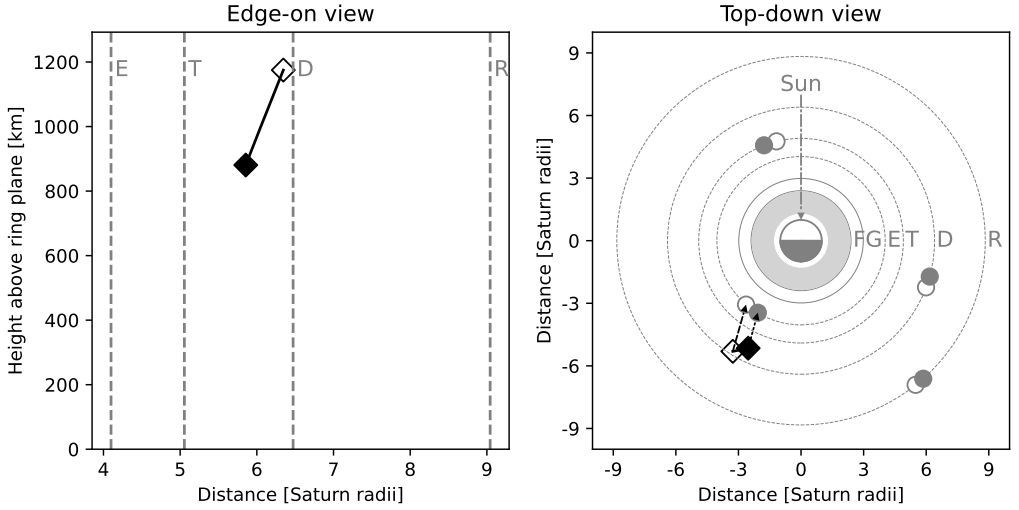

Figure 19: Cassini's E19 flyby geometry on 02/05/2012 from 05:07:13 to 06:02:00 UTC. Cassini's position is marked by a diamond, and the moons' positions are indicated by circles. The open symbol represents the start position, and the filled symbol represents the end position. The orbits of Enceladus, Tethys, Dione, and Rhea (E, T, D, R) are represented by dashed grey lines, while the F-ring and G-ring (F, G) are shown with solid grey lines. The solar direction is indicated by a dash-dotted arrow, and the ISS/VIMS viewing direction by black dashed arrows.

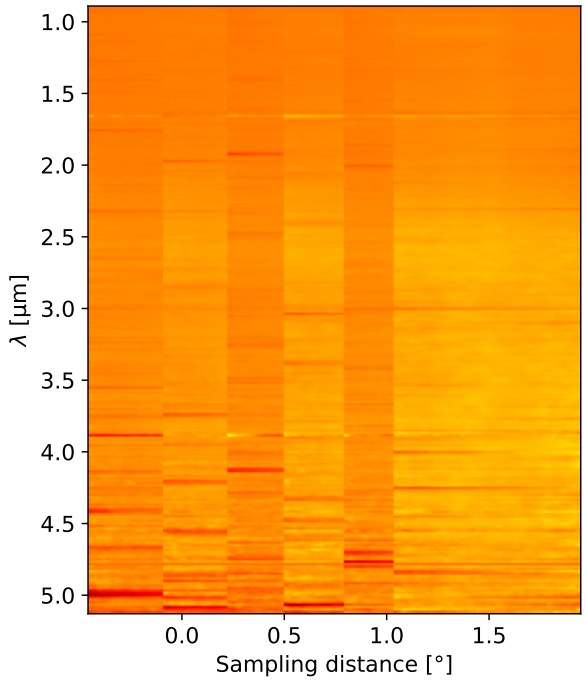

Figure 20: Spectral kymograph mosaic of Cassini flyby E13.

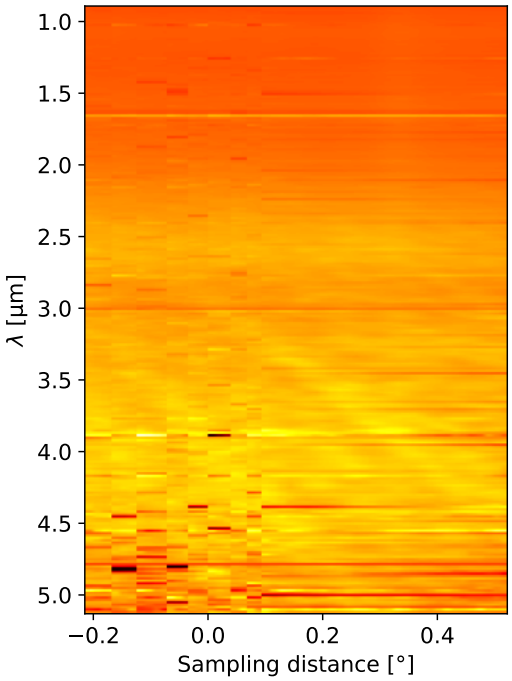

Figure 21: Spectral kymograph mosaic of Cassini flyby E19.

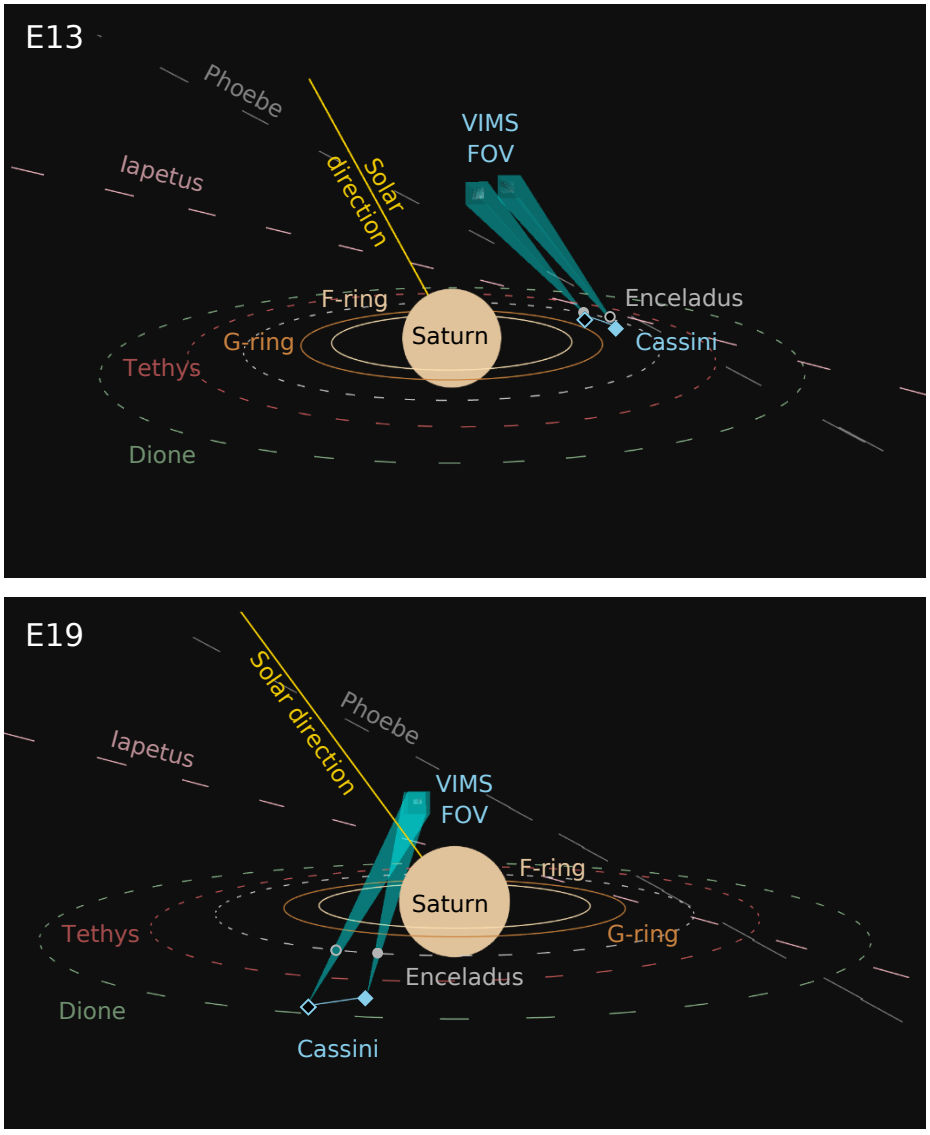

Figure 22: Overview of VIMS stripe observation geometry of flyby E13 (top) and flyby E19 (bottom) retrieved from SPICE, and projected to the distance of Phoebe's orbit

5

Conclusion & Recommendations

This chapter summarizes the findings from the scientific article in section 5.1 by addressing the research questions created in the research plan. Next, section 5.2 makes recommendations for future work.

5.1. Conclusions

The established research questions are addressed in this section using the work presented in the scientific article and the appendices.

1. *What are the expected projections of the rainbow, corona, halo, and glory optical phenomena onto Enceladus' plumes when observed from the ISS and VIMS for a complete three-dimensional observer geometry?*

   The tool described in Appendix B combines Cassini's observation geometry from SPICE with mathematical models of optical phenomena to accurately indicate when optical phenomena should be visible at specific wavelengths during Cassini's targeted flybys of Enceladus. A two-dimensional representation of the three-dimensional tool depicts how these phenomena would appear in the Cassini ISS and VIMS instrument field of view. As discussed in subsection 2.5.1, the ice particle halo and corona are the most likely optical features to occur within Enceladus' plumes. Rainbow and glory effects are highly improbable due to the lack of liquid water, as the plumes contain only gaseous and solid-phase materials.

2. *How will the plume data be analysed to find signatures of the optical phenomena?*

   A combination of VIMS and ISS observations is used. Images are initially selected based on the observational requirements generated by the tool from Appendix B. In the scientific paper, the stripe features are examined using a few methods: SPICE is used to create mosaic projections of the images in the J2000 reference frame, revealing patterns in the phenomenon's appearance across multiple images. The SPICE-enhanced observations and tools also allow us to compare the stripe's orientation to Enceladus, the Sun, and other objects in Saturn's system. Line samples taken from ISS images and VIMS cubes reveal spectral dependencies on the position of the stripes. These dependencies are investigated further by creating a spectral kymograph, which reveals diffraction patterns on a flyby scale.

3. *What can the (lack of) optical phenomenon signatures reveal about the physical and chemical structure of the plume particles*?

   The stripe features do not necessarily originate from the plume particles and cannot be used to characterise them. However, data on the particles that cause the stipes can be analysed. The VIMS spectra of the stripe phenomenon are compared to those of the plume and E-ring background. We find that the particles causing the stripes are made of crystalline water ice, similar to the plumes. Furthermore, steeper spectral slopes and the 3-micron absorption band shape of the stripes particle spectrum suggest particle size distributions with a higher abundance of larger

particles compared to the E-ring and plume, as well as a paucity of grains with a radius smaller than 2 µm. Traces of CO_2 are also found in the stripe feature particles.

4. *Can optical phenomena be observed using artificial plume experiments, and what can these reveal about the plumes' composition?*

   As outlined in chapter 3, experiments are only conducted if no optical phenomena can be detected. Since an optical phenomenon was observed, no experiments were performed, and thus, no conclusions can be drawn.

5. *What recommendations can be made for future missions to observe and exploit optical phenomena for particle characterisation?*

   Flyby trajectories can be defined to meet the illumination and observation geometries required for observing optical phenomena, as shown in Table 2.1. For these observations, the phase angle should be 180° minus the phenomenon's scattering angle. Trajectories can also be planned to observe the same medium at different phase angles, enabling the construction of phase functions that can be compared with Mie theory simulations. Furthermore, the spacecraft should aim to position itself as close as possible to the scattering medium to maximize the apparent angular size of the medium. Similarly, a large angular field of view is desirable for the instruments to replicate the extended medium conditions seen on Earth, which allow large-scale optical structures (angular sizes of approximately 5 to 50°) to be resolved. For spectral resolution, a visible-light optical camera with medium-band spectral filters should be sufficient to distinguish structures like corona and glory rings as well as rainbows and halos.

5.2. Recommendations

Recommendations can be provided on two levels: the initial search for optical phenomena such as the atmospheric corona and ice particle halo in Enceladus' plumes and the characterisation of the stripe features described in the scientific article.

5.2.1. Optical Phenomena Search in Enceladus' Plumes

Although an initial search for optical phenomena was conducted prior to discovering the stripes, the process is not extensively documented in this report, so detailed recommendations cannot be provided. However, it was noted that identifying optical phenomena in single images was challenging due to the limited fields of view in ISS NAC and VIMS, along with VIMS's low angular resolution. As a result, subsequent research should focus on comparing global intensity variations across images taken throughout a flyby.

5.2.2. Characterisation of the Stripes

- A survey of ISS and VIMS-IR data was conducted to find stripe features similar to those observed during flybys E13, E17, and E19. Expanding this survey to include VIMS-IR non-targeted flybys at high phase angles, primarily when Cassini is located between the G-ring and Rhea's orbit, is advised. Investigating other instruments with similar near-infrared sensitivity and observation geometries would also be valuable.
- Filtering the VIMS cubes to enhance the stripe contrast and reduce noise. This will aid in producing clearer spectral kymographs and deconstructing the contributions of the groove spacings and widths of the reflection grating.
- A specific configuration should be identified where the stripes remain continuous when projected at an infinite distance while physically situated between Cassini and Enceladus. This could be explored through ray tracing software or by setting up an experimental model replicating the scene's motions and illumination.
- Fitting the VIMS spectra of the bright band to particle size distributions using Mie theory, as done by [31], is recommended. A similar comparison with different ice mixtures could provide additional insights.

References

[1] C. H. Acton. *Ancillary data services of NASA's Navigation and Ancillary Information Facility*. Tech. rep. 1. Jet Propulsion Laboratory, California Institute of Technology, 1996.

[2] J. A. Adam. *The mathematical physics of rainbows and glories*. Tech. rep. 2002, pp. 229–365.

[3] C. D. Ahrens. *Meteorology today: an introduction to weather, climate, and the environment*. Cengage Learning Canada Inc, 2015. ISBN: 0176728333.

[4] A. Annex et al. "SpiceyPy: a Pythonic Wrapper for the SPICE Toolkit". In: *Journal of Open Source Software* 5.46 (Feb. 2020), p. 2050. ISSN: 2475-9066. DOI: 10.21105/joss.02050.

[5] L. Bi and P. Yang. "Accurate simulation of the optical properties of atmospheric ice crystals with the invariant imbedding T-matrix method". In: *Journal of Quantitative Spectroscopy and Radiative Transfer* 138 (May 2014), pp. 17–35. ISSN: 00224073. DOI: 10.1016/j.jqsrt.2014.01.013.

[6] M. T. Bland et al. "A New Enceladus Global Control Network, Image Mosaic, and Updated Pointing Kernels From Cassini's 13-Year Mission". In: *Earth and Space Science* 5.10 (Oct. 2018), pp. 604–621. ISSN: 23335084. DOI: 10.1029/2018EA000399.

[7] C. F. Bohren and D. R. Huffman. *Absorption and Scattering of Light by Small Particles*. Wiley, Apr. 1998. ISBN: 9780471293408. DOI: 10.1002/9783527618156.

[8] R. H. Brown et al. "The Cassini Visual And Infrared Mapping Spectrometer (Vims) Investigation". In: *Space Science Reviews* 115.1 (2004), pp. 111–168. ISSN: 1572-9672. DOI: 10.1007/s11214-004-1453-x. URL: https://doi.org/10.1007/s11214-004-1453-x.

[9] R. H. Brown et al. *Cassini Final Mission Report Volume 1: Mission Overview & Science Objectives and Results*. Tech. rep. NASA Jet Propulsion Laboratory, 2019.

[10] C. E. Carr, M. T. Zuber, and G. Ruvkun. "Life detection with the Enceladus Orbiting Sequencer". In: *IEEE Aerospace Conference Proceedings*. 2013. ISBN: 9781467318112. DOI: 10.1109/AERO.2013.6497129.

[11] B. Casselman. *The Mathematics of the Rainbow*. 2024.

[12] G. Choblet et al. "Enceladus as a potential oasis for life: Science goals and investigations for future explorations". In: *Experimental Astronomy* 54.2 (2022), pp. 809–847. ISSN: 1572-9508. DOI: 10.1007/s10686-021-09808-7. URL: https://doi.org/10.1007/s10686-021-09808-7.

[13] J. Cowley. *Corona Formation: Exploring the Phenomenon of Light Diffraction*. Mar. 2024.

[14] W. Degruyter and M. Manga. "Cryoclastic origin of particles on the surface of Enceladus". In: *Geophysical Research Letters* 38.16 (Aug. 2011). ISSN: 00948276. DOI: 10.1029/2011GL048235.

[15] T. Denk et al. "The irregular satellites of Saturn". In: *Enceladus and the Icy Moons of Saturn* (2018), p. 409.

[16] D. Dhingra et al. "Spatially resolved near infrared observations of Enceladus' tiger stripe eruptions from Cassini VIMS". In: *Icarus* 292 (Aug. 2017), pp. 1–12. ISSN: 10902643. DOI: 10.1016/j.icarus.2017.03.002.

[17] M. K. Dougherty, L. W. Esposito, and S. M. Krimigis. *Saturn from cassini-huygens*. Springer Netherlands, 2009, pp. 1–805. ISBN: 9781402092169. DOI: 10.1007/978-1-4020-9217-6.

[18] A. Farkas. *Possible extraterrestrial halo displays-a review*. Tech. rep. URL: http://atoptics.co.uk.

[19] F. Favata et al. *Introducing the Voyage 2050 White Papers, contributions from the science community to ESA's long-term plan for the Scientific Programme*. June 2021. DOI: 10.1007/s10686-021-09746-4.

[20] S. D. Gedzelman. “OPTICS, ATMOSPHERIC | Optical Phenomena”. In: *Encyclopedia of Atmospheric Sciences*. Ed. by J. R. Holton. Oxford: Academic Press, 2003, pp. 1583–1594. ISBN: 978-0-12-227090-1. DOI: https://doi.org/10.1016/B0-12-227090-8/00284-0. URL: https://www.sciencedirect.com/science/article/pii/B0122270908002840.

[21] S. D. Gedzelman. *Simulating glories and cloudbows in color*. Tech. rep. 2003.

[22] S. D. Gedzelman and J. A. Lock. *Simulating coronas in color*. Tech. rep. 2003.

[23] S. D. Gedzelman. *Simulating rainbows in their atmospheric environment*. Tech. rep. 2008.

[24] S. D. Gedzelman. *Visibility of halos and rainbows*. Tech. rep. 1980.

[25] J. D. Goguen et al. “The temperature and width of an active fissure on Enceladus measured with Cassini VIMS during the 14 April 2012 South Pole flyover”. In: *Icarus* 226.1 (Sept. 2013), pp. 1128–1137. ISSN: 00191035. DOI: 10.1016/j.icarus.2013.07.012.

[26] D. B. Goldstein et al. “Enceladus plume dynamics: from surface to space”. In: *Enceladus and the Icy Moons of Saturn* 175 (2018).

[27] J. He et al. “Refractive Index and Extinction Coefficient of Vapor-deposited Water Ice in the UV–vis Range”. In: *The Astrophysical Journal* 925.2 (Feb. 2022), p. 179. ISSN: 0004-637X. DOI: 10.3847/1538-4357/ac3fbb.

[28] M. M. Hedman et al. “Connections between spectra and structure in Saturn’s main rings based on Cassini VIMS data”. In: *Icarus* 223.1 (Mar. 2013), pp. 105–130. ISSN: 00191035. DOI: 10.1016/j.icarus.2012.10.014.

[29] M. M. Hedman et al. “Spatial variations in the dust-to-gas ratio of Enceladus’ plume”. In: *Icarus* 305 (May 2018), pp. 123–138. ISSN: 10902643. DOI: 10.1016/j.icarus.2018.01.006.

[30] M. M. Hedman et al. “Spectral observations of the enceladus plume with cassini-vims”. In: *Astrophysical Journal* 693.2 (Mar. 2009), pp. 1749–1762. ISSN: 15384357. DOI: 10.1088/0004-637X/693/2/1749.

[31] M. M. Hedman et al. “Three tenuous rings/arcs for three tiny moons”. In: *Icarus* 199.2 (Feb. 2009), pp. 378–386. ISSN: 00191035. DOI: 10.1016/j.icarus.2008.11.001.

[32] H. W. Hsu et al. “Stream particles as the probe of the dust-plasma-magnetosphere interaction at Saturn”. In: *Journal of Geophysical Research: Space Physics* 116.9 (2011). ISSN: 21699402. DOI: 10.1029/2011JA016488.

[33] H. W. Hsu, S. Kempf, and C. M. Jackman. “Observation of saturnian stream particles in the interplanetary space”. In: *Icarus* 206.2 (Apr. 2010), pp. 653–661. ISSN: 00191035. DOI: 10.1016/j.icarus.2009.06.033.

[34] A. P. Ingersoll and S. P. Ewald. “Total particulate mass in Enceladus plumes and mass of Saturn’s E ring inferred from Cassini ISS images”. In: *Icarus* 216.2 (Dec. 2011), pp. 492–506. ISSN: 00191035. DOI: 10.1016/j.icarus.2011.09.018.

[35] A. P. Ingersoll, S. P. Ewald, and S. K. Trumbo. “Time variability of the Enceladus plumes: Orbital periods, decadal periods, and aperiodic change”. In: *Icarus* 344 (July 2020). ISSN: 10902643. DOI: 10.1016/j.icarus.2019.06.006.

[36] B. Knowles. “Cassini imaging science Subsystem (ISS) data User’s Guide”. In: *PDS https://pds-rings. seti. org/cassini* 2016 (2018).

[37] V. Kofman et al. “The Refractive Index of Amorphous and Crystalline Water Ice in the UV–vis”. In: *The Astrophysical Journal* 875.2 (Apr. 2019), p. 131. ISSN: 0004-637X. DOI: 10.3847/1538-4357/ab0d89.

[38] G. P. Können. *Polarized light in nature*. Cambridge University Press, 1985, p. 172. ISBN: 0521258626.

[39] N. W. Kutsop et al. “Titan Stratospheric Haze Bands Observed in Cassini VIMS as Tracers of Meridional Circulation”. In: *Planetary Science Journal* 3.5 (May 2022). ISSN: 26323338. DOI: 10.3847/PSJ/ac582d.

[40] P. Laven. “Re-visiting the atmospheric corona”. In: *Applied Optics* 54.4 (Feb. 2015), B46. ISSN: 1559-128X. DOI: 10.1364/ao.54.000b46.

[41] P. Laven. “Simulation of rainbows, coronas and glories using Mie theory and the Debye series”. In: *Journal of Quantitative Spectroscopy and Radiative Transfer* 89.1-4 (Nov. 2004), pp. 257–269. ISSN: 00224073. DOI: 10.1016/j.jqsrt.2004.05.026.

[42] P. Laven. “Supernumerary arcs of rainbows: Young’s theory of interference”. In: *Applied Optics* 56.19 (July 2017), G104. ISSN: 0003-6935. DOI: 10.1364/ao.56.00g104.

[43] S. Le Mouélic et al. “The Cassini VIMS archive of Titan: From browse products to global infrared color maps”. In: *Icarus* 319 (Feb. 2019), pp. 121–132. ISSN: 10902643. DOI: 10.1016/j.icarus.2018.09.017.

[44] M. T. Lemmon et al. “Hexagonal Prisms Form in Water-Ice Clouds on Mars, Producing Halo Displays Seen by Perseverance Rover”. In: *Geophysical Research Letters* 49.17 (Sept. 2022). ISSN: 19448007. DOI: 10.1029/2022GL099776.

[45] D. K. Lynch and P. Schwartz. *Rainbows and fogbows*. Tech. rep. 1991.

[46] W. J. Markiewicz et al. “Glory on Venus cloud tops and the unknown UV absorber”. In: *Icarus* 234 (May 2014), pp. 200–203. ISSN: 0019-1035. DOI: 10.1016/J.ICARUS.2014.01.030.

[47] W. J. Markiewicz, E. V. Petrova, and O. S. Shalygina. “Aerosol properties in the upper clouds of Venus from glory observations by the Venus Monitoring Camera (Venus Express mission)”. In: *Icarus* 299 (Jan. 2018), pp. 272–293. ISSN: 10902643. DOI: 10.1016/j.icarus.2017.08.011.

[48] R. M. Mastrapa et al. “Optical constants of amorphous and crystalline h2o-ice: 2.5-22 μm (4000-455 cm-1) optical constants of h2o-ice”. In: *Astrophysical Journal* 701.2 (2009), pp. 1347–1356. ISSN: 15384357. DOI: 10.1088/0004-637X/701/2/1347.

[49] B. Mayer et al. *Atmospheric Chemistry and Physics Remote sensing of water cloud droplet size distributions using the backscatter glory: a case study*. Tech. rep. 2004, pp. 1255–1263. URL: www.atmos-chem-phys.org/acp/4/1255/.

[50] G. Mie. “Beiträge zur Optik trüber Medien, speziell kolloidaler Metallösungen”. In: *Annalen der Physik* 330.3 (Jan. 1908), pp. 377–445. ISSN: 0003-3804. DOI: 10.1002/andp.19083300302.

[51] C. Mobley. *Ocean Optics Web Book: Mie theory Overview*. 2024. URL: https://www.oceanopticsbook.info/view/theory-electromagnetism/level-2/mie-theory-overview.

[52] J. Moilanen and M. Gritsevich. “Light scattering by airborne ice crystals – An inventory of atmospheric halos”. In: *Journal of Quantitative Spectroscopy and Radiative Transfer* 290 (Nov. 2022). ISSN: 00224073. DOI: 10.1016/j.jqsrt.2022.108313.

[53] Navigation and Ancillary Information Facility. *NAIF Reference Frames and Coordinate Systems in the SPICE Context*. Tech. rep. 2023.

[54] H. M. Nussenzveig. “THE SCIENCE OF THE GLORY”. In: *Scientific American* 306.1 (2012), pp. 68–73. ISSN: 00368733, 19467087. URL: http://www.jstor.org.tudelft.idm.oclc.org/stable/26014160.

[55] J. Oberst et al. “Enceladus geodetic framework”. In: *International Archives of the Photogrammetry, Remote Sensing and Spatial Information Sciences - ISPRS Archives*. Vol. 42. 3W1. International Society for Photogrammetry and Remote Sensing, July 2017, pp. 113–118. DOI: 10.5194/isprs-archives-XLII-3-W1-113-2017.

[56] R. S. Park et al. “The Global Shape, Gravity Field, and Libration of Enceladus”. In: *Journal of Geophysical Research: Planets* 129.1 (Jan. 2024). ISSN: 21699100. DOI: 10.1029/2023JE008054.

[57] *PDS Planetary Image Atlas*. Mar. 2024. URL: https://pds-imaging.jpl.nasa.gov/search/.

[58] E. V. Petrova, O. S. Shalygina, and W. J. Markiewicz. “The VMC/VEx photometry at small phase angles: Glory and the physical properties of particles in the upper cloud layer of Venus”. In: *Planetary and Space Science* 113-114 (Aug. 2015), pp. 120–134. ISSN: 00320633. DOI: 10.1016/j.pss.2014.11.013.

[59] *Planetary Data System Software*. Mar. 2024. URL: https://pds-rings.seti.org/cassini/iss/software.html.

[60] C. C. Porco et al. “Cassini Observes the Active South Pole of Enceladus”. In: *Science* 311.5766 (Mar. 2006), pp. 1393–1401. DOI: 10.1126/science.1123013. URL: https://doi.org/10.1126/science.1123013.

[61] C. C. Porco et al. *Cassini Imaging Science: Instrument Characteristics And Anticipated Scientific Investigations At Saturn*. Tech. rep. Nov. 2004, pp. 363–497.

[62] C. C. Porco, L. Dones, and C. Mitchell. “Could It Be Snowing Microbes on Enceladus? Assessing Conditions in Its Plume and Implications for Future Missions”. In: *Astrobiology* 17.9 (Sept. 2017), pp. 876–901. ISSN: 15311074. DOI: 10.1089/ast.2017.1665.

[63] F. Postberg et al. “A salt-water reservoir as the source of a compositionally stratified plume on Enceladus”. In: *Nature* 474.7353 (June 2011), pp. 620–622. ISSN: 00280836. DOI: 10.1038/nature10175.

[64] F. Postberg et al. “Sodium salts in E-ring ice grains from an ocean below the surface of Enceladus”. In: *Nature* 459.7250 (June 2009), pp. 1098–1101. ISSN: 00280836. DOI: 10.1038/nature08046.

[65] F. Postberg et al. “Plume and Surface Composition of Enceladus”. In: *Enceladus and the Icy Moons of Saturn*. Ed. by R. N. Clark et al. University of Arizona Press, 2018, pp. 129–162. ISBN: 9780816537075. URL: http://www.jstor.org.tudelft.idm.oclc.org/stable/j.ctv65sw2b.16.

[66] S. Prahl. *miepython, Pure python calculation of Mie scattering*. May 2024. DOI: 10.5281/zenodo.11135148. URL: https://doi.org/10.5281/zenodo.11135148.

[67] X. Quan and E. S. Fry. *Empirical equation for the index of refraction of seawater*. Tech. rep.

[68] W. R. Rocha et al. “Water ice: Temperature-dependent refractive indexes and their astrophysical implications”. In: *Astronomy and Astrophysics* 681 (Jan. 2024). ISSN: 14320746. DOI: 10.1051/0004-6361/202347437.

[69] K. Sassen. *Corona-producing cirrus cloud properties derived from polarization lidar and photographic analyses*. Tech. rep. 1991.

[70] D. J. Segeistein. *The complex refractive index of water*. Tech. rep. 1975.

[71] B. Seignovert et al. *PyVIMS*. Jan. 2023. DOI: 10.5281/zenodo.7535017. URL: https://doi.org/10.5281/zenodo.7535017.

[72] J. A. Shaw and M. Vollmer. “Near infrared photography of atmospheric optical phenomena”. In: *Optics InfoBase Conference Papers*. Vol. Part F130-ETOP 2019. Optica Publishing Group (formerly OSA), 2019. ISBN: 9781510629790. DOI: 10.1117/12.2523165.

[73] L. Spilker. “Cassini-Huygens’ exploration of the Saturn system: 13 years of discovery”. In: *Science* 364.6445 (2019), pp. 1046–1051. DOI: 10.1126/science.aat3760. URL: https://www.science.org/doi/abs/10.1126/science.aat3760.

[74] J. N. Spitale et al. “Curtain eruptions from Enceladus’south-polar terrain”. In: *Nature* 521.7550 (May 2015), pp. 57–60. ISSN: 14764687. DOI: 10.1038/nature14368.

[75] R. Stull. *22: ATMOSPHERIC OPTICS*. Tech. rep. URL: https://geo.libretexts.org/@go/page/10194.

[76] B. D. Teolis et al. “Enceladus Plume Structure and Time Variability: Comparison of Cassini Observations”. In: *Astrobiology* 17.9 (Sept. 2017), pp. 926–940. ISSN: 15311074. DOI: 10.1089/ast.2017.1647.

[77] R. A. R. Tricker. *An introduction to meteorological optics.* 1971.

[78] M. Vollmer. *Effects of absorbing particles on coronas and glories*. Tech. rep. 2005.

[79] M. Vollmer and J. A. Shaw. “Atmospheric optics in the near infrared”. In: *Applied Optics* 56.19 (July 2017), G145. ISSN: 0003-6935. DOI: 10.1364/ao.56.00g145.

[80] S. G. Warren and R. E. Brandt. “Optical constants of ice from the ultraviolet to the microwave: A revised compilation”. In: *Journal of Geophysical Research Atmospheres* 113.14 (2008). ISSN: 01480227. DOI: 10.1029/2007JD009744.

[81] X. Xu et al. “Identification of Supercooled Cloud Water by FY-4A Satellite and Validation by CALIPSO and Airborne Detection”. In: *Remote Sensing* 15.1 (Jan. 2023). ISSN: 20724292. DOI: 10.3390/rs15010126.

[82] P. Yang et al. “Uncertainties associated with the surface texture of ice particles in satellite-based retrieval of cirrus clouds: Part II - Effect of particle surface roughness on retrieved cloud optical thickness and effective particle size”. In: *IEEE Transactions on Geoscience and Remote Sensing* 46.7 (July 2008), pp. 1948–1957. ISSN: 01962892. DOI: 10.1109/TGRS.2008.916472.

[83] S. K. Yeoh et al. “On understanding the physics of the Enceladus south polar plume via numerical simulation”. In: *Icarus* 253 (June 2015), pp. 205–222. ISSN: 10902643. DOI: 10.1016/j.icarus.2015.02.020.

A

Cassini Instrument Details

Table A.1: Cassini ISS characteristics [36]

General		
CPU	IBM MIL-STD-1750A 16-bit processor	
CCD	Three-phase, front-side illuminated	
Pixel size	12 µm	
Format	1024 × 1024	
Available exposures	64 commandable settings, 5 msec–1200 s	
Minimum framing time	11 s (4 × 4 sum, highest CDS pickup rate)	
Signal digitization	12 bits, 4095 DN	
Summation modes	1 × 1, 2 × 2, 4 × 4	
Pixel full well	120,000 e− (normal); 1,000,000 e− (low gain, 4 × 4)	
Data conversion (12:8)	'Square Root Encoding' (LUT), Least-Significant 8 Bits (L58B)	
Data compression	Lossless; Lossy	
Read noise level	12 e− (high gain state)	
	NAC	WAC
Type	Reflector	Refractor
Mass	30.5 kg	26.4 kg
Dimensions	95 cm × 40 cm × 33 cm	55 cm × 35 × 33 cm
F/N	10.5	3.5
Focal length	2002.70 ± 0.07 mm	200.77 ± 0.02 mm
Pixel angular size	5.9907 µr/pixel	59.749 µr/pixel
FOV	6.134 mrad	61.18 mrad
FWHM of PSF	1.3 pixels	1.8 pixels
Peak power (active)	26.2 W	19.4 W
Spectral range	200–1050 nm	380–1050 nm
Filter positions	12 × 2 filter wheels	9 × 2 filter wheels
Gain state	0: 1: 2: 3	0: 1: 2: 3
Gain values (e-/DN)	233: 99: 30: 13	211: 85: 28: 12
Gain state factors	0.13: 0.31: 1.0: 2.36	0.13: 0.31: 1.0: 2.36
Limiting magnitudes (in $t_{\text{exp}} = 1$s, gain state 2, 12-bit data)	$M_v \sim 14$	$M_v \sim 11.6$

Table A.2: VIMS-VIS and VIMS-IR optical system characteristics from Brown et al. [8].

Parameter	VIMS-VIS	VIMS-IR	Total System
Spectral coverage	0.35–1.0 µm (0.3–1.0 µm by special command)	0.85–5.1 µm	0.35–5.1 µm or 0.3–5.1 µm
Spectral sampling	7.3 nm/spectral (96 bands) 1 × 5 sum	16.6 nm/spectral (256 bands)	
Spatial characteristics			
Instantaneous field of view (IFOV)	0.17 × 0.17 mrad	0.25 × 0.5 mrad	
Effective IFOV	0.5 × 0.5 mrad (3 × 3 sum)	0.5 (0.5 mrad (1 × 2 sum)	0.5 × 0.5 mrad
Total field of view	64 × 64 pixels (32 × 32 mrad)	64 × 64 pixels (32 × 32 mrad)	32 × 32 mrad
Swath width	576 IFOVs (3 × 3 × 64)	128 IFOV (2 × 64)	32 mrad
Image size modes (fast scan)	1–64 pixels	1–64 pixels	1–64 pixels
Image size modes (slow scan)	1–64 pixels	1–64 pixels	1–64 pixels

Table A.3: ISS Filter Characteristics, all wavelengths in nm. Central wavelengths ('cen') are computed using the full system transmission function. These numbers are taken to be the numerical name assigned to the filter. Effective wavelengths ('eff') are computed using the full system transmission function convolved with a solar spectrum. Bandpass types: SP: short wavelength cutoff; W: wide; N: narrow; LP: long wavelength cutoff [61].

Filter	$\lambda_{cen,NAC}$	$\lambda_{eff,NAC}$	$\lambda_{cen,WAC}$	$\lambda_{eff,WAC}$	Science justification
UV1	258W	264	–	–	Aerosols
UV2	298W	306	–	–	Aerosols, broad-band color
UV3	338W	343	–	–	Aerosols, broad-band color, polarization
VIO	–	–	420SP	420	Broad-band color
BL2	440M	441	–	–	Medium-band color, polarization
BL1	451W	455	460W	463	Broad-band color
GRN	568W	569	567W	568	Broad-band color
MT1	619N	619	–	–	Methane band, vertical sounding
CB1	619N	619	–	–	Two-lobed continuum for MT1
CB1a	635	635	–	–	–
CB1b	603	603	–	–	–
RED	650W	649	648W	647	Broad-band color
HAL	656N	656	656N	656	H-alpha/lightning
MT2	727N	727	728N	728	Methane band, vertical sounding
CB2	750N	750	752N	752	Continuum for MT2
IR1	752W	750	742W	740	Broad-band color
IR2	862W	861	853W	852	Broad-band color; ring absorption band
MT3	889N	889	890N	890	Methane band, vertical sounding
CB3	938N	938	939N	939	Continuum for MT3; see thru Titan haze
IR3	930W	928	918W	917	Broad-band color
IR4	1002LP	1001	1001LP	1000	Broad-band color
IR5	–	–	1028LP	1027	Broad-band color
CL1	611	651	635	634	Wide open, combine with wheel 2 filters
CL2	611	651	635	634	Wide open, combine with wheel 1 filters
P0	617	633	–	–	Visible polarization, 0°
P60	617	633	–	–	Visible polarization, 60°
P120	617	633	–	–	Visible polarization, 120°
IRP0	746	738	705	705	IR polarization; see through Titan haze
IRP90	–	–	705	705	IR polarization; see through Titan haze

B

SPICE Projection Tools

This appendix elaborates on the 3-dimensional visualisation tools which were created for the analysis of optical phenomena in Enceladus' plumes as well as the assessment of the stripe anomaly observed in chapter 4. First, the retrieval of the geometry data and the construction of the first iteration of the tool including optical phenomena will be presented in subsection B.1.4. Next, a derivation of the tool with 2-dimensional projections of the optical phenomena on the images will be discussed in section B.2. Lastly, the second iteration of the tool for analysis of the stripe features with 3-dimensional projections of VIMS data will be shown in section B.3. The tools can be downloaded from https://github.com/nrubbrecht/thesis_tools_pub.git.

B.1. Tool Iteration 1: Enceladus-Centered Optical Phenomena

The aim is to develop a tool that indicates when optical phenomena should be visible to the ISS and VIMS instruments during Cassini's Enceladus-targeted flybys. Additionally, the tool must simulate how these phenomena would appear in the images. This enables a focused search for optical phenomena within the extensive data gathered by Cassini.

B.1.1. SPICE Data Retrieval and Integration

In order to have 3-dimensional overview of the observation geometry and illumination conditions during Cassini's flybys, one must know the relative positions between the Sun, Enceladus and Cassini. This information is publicly available from the "SPICE" (Spacecraft, Planet, Instrument, C-matrix, Events) observation geometry information system created by NASA's Navigation and Ancillary Information Facility (NAIF) [1]. This system helps scientists plan and interpret scientific observations from space-based instruments aboard robotic planetary spacecraft. To compute relevant observation geometry characteristics such as locations, altitudes, lighting angles, and latitudes and longitudes, SPICE data files—also known as "kernels"—must be used with SPICE Toolkit software. The majority of SPICE software comes in the form of application program interfaces (APIs), often known as subroutines or modules, which users incorporate into their own application programs. This analyses will use the SpiceyPy python wrapper [4] to interact with planetary and spacecraft ephemeris (trajectory) data from SPICE [1].

B.1.2. Reference Frames and Coordinate Systems

Ephemeris and orientation objects in SPICE are defined with respect to a set reference frame. Some documentation outside of SPICE refers to a reference frame as a "coordinate frame." However, in SPICE, a coordinate system specifies a mechanism for locating points within a reference frame [53]. Figure B.1 shows the common style for specifying positions in a reference frame compared to the SPICE style. In SPICE, the position of a target is determined by the coordinate system of the observer with both the target and the observer being located in a reference frame. One must be aware of the reference frame and coordinate system in use while creating or utilising state (position and velocity) or orientation (pointing) data. It is chosen to work with Cartesian position vectors as these allow for the most straightforward conversions between reference frames.

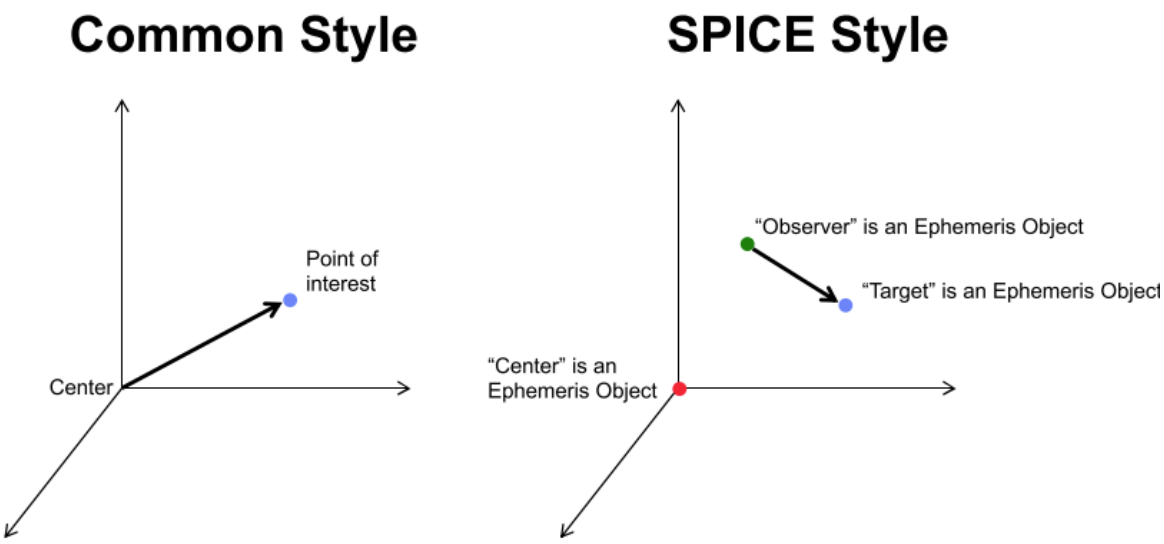

Figure B.1: Common positioning and SPICE positioning coordinate system styles.

Three ephemeris objects are taken in consideration for the selection of the optimal reference frame for the tool. These include the relative positions and velocities of the Sun (illumination source), Enceladus (target) and Cassini (observer). For simplicity, keeping the lighting geometry of the plume particles (relative position of the Sun to Enceladus) constant during the flyby is desired. This is because it determines the origin of the optical phenomena. Such geometry can be approximated using the J2000 frame shown in Figure B.2, based on the earth's equator and equinox [53]. This frame is an inertial reference frame, meaning it is non-rotating with respect to the stars and has a non-accelerating origin. For integration in the tool, the International Celestial Reference Frame (ICRF) was selected. The ICRF frame definition is used instead of the J2000 frame in SPICE as the ICRF coordinate axes are closely aligned to those of the J2000 reference frame with a rotational offset of under 0.1 arcseconds [53].

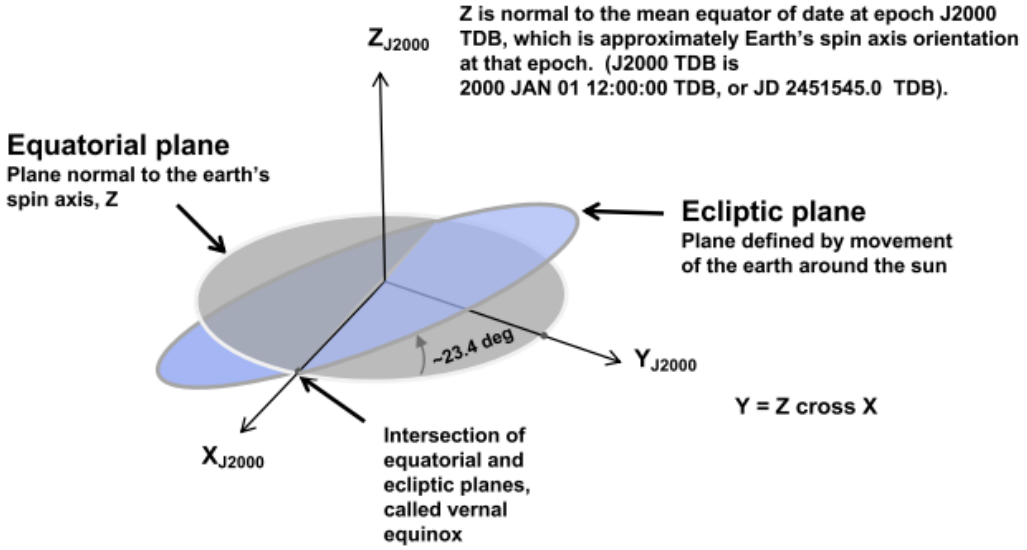

Figure B.2: J2000 inertial frame definition [53].

To verify the assumption of a constant position of Enceladus relative to the Sun, the change in Enceladus' ephemeris as observed by the Sun must be checked during the timescale of a flyby. Two contributions to this position shift exist: the orbital rotation of Saturn around the Sun, and the orbital rotation of Enceladus around Saturn. It is assumed that a flyby takes around 6 hours in total (range of three hours from closest approach). If Saturn needs 29.4 years [1] to complete one revolution around

the Sun, the angular change in position during a six-hour flyby will be 30 arcseconds, which is negligible for optical phenomena. Enceladus revolves around Saturn with an orbital period of 1.37 days [35], so Enceladus would have completed about a quarter of its orbit after a 6 hour flyby. Therefore, the maximum angular separation α between the Sun–Enceladus vectors before and after a quarter orbit can be approximated by the trigonometric relation $\tan(\alpha) = a_{Enc}/d_{Sun-Sat}$, where $a_{Enc} = 237,948$ km (semi-major axis of Enceladus) and $d_{Sun-Sat} = 9.58$ AU (semi-major axis of Saturn) [1]. This results in a maximum difference of $\alpha = 34.2$ arcseconds in illumination angle which is deemed acceptable for the tool.

B.1.3. SPICE Kernel Contributions

In SPICE, positions and orientations of objects are called based on an ephemeris time or ET which is an astronomical time unit. Cassini data archives like the Planetary Data System (PDS) search atlas [57] also use ET to filter search results. Therefore, it was decided that the tool should interactively show the Cassini's observation geometries based on time inputs. In order to retrieve the positions and orientations of the objects of interest, specific SPICE kernels must be downloaded from the NAIF Planetary Data System Navigation Node[1] and be called upon inside the tool. These include [1]:

- LSK: Leap Seconds-Kernel used to compute time conversions.
- SPK: Reference for the SPICE ephemeris subsystem and SP-Kernel, used to provide the ephemeris (trajectory) of a solar system body, a space vehicle, or any other physical object.
- CK: Cassini Camera Kernel, used to provide the orientation of a spacecraft or an articulating component of a spacecraft or instrument
- FK: Cassini Subsystem and Frames Specification Kernel, used to establish the relationships between various reference frames and to provide either the data – or references to the data—needed to construct the transformations between these reference frames.
- SCLK: Cassini spacecraft clock subsystem and the Spacecraft Clock Kernel, used to convert epochs (times) between Cassini clock time system and other time systems
- IK: Instrument kernel, contains references to the mounting alignment, internal and FOV geometry of an instrument

Ephemeris Objects

The SPK files return the object's state at a particular empheris time or ET. The LSK file is required since it can be used as an argument to call the SPK files using different time conventions like the Coordinated Universal Time (UTC). A single general leap seconds kernel, as well as Solar System and Saturnian satellite ephemeris kernels, can be downloaded for periods of time far beyond the Cassini mission's lifetime. However, the Cassini spacecraft ephemeris files cover time intervals of days. As a result, individual files had to be downloaded for each flyby based on the labelled time ranges. After loading the aforementioned kernels, the user of the tool can enter one of the 22 Cassini Enceladus flyby names (e.g. E1 to E22) and a time range in UTC from the closest approach to access the SPICE ephemeris data. From the time range input, the tool displays the Cartesian position vectors of the Sun and Cassini in kilometres as observed from Enceladus in the ICRF reference frame as shown in Figure B.3. This is according to the SPICE style approach shown in Figure B.1. Positions are chosen to be observed from Enceladus as the moon lies at the centre of potential optical phenomena in the plumes. For the given time range, the mean solar direction is computed and plotted with respect to Enceladus (shown in yellow). The Cassini flyby trajectory (black) is shown for a time range of six minutes from the closest approach.

Plume Orientation

The disadvantage of not using an Enceladus body-fixed frame such as the International Astronomical Union (IAU) Enceladus frame [53] is that the location of the plume can change in time with respect to the inertial reference frame. On the other hand, if the IAU frame is chosen for the model, the lighting geometry will not be fixed anymore as the IAU frame co-rotates with the surface of the body. Therefore, to remain in the ICRF frame, the location of the plume in the ICRF frame must be determined for each ET.

[1] Link to NAIF PDS Navigation Node

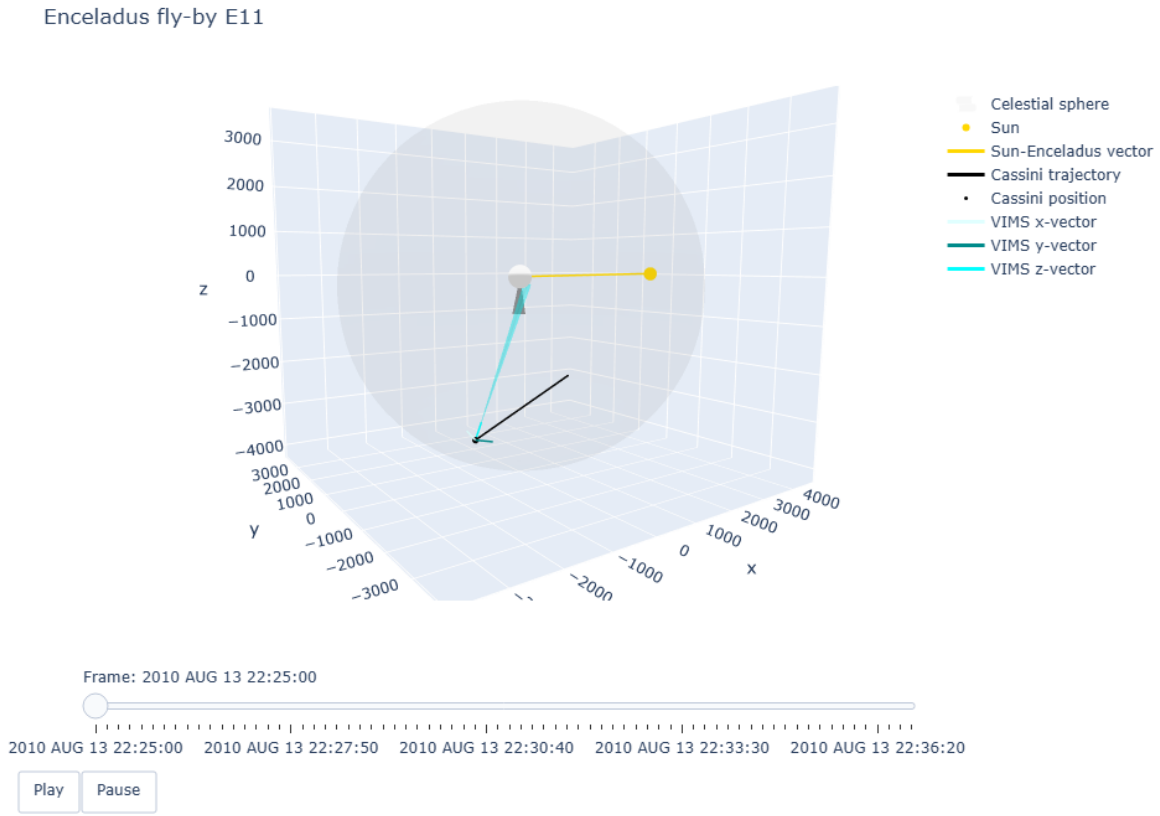

Figure B.3: 3D view of Cassini's E11 flyby generated using the SPICE tool. Cassini's trajectory is shown in black, the VIMS FOV in blue, with Enceladus and its plumes depicted in white and gray, respectively.

The orientation of Enceladus can be retrieved using the planetary constants kernel (PCK). Because the plumes are located on the south-polar terrain [74, 76], it can be assumed that the plumes are pointing in the direction of the negative spin axis. Therefore, the plume direction can be directly compared to the precession of Enceladus poles. From Oberst et al. [55], variations in the pole direction on the timescale of a single flyby (a few hours) are negligible. Therefore, the tool will use the mean plume orientation when considering a single flyby time range. Figure B.3 shows an example of the plume depicted in dark grey in the ICRF reference frame.

Cassini Instrument Pointing

Apart from being in the right location to observe optical phenomena, the Cassini instruments must also look in the right direction [1]. Similar to the Cassini ephemeris kernels, the CK kernels are obtained for individual flybys. The FK, SCLK and IK kernels are general files independent of ET and only need to be downloaded once. From these inputs, the instrument orientation and FOV can be determined and converted from the instrument frame to the ICRF reference frame for specified ETs. The user can input the name for either the ISS NAC/WAC or VIMS VIS/IR to get the desired FOVs. The pre-downloaded CK kernels allow time ranges up to 10 hours from the closest flyby but this can be extended by downloading neighbouring kernels from naif.jpl.nasa.gov/pub/naif/CASSINI/kernels/.

The VIMS FOV during flyby E11 is shown in cyan in Figure B.3. The pointing variations with time are also shown in a video[2]. The black dot is the position of Cassini at the specified UTC below; the FOV is shown in cyan and corresponds to the instrument name input in the tool (in this case, VIMS). The result is an interactive 3D plot that can easily switch between different Cassini instrument measurement times with a slider to show the FOV of the instrument with respect to Enceladus. The instrument coordinate system is also translated to the ICRF frame, which reveals the expected image scene (in the instrument

[2]Link to tool video of flyby E11

x,y-plane). For example, if the plume is oriented in the positive x-direction of the instrument frame, it will also be in the same orientation in the image. Thus, even if the plume is not visible in the image, the expected location is still known from the tool.

B.1.4. Integration of Optical Phenomena

After implementing the required positions and orientations from SPICE, the optical phenomena can be placed in three-dimensional space. This process is challenging because these phenomena are not physical objects with a fixed location but rather illusions perceived by the observer.

Extended versus Localised Source

When looking at a rainbow on Earth, a large colourful arc spanning a wide FOV can be seen. The area of the rainbow matches the area of the curtain of raindrops, which scatters the light as seen on the left side of Figure B.4. Each wavelength that reaches the observer's eye originates from a droplet that is positioned at a slightly different angle. Additionally, when the observer moves, the rainbow will remain in the same apparent position with respect to the observer and the anti-solar point. This is because different droplets are observed that scatter the light in the exact same way as the previous droplets.

Unlike conditions on Earth, Cassini (the observer) is not surrounded by an extensive source of scattering particles, except when flying directly through the plume. In Cassini's observations, the plume particles are seen within very small instrument fields of view and from long distances, as detailed in section 2.4. This makes it impossible to observe full rainbow arcs, or halo and corona rings. However, a small portion of these phenomena can still be observed, as the plume acts as a localized source of light-scattering particles. This is comparable to a small "window" of particles capable of producing fragments of optical phenomena within an otherwise extended vacuum. It has been shown that the appearance of optical phenomena depends on the scattering angle from the Sun. Thus, the Sun-Enceladus-Cassini phase angle determines which parts of the optical phenomena are visible, or whether they are visible at all.

As shown in subsection B.1.3, the tool uses a fixed Enceladus and Sun position during the Cassini flybys. This also means that the scattering angles of the optical phenomena are fixed because these only dependent on the illumination geometry of the plumes. Thus, the observation of optical phenomena is solely determined by Cassini's position. For Cassini to see the optical phenomenon, its position must be compared to a reversed Earth condition as shown on the right side of Figure B.4. The localised plume is considered a point source of the optical phenomena. As sun rays hit this point, cones of light emerge with angles dependent on the wavelength. Now, the variable position of the observer dictates the observed wavelengths, like the colours of a rainbow.

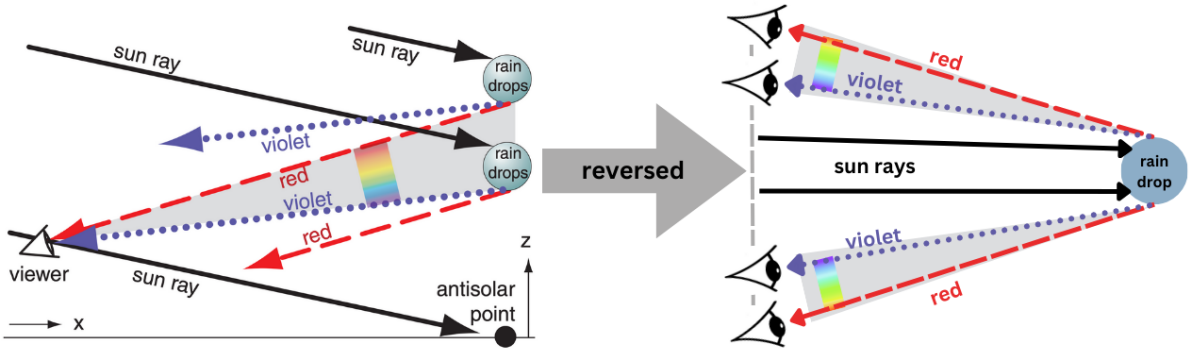

Figure B.4: Left: rainbow scattering as observed on Earth [75], right: rainbow scattering on Enceladus as observed by Cassini.

Scattering Angles

From section 2.1, simple relations for the scattering angles of the rainbow, halo and corona were given. These reveal where peaks of light at specific wavelengths are scattered which correspond to the angles of the cones shown in Figure B.4. For the tool, scattering angles for a discrete number of wavelengths can be implemented to show the angular boundaries of the optical phenomena between these

wavelengths. This approach is purely geometric and does include expected intensities. Combining Equation 2.1, Equation 2.2, Equation 2.6 for the primary rainbow yields the rainbow scattering angle $\theta_{rainbow}$ in Equation B.1.

$$\theta_{rainbow} = 2i - 4r = 2\arccos(\sqrt{\frac{n^2-1}{3}}) - 4\arcsin\left(\sin\left(\arccos(\sqrt{\frac{n^2-1}{3}})\right)/n\right) \tag{B.1}$$

The halo scattering angle can be obtained by rearranging Equation 2.7 with $A = \pi/3$ and where the angle of minimum deviation equals the halo scattering angle θ_{halo} in Equation B.2

$$\theta_{halo} = 2\arcsin\left(n\sin\left(\pi/6\right)\right) - \pi/3 \tag{B.2}$$

As can be seen from Equation B.1 and Equation B.2, the scattering angles of the rainbow and halo solely depend on the real relative refractive index between the refracting medium (ice or water) and the incident medium (assumed vacuum). For the rainbow, the refractive indices of liquid water at room temperature were taken from Segelstein [70] as input into the tool. The refractive index of the crystalline ice at 266K from Warren and Brandt [80] was used for the halo. Both models are shown in Figure B.5.

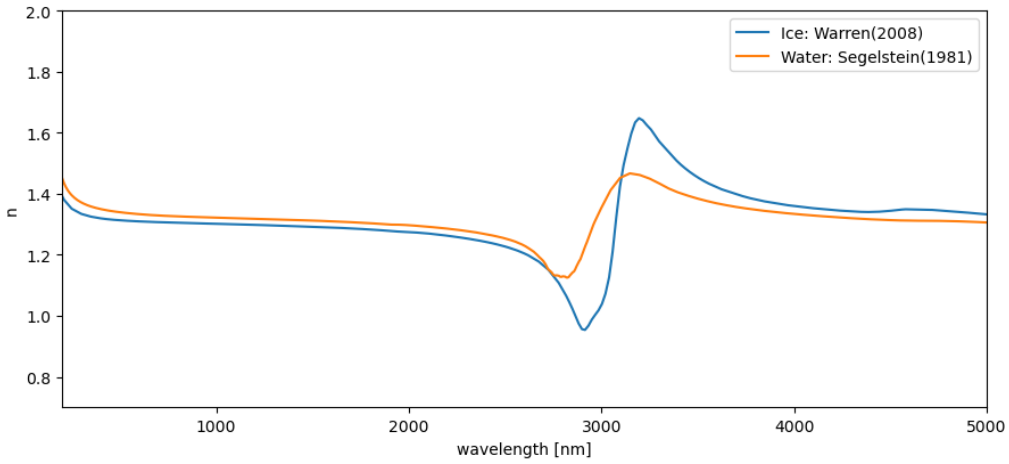

Figure B.5: Refractive indices of water and ice used in the SPICE tool.

The scattering angles of the corona in the tool are based on the peaks of the Fraunhofer diffraction intensity function shown in Equation 2.8. The peaks of the corona intensity function depend on the wavelength and the particle size. The tool accepts both variables as input and plots cones for the first three peaks or rings of the corona for each selected wavelength. An example of the corona intensity function in the tool is shown in Figure B.6. The scattering angle of the peaks becomes smaller with shorter wavelengths as well as the spacing between the peaks.

From a selection of wavelength inputs, the scattering angles of the phenomena can be computed and then translated into 3D surface cones. Next, the cones are aligned with the Sun-Enceladus vector and shifted so that the tip corresponds to the scattering origin in the plume. This origin was taken at an altitude of 40km from the south-pole of Enceladus. The result is shown in Figure B.7. Here, a rainbow (in front) and halo (in the back) are simulated for six discrete wavelengths in the visible spectrum during flyby E4. In order for Cassini to see the optical phenomena, its position must intersect a cone, and Cassini must look towards the plumes. In the case of flyby E4, neither is true, making it impossible to see the phenomena in the visible during this flyby. Another factor affecting the visibility of the optical phenomena arises from this simulation. The complete cones could be partially blocked by the body of Enceladus under high solar latitude illumination conditions. This would partially remove the phenomenon's visibility.

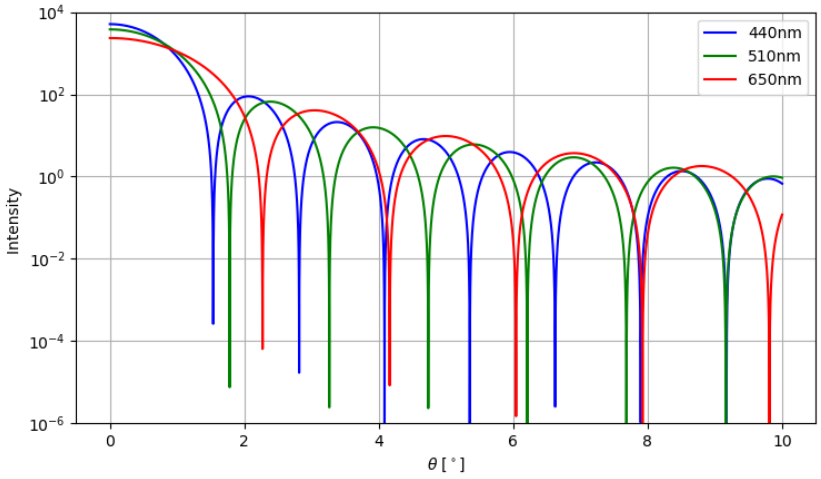

Figure B.6: Corona intensity as a function of scattering angle from a particle with a radius of 10 µm with Fraunhofer diffraction theory.

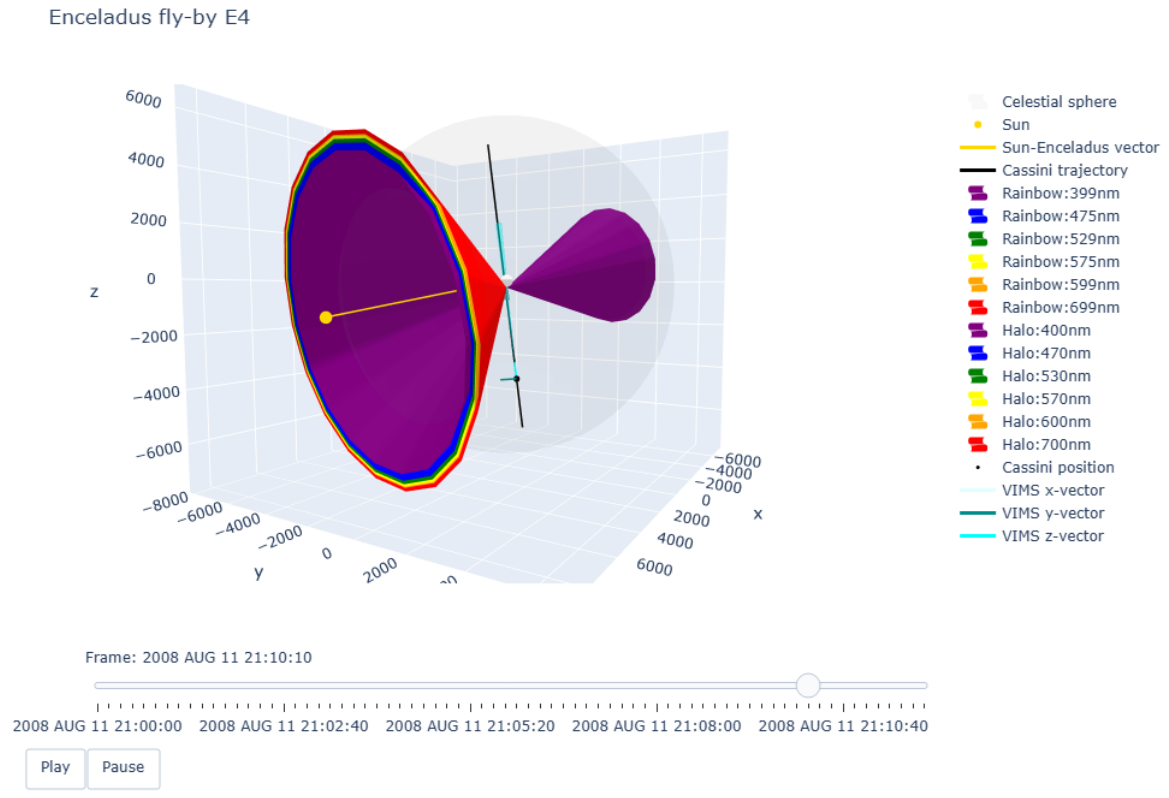

Figure B.7: Rainbow and halo cone projections for six discrete wavelengths in the visible spectrum during flyby E4. Distances are given in kilometers in Cartesian coordinates in the ICRF frame.

B.1.5. Verification

Several verification checks are implemented to ensure the accuracy and reliability of the aforementioned contributions to the tool. These checks include cross-referencing the refractive index models with published literature, validating the tool's outputs against observed data, and conducting sensitivity analyses to account for potential variations in plume material properties.

SPICE Integration

The solar phase angle is calculated one hour before and after Cassini's closest approach during each Enceladus-targeted flyby to verify the retrieval and integration of the SPICE ephemerides. Additionally, the distance between Cassini and the centre of Enceladus at closest approach is retrieved. These values are compared to those listed in Table 2.5. The consistent results confirm the accurate retrieval of the relative positions of Cassini and the Sun to Enceladus. The orientation of the instrument's field of view is verified by comparing it with the archived imaging sequences. For example, the orientation of the ISS and VIMS instruments is validated by identifying the time intervals during which the plumes are observed in the tool and matching those to the corresponding images available from the same flyby. The tool also confirmed that the Cosmic Dust Analyzer (CDA) aligned correctly with the plumes during in-situ sampling. Additionally, the expected orientations of Enceladus, based on the instrument coordinate system in the tool, were cross-checked with Enceladus' orientation in the archived images, further confirming the accuracy of the alignment.

Scattering Angles and Material Property Effects

The cone projections use the ice and water refractive indices from Figure B.5. However, there remain uncertainties in the exact composition of the plume particles [63, 65]. Therefore, it is important to investigate the sensitivity of the scattering angles to changes in material properties. These uncertainties can then be used to assign uncertainty boundaries to the scattering cones when searching for optical phenomena. Figure B.8 show the variations in halo scattering angles for a variety of crystalline ice refractive index models for a range of ice formation temperatures [27, 48, 68, 80]. An amorphous ice model from Kofman et al. [37] is included for comparison with the crystalline ice models. However, only crystalline ice is considered in this analysis as crystalline ice is necessary to create halos, while non-crystalline (amorphous) ice lacks the required hexagonal crystalline structure. Dhingra et al. [16] showed that Enceladus's plumes mainly consist of crystalline ice using VIMS measurements. Crystalline ice is only expected to form from condensing vapour at temperatures above 130 K [16]. Goguen et al. [25] estimated temperatures at the vent of 197K [25]. Looking at the right side of Figure B.8, it can be seen that halo angles can increase or decrease up to 1 degree from the chosen model from Warren and Brandt [80] in the visible and near-infrared. For wavelengths longer than 3 µm, as illustrated on the left side of Figure B.8, the selected model represents the lower limit, whereas other models can increase the halo scattering angle by up to 5°.

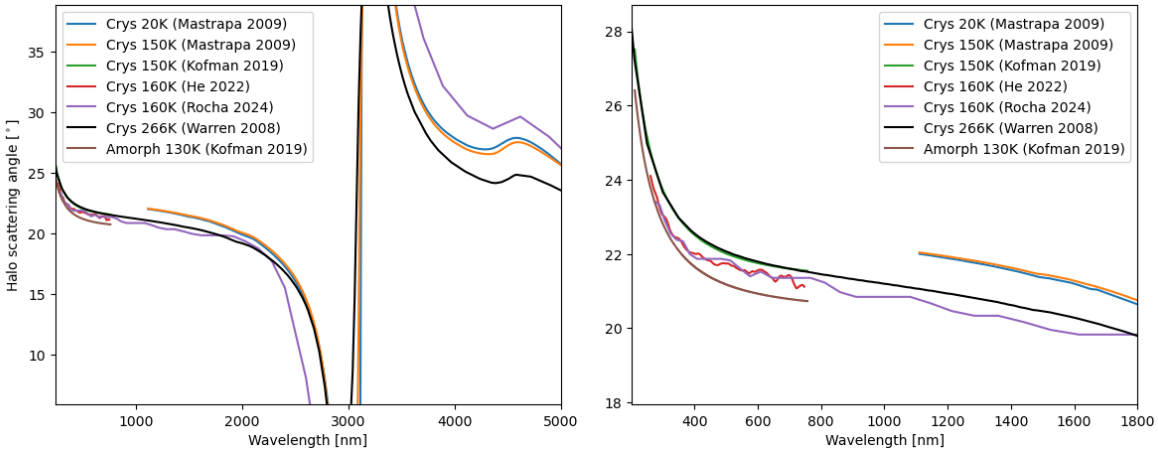

Figure B.8: Halo scattering angle versus wavelength for various ice refractive index models in the VIMS spectral range (left) and visible and near-infrared (right).

For rainbows, a distinction is made between the refractive indices of fresh water and seawater, as Enceladus' plumes are known to contain salt concentrations within the water ice [65]. Five models for the refractive indices of both fresh and seawater at different temperatures were compared [67, 70], as illustrated in Figure B.9. A conservative margin of 2° above and below the model used in the tool was determined to be sufficient. The angles of the corona scattering peaks were verified by recreating Figure 1 from Laven [40]. The accurate recreation is shown in Figure B.6. In addition, the implementation of the scattering angles into the tool cones was verified by simple trigonometric relations.

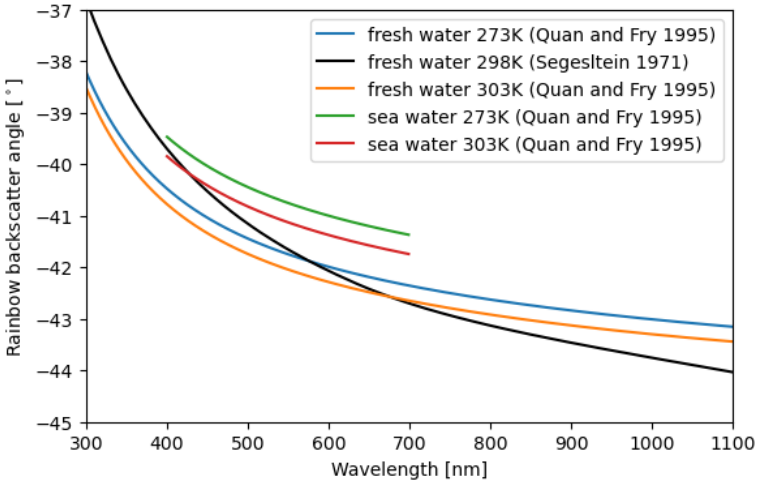

Figure B.9: Rainbow scattering angles for varying wavelengths and water refractive indices models.

B.2. Tool Iteration 1: 2D Corona Projection

The 3-dimensional tool locates when optical phenomena should be observable in the ISS and VIMS images. However, it does not directly show the appearance of optical phenomena in the image window. Therefore, an adaptation is made to the previous tool to project the expected phenomena onto the 2-dimensional instrument FOV. The focus was placed on the atmospheric corona rather than the halo, as the corona is more challenging to visualize, given its dependence on both wavelength and particle radius. While both the corona and halo are likely to occur in Enceladus' plumes (as discussed in subsection 2.5.1), the halo's scattering angles can be more directly retrieved based on observed wavelengths from Figure B.8. Importantly, since the orientation of both circular corona and halo features is the same relative to the Sun, determining the corona's orientation allows us to infer the halo's orientation as well.

Simulations are based on Mie theory, detailed in subsection 2.1.6. The inputs are the ice refractive indices from Warren and Brandt [80], a particle radius, and a set of discrete wavelengths to be considered. Gedzelman and Lock [22] found that 7 wavelengths in the visible are sufficient to accurately model the appearance of the corona. A corona simulation for monodisperse ice particles with a radius of 1.5 µm is shown in Figure B.10. These simulations use the miepython package from Prahl [66]. On the left side of the figure, the individual phase functions of a discrete set of seven wavelengths are shown. Their contributions are weighted with the Sun's blackbody spectrum and are combined to reveal the appearance of the corona shown on the right. These results were verified by running the same simulations in the MiePlot application made by Laven P. [41]. Individual wavelengths, or ISS broadband filters, can also be entered to simulate the observed corona for certain VIMS channels and ISS filters.

The Mie simulations are then integrated with the image orientations from SPICE. The tool allows the entry of an image ID of ISS NAC or WAC, which directly retrieves the image and mid-time from the PDS search atlas [57]. The results for ISS NAC image N1711553432 are shown in Figure B.11. Here, the ISS NAC image window is shown in the left-most figure with the solar direction and expected corona colour superimposed on the image through thinly spaced coloured lines. No immediate colour variations are visible in this case, but a homogenous purple background appears. The middle image shows a zoomed-out view, whereas the black square gives the actual image window. Now, colour variations can be seen from the plot's top right to the bottom left corners. The right-most image zooms out even further to reveal the first corona rings. This example illustrates how the tool can indicate the direction and appearance of the colour variations within the actual images. In addition to image IDs, the spice kernels can be loaded based on a manually entered time range. These will then show the field of view of the instrument and the expected corona with an added interactive slider, which shows the

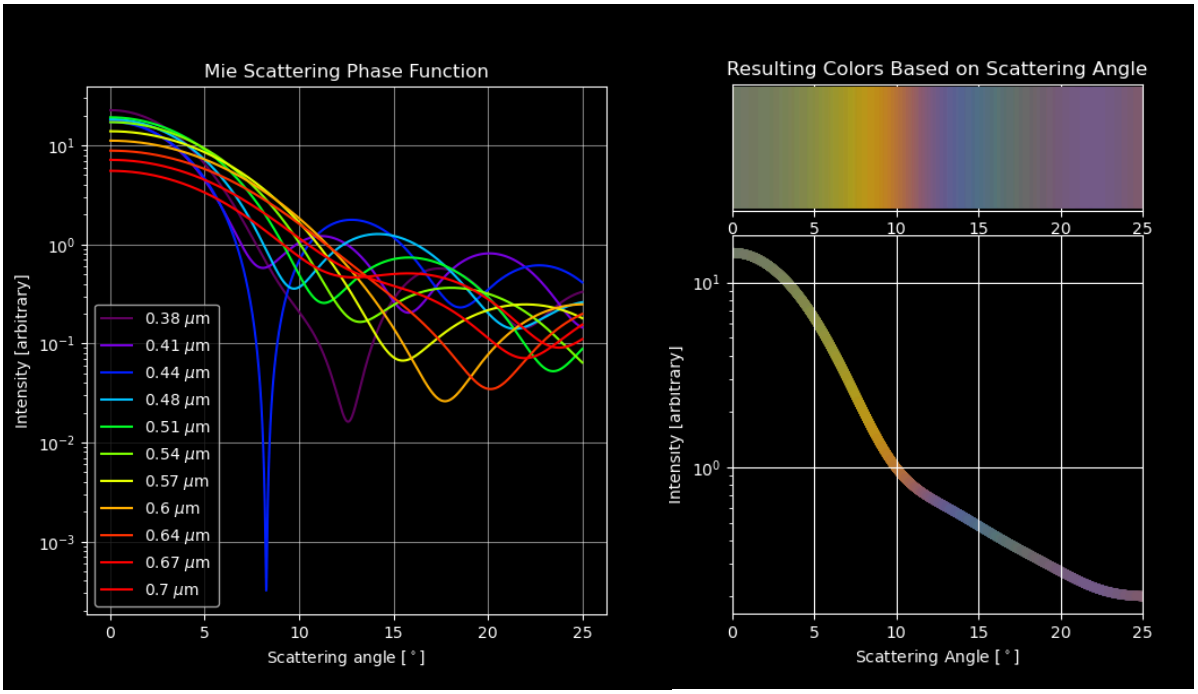

Figure B.10: Mie theory simulations of the atmospheric corona for ice particles with radius 1.5 µm in the visible spectrum.

progression of the corona projection for each time step. This can be used to analyse phase-dependent intensities throughout a flyby.

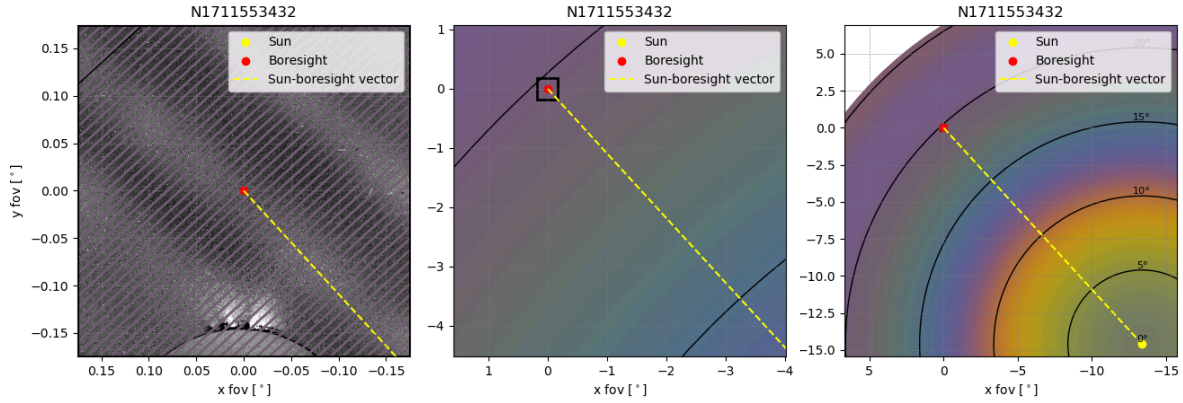

Figure B.11: Field of view of Cassini ISS NAC image N1711553432 with Corona simulation from Figure B.10

B.3. Tool Iteration 2: Saturn-Centered VIMS Projections

After identifying the stripe anomalies in chapter 4, it became clear that the stripes were decoupled from Enceladus and did not align with the expected optical phenomena described in section 2.1. This decoupling suggested that the source of the anomalies is located either in front of or behind Enceladus along Cassini's line of sight. As a result, the tool needs to be adapted to account for structures beyond Enceladus and its plumes. Furthermore, the cones associated with the known optical phenomena no longer contribute to the analysis. In subsection B.3.1, the required updates to the SPICE objects in the initial tool will be discussed, followed by the implementation of the VIMS cubes in subsection B.3.2.

B.3.1. SPICE adaptation

For the second iteration of the tool, the procedures described in subsection B.1.1 and subsection B.1.2 are repeated using the same data retrieval method and the ICRF inertial reference frame. However, the tool's scope must now be extended beyond the Enceladus-centered system. To achieve this, the central observer for retrieving relative ephemeris data is switched from Enceladus to Saturn. This change enables an analysis relative to other moons and rings within the Saturnian system. Structures like the positions and orbits of Saturn's inner mid-sized moons are easily added through data retrieval from the Saturnian satellite ephemeris kernels already included in the first tool iteration. Additionally, by loading a separate SPK-kernel, moons such as Saturn's many irregular satellites [15] are incorporated. Other parameters, including Cassini's position and instrument pointing (as discussed in subsection B.1.3), are recalculated to fit the new geometry relative to Saturn.

B.3.2. VIMS implementation

Calibrated cubes enhanced with SPICE information are available from vims.univ-nantes.fr [43]. Therefore, the orientation and position of each pixel in a cube can be mapped inside the tool. Having the FOV of Cassini during the Enceladus targeted flybys and images with positioning information allows for the opportunity to see the projection of the cubes at some distance along the line of sight of Cassini. This may give insight into the stripe anomalies' movement, geometry, and location. The RA and DEC coordinates of each pixel corner are retrieved from the VIMS data product using the PyVIMS (Version 1.0.4) - Zenodo Python package [71]. These spherical coordinates are then converted to rectangular Cartesian coordinates. This gives the orientation of the VIMS cubes in the ICRF frame dependent only on the projected distance from the centre of the observation, with the centre being Cassini's position during the mid-time of the cube observation.

The resulting tool is shown in Figure B.12. It accepts a list of cube inputs and will plot Cassini's position (blue) and FOV (cyan), including the projected cubes for each cube mid-time. Additional inputs include the spectral channel to be shown and the projected distance of the cube along the FOV. In this case, the VIMS projection distance is chosen to be the distance between Enceladus and Cassini. Other structures in the Saturnian system, like mid-sized moon orbits, are described in the legend on the right. As for iteration 1, the time slider allows for an interactive tool with easy comparison between cube observations. If no cube inputs are provided, the tool will work similarly to iteration 1, showing the geometries for specified time steps in a time range from the closest approach.

Another version of this tool was developed to compare two VIMS cubes and the alignment of the observed stripes. This version accepts two cube inputs and plots the observation geometries at the cube mid-times, along with the projected cubes at a specified distance, as illustrated in Figure B.13. Here, the blue dots show Cassini's positions, and Enceladus' are marked in white. In this setup, the expected FOV (displayed in cyan) appears larger than the actual field of view because only 32×14 pixels are used instead of the full 64×64 pixel window. Despite this, the alignment of the field of view from SPICE closely matches the projections retrieved from the VIMS data portal. These components are implemented independently in the tool, confirming the correct geometry implementation. Furthermore, it can be seen that Enceladus' position aligns with the VIMS observations, which capture the moon's body.

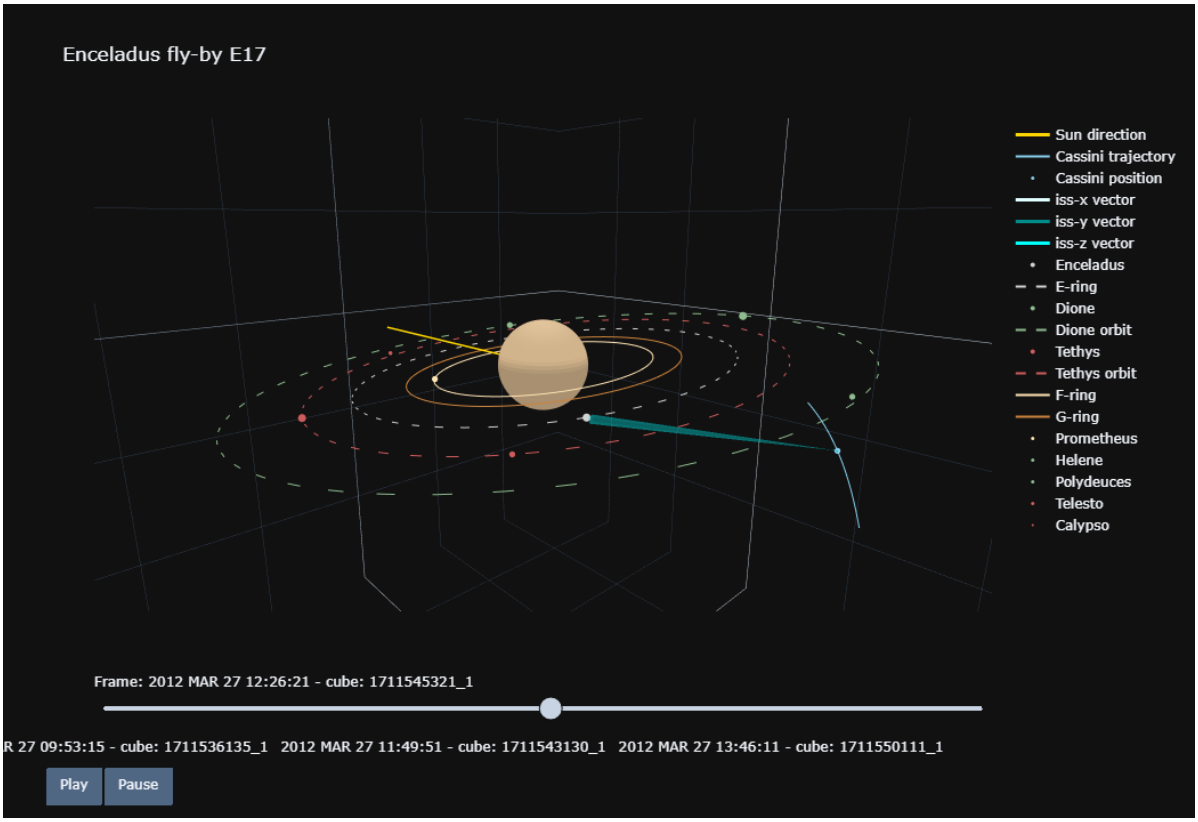

Figure B.12: Spice tool iteration 2 interface for Cassini flyby E17 VIMS observations.

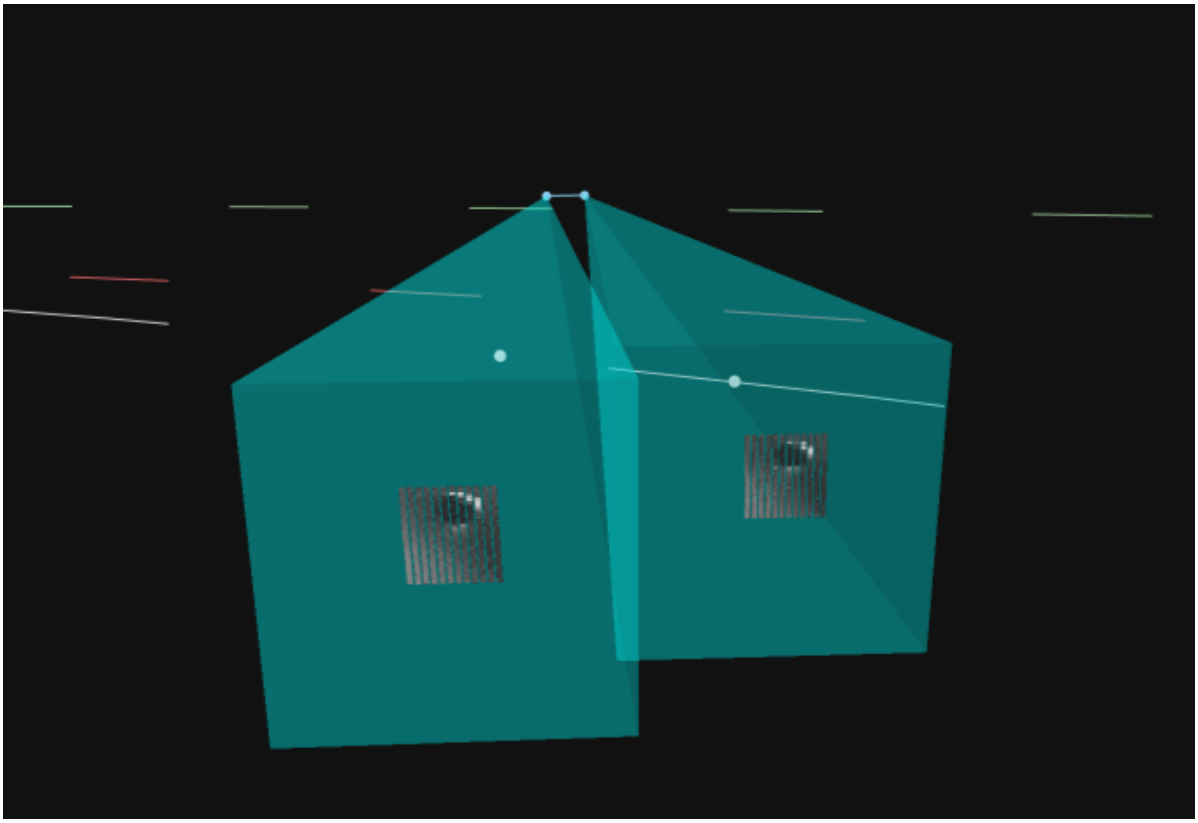

Figure B.13: Spice tool iteration 2, showing the observation geometries for VIMS cubes 1711546301 and 1711546939 along with their projected FOV close to Enceladus